6

Molecules and clusters in strong laser fields

Claus Peter Schulz[1], Tobias Burnus[2], Alberto Castro[3], E. K. U. Gross[3],
Andreas Heidenreich[4], Ingolf V. Hertel[1,5], Joshua Jortner[4], Tim Laarmann[1],
Isidore Last[4], Robert J. Levis[6], Miguel A. L. Marques[7],
Dmitri A. Romanov[6], and Alejandro Saenz[8]

[1] Max Born Institute, Berlin, Germany
[2] II.Physikalisches Institut, Universität zu Köln, Germany
[3] Institut für Theoretische Physik, Freie Universität Berlin, Germany
[4] School of Chemistry, Tel Aviv University, Israel
[5] Institut für Experimentalphysik, Freie Universität Berlin, Germany
[6] Temple University, Philadelphia, USA
[7] Departamento de Física, Universidade de Coimbra, Portugal
[8] Institut für Physik, Humboldt-Universität zu Berlin, Germany

Coordinated by: Claus Peter Schulz

6.1 Light matter interaction in the high field regime

In light matter interaction a ‘strong’ laser field will be defined differently depending on the process under investigation. In the context of this chapter a laser field is considered to be strong if the potential energy surfaces of the irradiated molecule or cluster are altered considerably. On an absolute scale one can compare the electromagnetic field of a laser pulse with inner-atomic fields. The electric field amplitude F of a laser pulse with the intensity I is given by

$$F = \sqrt{\frac{2I}{\varepsilon_0 c}} \tag{6.1}$$

with ε_0 being the vacuum dielectric constant, and c the velocity of light. For a ground state H-atom (with its electron in a distance of 1 Bohr radius a_0 from the nucleus) the field is strong if the intensity is $I \geq 3.5 \times 10^{16}\,\mathrm{Wcm}^{-2}$, while above some $10^{18}\,\mathrm{Wcm}^{-2}$ relativistic effects as well as the magnetic field component of the field become important. However, it turns out that molecules and clusters already completely disintegrate at intensities above $10^{16}\,\mathrm{Wcm}^{-2}$, ejecting fast highly charged ions. This interesting new research field of cluster dynamics initiated by ultraintense laser pulses will be presented in Sect. 6.6.

To study the chemical aspects one has to consider the typical energy level spacing of polyatomic molecules and clusters for the definition of the ‘strong field regime'. Laser intensities in excess of $10^{12}\,\mathrm{Wcm}^{-2}$ already induce substantial Stark shifting, polarization, and disturbance of the field free electronic states occurs to produce a quasi-continuum of new states in the molecule. Thus, intense short pulse lasers have led to the observation of many interesting strong field phenomena in atoms, molecules and clusters including: X-ray generation from high harmonics [1], above threshold ionization [2], above threshold dissociation [3], multiple electron emission from molecules [4], intact ionization of large polyatomic molecules [5–7], forced molecular rotation in an optical centrifuge [8], production of extremely high charge states from molecular clusters [9], production of highly energetic ions [10], and neutrons from clusters [11].

6.1.1 Experimental aspects

It is useful to mention some experimental aspects of strong field studies here, although the various laser systems and experimental methods of ultrafast physics will not be discussed. Suffice it to say that typically the basis of all table top short pulse laser systems used in these studies is the Ti:Sapphire laser at 800 nm which may be converted conveniently to the second harmonics and by using other nonlinear conversion schemes visible or near infrared laser wavelength can be employed. Present state of the art high intensity laser facilities can provide intensities up to $10^{20}\,\mathrm{Wcm}^{-2}$, using 800 nm Ti:Sapphire lasers with sub-50 fs pulse duration at a comfortable 10 Hz repetition rate (see e.g. [12]). Techniques to manipulate, stretch, shape and characterize the laser pulses have already been described in Chapter 2. However, a few subtleties concerning the definition of intensities, and calibrating them have to be discussed here.

Intensity calibration with short pulse lasers is a non trivial problem. What can be measured directly is the pulse energy E_P. But since one never has a constant spatial and temporal distribution of intensity it is important to define clearly to which quantity a given intensity refers. In the most favorable case the spatial and temporal distribution is Gaussian and the intensity I (mostly given in Wcm^{-2}) is

$$I(r,t) = I_m \exp(-\left(r/w\right)^2) \exp(-\left(t/\tau\right)^2) \tag{6.2}$$

with I_m giving the maximum intensity at $t = r = 0$ with τ and w characterizing the temporal and spatial beam profile – quantities which can in principle be measured experimentally by determining the autocorrelation function (for τ) and, e.g., the total energy passing a knife edge which is moved into the beam (for w). For a Gaussian one easily works out that

$$I_m = \frac{E_p}{\sqrt{\pi}\tau\pi w^2} \simeq \frac{E_p}{t_h\left(\pi w^2\right)} = 0.83\frac{E_p}{t_h d_h^2} \tag{6.3}$$

with t_h and d_h being FWHM of the temporal and spatial pulse width, respectively. We note that the maximum intensity at the pulse center corresponds to a hypothetical cylindrical beam of constant intensity of radius w. Note, however, that w is the $1/e$ beam waist radius, not the $1/e^2$ radius often given for laser beams! Since the beam parameters are difficult to determine quantitatively, the intensity in typical ion yield experiments is usually not measured absolutely. Rather one calibrates the intensity with a known intensity dependence for a standard ion (typically Xe^+) or compares photoelectron spectra with known data from the literature [13, 14].

6.1.2 Processes in strong laser fields: An overview

The response of an atomic or molecular system to a laser field can approximately be divided into two different regimes, the multi photon and the quasi-static regime. One relevant quantity to define the boundary is the average oscillation energy which a free electron acquires in the radiation field of the laser pulse. This *ponderomotive potential* is given by

$$U_p = \frac{e_0^2}{2m_e\varepsilon_0\, c}\,\frac{I}{\omega_L^2} \propto \lambda^2 I \tag{6.4}$$

with m_e the mass of the electron, ω_L the angular frequency of the laser radiation. Note that the ponderomotive potential depends quadratically on the laser wavelength λ, i.e., is most significant in the infrared wavelength region. To determine whether a field is strong one has thus to compare U_p with the atomic or molecular energy in question. When discussing ionization processes one would consider the *quasi-static regime* to begin at

$$U_p > E_I \tag{6.5}$$

where E_I is the ionization potential of the system. If one takes for example C_{60} with $E_I = 7.58\,\mathrm{eV}$ an 800 nm Ti:Sapphire pulse would in that sense be ‘strong’ when $I > 1.3 \times 10^{14}\,\mathrm{Wcm}^{-2} = I_{crit}$.

For low intensities and high frequencies ($I \ll I_{crit} \propto \omega_L^2 E_I$) the interaction can be well described by lowest-order perturbation theory (LOPT). The order N of the process is then given by the least number of photons required to reach the ionic ground state from the neutral initial state, i.e., N is the smallest integer fulfilling $N\hbar\omega_L > E_I$. This multi photon regime is illustrated for an atom in Fig. 6.1 (left panel). Note, that in LOPT approximation only a single photo electron peak with the kinetic energy $E_0 = N\hbar\omega_L - E_I$ exists.

Within the LOPT approximation the ionization rate Γ_{LOPT} is proportional to the Nth power of the laser intensity I, $\Gamma_{\mathrm{LOPT}} \propto \sigma^{(N)}\, I^N$ where $\sigma^{(N)}$ is the generalized N-photon cross-section that depends on the atomic or molecular system under consideration. The ab initio evaluation of $\sigma^{(N)}$ for systems only slightly more complicated than hydrogen-like atoms is, however, a very demanding task, since it implies a summation over all field-free eigenstates, including all continua. Converged 2-, 3-, and 4-photon cross-sections for atomic helium were presented in [15].

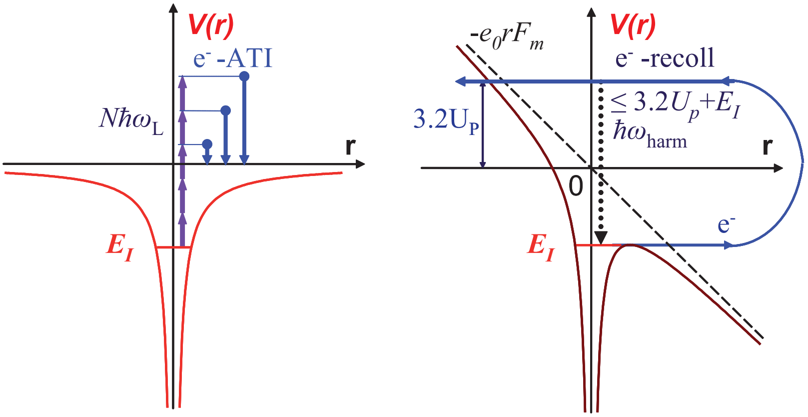

Fig. 6.1. Schematic illustration of an atom in a strong field with electron energetics and high harmonic generation. Left: multi photon ionization (upward arrows indicate photon energies), electron energies (full downward arrows) in above threshold ionization (ATI). Right: above barrier ionization in a strong field, indication the recollision electron with a maximum energy of $3.2\,U_p$, and high harmonics generation (dotted downward arrow).

The absence of spherical symmetry makes molecular calculations even more demanding. Within the fixed-nuclei approximation 2-, 3-, and 4-photon cross-sections for H_2^+ at the equilibrium distance $R = 2.0\,a_0$ were presented in [16]. These results were confirmed and extended to different R values and alignment of the molecular axis with respect to a linear polarized laser field in [17]. The molecular results for fixed R are qualitatively very similar to the ones obtained for atoms: a rather smooth variation of $\sigma^{(N)}$ as a function of the photon frequency underlying very sharp resonant peaks (that within LOPT actually diverge). These resonances indicate the presence of resonantly enhanced multiphoton ionization (REMPI) and are a consequence of intermediate states coming into resonance with M $(< N)$ photons. If this occurs, the intermediate state becomes populated. A proper treatment (within LOPT) requires the solution of the corresponding rate equations considering population and depopulation of the intermediate state by an M- and an $N-M$-photon process, respectively. The presence of REMPI peaks are also the reason that inclusion of vibrational motion in LOPT calculations of molecules is a nontrivial task [17]. While for processes like single-photon ionization it is possible to obtain approximate results by simply averaging over R weighted vibrational wave function of the initial state (usually the ground state), such a procedure works only in a very limited frequency regime for N photon processes. The reason is that for most photon frequencies the intermediate states are embedded in dissociative continua and the LOPT amplitudes are thus divergent. A proper treatment of this problem was then adopted in [18]. A further technical problem encountered for molecules is the dependence of $\sigma^{(N)}$ on the molecular alignment [19].

If the laser intensity is increased, the LOPT approximation becomes increasingly inaccurate. As a consequence, the ionization rate shows an intensity dependence differing from I^N. Usually, the increase with intensity is smaller than predicted by LOPT. Often this is called the nonperturbative multi photon regime. One characteristic of this regime is visible, if photoelectron spectra are recorded. By construction, the LOPT approximation assumes that only a single photoelectron peak exists, its energetic position being given by $E_0 = N\hbar\omega - E_I$. However, with increasing intensity additional peaks occur in the photoelectron spectrum at $E_n = (N+n)\,\hbar\omega - E_I$, $n = 1, 2, \ldots$ These so called above-threshold ionization (ATI) peaks are also indicated in Fig. 6.1 (left panel). In the language of perturbation theory they result from additional absorption of photons within the electronic continuum of states. With increasing laser intensity the relative importance of the higher-order ATI peaks increases and they can even provide the dominant path to ionization. As a consequence, LOPT fails to predict even the integrated ionization spectrum.

At intensities $I \gtrsim I_{crit}$ the atomic or molecular potentials are significantly deformed by the field as depicted in Fig. 6.1 (right panel). The electron e^- can escape from the atom in an *above barrier* process and is accelerated in the oscillating laser field. While a completely free electron would not be able to gain energy from the laser pulse (for energy and momentum conservation reasons) with the atom present this is possible. As first pointed out by [20], the electron can accumulate energy and – depending on its starting phase with respect to the laser field – may return to the atom with kinetic energies up to about $3.2\,U_p$. This is schematically illustrated by the trajectory in Fig. 6.1 (right panel) showing an electron starting at the barrier. This so-called *recollision process* is instrumental in high harmonic generation (HHG) and explains the experimentally observed plateau and cutoff of HHG toward high energies [20, 21].

Traditionally, one defines a dimensionless quantity, the so-called *Keldysh parameter*, introduced in [22],

$$\gamma = \sqrt{\frac{E_I}{2U_p}} = \sqrt{\frac{\varepsilon_0\, m_e\, c}{e_0^2}\,\frac{E_I\,\omega_L^2}{I}} \propto \frac{t_T}{t_L} \tag{6.6}$$

to differentiate between the high and low intensity regime. In the high-frequency low-intensity multi photon regime one has $\gamma \gg 1$, while $\gamma \ll 1$ indicates the validity range of the low-frequency high-intensity quasi-static regime. The Keldysh parameter γ may be understood as an adiabaticity parameter. If the laser frequency is small and thus the periodic change of the electric field $t_L = 2\pi/\omega_L$ is slow, the atomic or molecular systems responds to the field similar as to a slowly varying electric field. For sufficiently low laser frequencies the system can follow adiabatically and thus it is at every instant of time in an eigenstate of the total field dressed Hamiltonian. For sufficiently high intensity, ionization in an electric field occurs via tunneling through the field deformed Coulomb barrier with the tunneling time t_T or even by escape over the completely suppressed barrier (see Fig. 6.1). On the opposite side, in the high-frequency limit, the field changes too quickly for the system to follow and thus it remains in its field-free eigenstate. In this case, the system does not react on the oscillating field amplitude in terms of the quasi-static picture but on the presence of a perturbation given by the pulse envelope. Transitions are then (formally) induced by photon absorption, since the fast changing direction of the electric field vector does not allow the electron to escape through or over the field deformed barrier before the barrier closes.

This clear picture of the boundary between the multi photon and the quasi static regime at $\gamma = 1$ becomes blurred when the size of the molecular system is increased. Especially for molecules with extended π electrons (e.g., benzene, anthracene, unsaturated hydrocarbons, and fullerenes) [23–26] but also for metal clusters [27] it has been found that the ionization rate deviates from the power law (I^N) at much lower intensities than estimated from the Keldysh parameter. In contrast to atoms and small molecules, where the excitation and ionization processes are typically described by a single active electron, in larger molecular system multi electron effects cannot be neglected mainly for two reasons: The motion of the active electrons is no longer fast compared to the period of the laser field and doubly excited states exists below the ionization limit. More details and examples on this issue are presented in Sects. 6.3 and 6.4.

6.1.3 Control in strong fields

In recent years, studies in the strong field regime have been extended by using tailored laser pulses to interact with molecules and clusters. In contrast to the control in the linear or nonlinear perturbative regime discussed in Chapter 2 “strong- or intense-field control” relates to intensities and frequencies where the potential energy surfaces are disturbed by the laser field and a quasi-continuum of new states is produced. This allows the laser field to “reprogram” the molecular Hamiltonian in a time-dependent manner, creating a new quantum system while the laser pulse exists. For small molecules the intensities for strong field control lead to Keldysh parameters $\gamma < 1$ and the quasi-static picture is appropriate in those cases. However, not only the laser intensity itself determines the strength of the interaction with respect to the underlying physics, but also the ratio of the photon energy to the ionization potential of the atomic or molecular system considered. More details and an example for the control of wave packets in the ground state of H_2 is given in Sect. 6.2.

For larger molecular systems one might suspect the degree of chemical control using pulses with an intensity of 10^{12} to $10^{14}\,\mathrm{Wcm}^{-2}$ to be rather limited as a consequence of the highly nonlinear processes induced in the molecule. However, by using short pulse durations ($\approx 50\,\mathrm{fs}$), the exciting laser couples primarily into the electronic system modes of the molecule because it has they have similar characteristic response times. This limits the intuitively expected catastrophic decomposition to atomic fragments and ions. For example, in the strong field excitation of benzene [5], up to intensities of $10^{14}\,\mathrm{Wcm}^{-2}$ exclusively ionization of the parent species was observed, with little induced dissociation. The observation of a single dominant channel (intact parent ionization) suggested that most of the possible final state channels (i.e., the large manifold of dissociative ionization states) may be suppressed in the short pulse strong field regime. In this high intensity regime there is opportunity to substantially manipulate the molecular wave function with suitably shaped laser pulses to induce and manage photochemical reactivity and products. Section 6.3 will give more details and examples of successful experiments in “strong field chemistry”. The control of photo fragmentation in fullerenes is presented in Sect. 6.4.

One big challenge in this context is a detailed theoretical description of strong field induced processes in complex molecular system. A new theoretical method, which allows the *time-resolved* observation of the formation, the modulation, and the breaking of chemical bonds is presented in Sect. 6.5. This method provides a visualization of complex reactions involving the dynamics of excited states.

6.2 Strong-field control in small molecules

Alejandro Saenz

In view of the goal to control nuclear motion and since the laser field interacts primarily with the electrons, it is of interest to concentrate on the interplay between vibrational and electronic motion and thus it is important to understand the influence of vibrational motion on the strong-field behavior of molecules. It will be demonstrated below that strong fields allow for control of vibrational motion in a different way than low-intensity laser pulses. While control schemes based on multi photon processes can be understood as being based on resonant transitions between field-free states, the schemes in the quasi-static regime are often nonresonant and involve field-modified states. However, the strong-field control schemes will have to compete with ionization that is increasingly important as the laser intensity increases. In fact, most of the strong-field molecular experiments indicating field-induced formation of vibrational wave packets concentrated on the nuclear motion induced in molecular ions created by strong-field ionization. Similarly to the case of forming coherent vibrational wave packets in excited electronic states by a sufficiently short laser pulse that transfers the initial-state wave packet onto the excited state potential curve, a sufficiently short intense laser field can transfer the initial vibrational wave packet onto the ground-state potential curve of the molecular ion. A lot of experimental work has been devoted to the simplest possible molecule that is easily experimentally accessible: H_2. Due to its high ionization potential, it is a perfect candidate for studying molecules in the quasi-static regime.

Very early and long time before intense-field two-pulse pump-probe experiments became available, the behavior of H_2 (and other mostly diatomic molecules) in strong short laser pulses were analyzed assuming the following sequential process. During the very first phase of the laser pulse the molecules are aligned. In the case of a linear polarized laser pulse and a diatomic molecule like H_2 it should align with its molecular axis parallel to the electric field vector. It should be noted, however, that with the occurrence of short laser pulses (below 50 fs) the rotational period of the molecules is too long for alignment to occur. More accurately, the pulse creates a rotational wave packet, but due to the shortness of the pulse with respect to the rotational period, the induced rotational wave packet motion takes place on a time scale much larger than the pulse length. As a consequence, the subsequent field-induced processes like ionization occur while the molecules are still in their initial rotational wave packet. In a second step, but still during the rise of the laser-pulse intensity, H_2 is ionized due to tunneling ionization. Since the tunneling process is very fast (it should occur within half an optical cycle), the nuclei are practically frozen during the ionization process and thus the H_2^+ ion was predicted to be generated in a vibrational wave packet that is simply given by the projection of the vibrational ground state of the neutral onto the vibrational states of the ion, the Franck-Condon factors. While this wave packet starts to move, the laser intensity increases further and also the ion may be ionized. If the ionization stage has reached a certain level (in the case of H_2 evidently 2), the Coulomb repulsion of the nuclei in the resulting ion is not any longer compensated by the remaining electrons. Coulomb explosion occurs. From the analysis of the kinetic energy distribution of the fragments (protons in the case of H_2) three molecular strong-field effects were discovered: bond softening, bond hardening, and enhanced ionization. In fact, bond softening had already been predicted and experimentally observed long time before lasers were available that allowed the investigation of Coulomb explosion of H_2.

6.2.1 Potential-curve distortion: bond softening and hardening

Hiskes [28] investigated theoretically the behavior of H_2 and H_2^+ in a strong electric field. For H_2^+ the electronic ground and first excited states $1\,\sigma_g$ and $1\,\sigma_u$, respectively, are degenerate in the limit $R \to \infty$. Since an electric field parallel to the molecular axis breaks the *gerade/ungerade* symmetry, the degeneracy must be lifted (Wigner-von Neumann noncrossing rule for states of the same symmetry). In fact, the dipole moment between the two states (and thus the electric-field induced coupling) diverges for $R \to \infty$. The two potential curves repel each other and go asymptotically to $\pm\infty$. As a result of the distortion of the ground-state potential curve the high-lying vibrational bound states become unbound (dissociative) or can tunnel through the distorted potential curve (predissociation). This effect is called bond softening and is a general feature for diatomic molecular ions with an odd number of electrons (a condition that is fulfilled for most singly ionized molecular ions). In a static electric field this effect was experimentally observed almost immediately after its theoretical prediction [29]. Since the adiabatic field dressed curve of the upper electronic state bends upwards, it can support vibrational bound states, while it is purely repulsive in the field-free case. The appearance of field-induced bound states is called bond hardening or occurrence of light-induced states.[1]

The occurrence of bond softening also in laser fields in the quasi-static regime explained the experimental result that the fragments of Coulomb explosion of H_2 had a kinetic energy that corresponded to an ionization of H_2^+ (and thus to a transition onto the purely repulsive curve of $H^+ + H^+$) at relatively large values of R. These R values were on the other hand not reachable, if the wave packet created in the first ionization step would be propagating on the field-free potential curves. This indicates an important ingredient for strong-field control schemes: the in comparison to multi photon control additional ability of distorting potential curves allows to reach with a given wave packet R regions that would otherwise be very difficult to access.

Bond softening alone was, however, not sufficient to explain the experimental data, since according to the kinetic energy distribution there was not only a relatively large fraction of H_2^+ molecular ions produced at quite large R values, but the energy distribution of this (overall dominant) part of the spectrum was in addition very narrow. This indicated that the ionization of H_2^+ occurred in a very small R interval. Enhanced ionization, i.e., a pronounced increase of the ionization rate at a certain (typically quite large) value of R, turned out to be the reason for the observed narrow kinetic energy distribution. The first semiclassical models [30, 31] were later on also confirmed by full ab initio calculations [32, 33]. In the framework of the quasi-static approximation one should analyze the ionization rates on the adiabatic field dressed potential curves. As is discussed in [33] and in agreement with simple pictures explaining enhanced ionization, the lowest-lying adiabatic curve does not show enhanced ionization. However, the first excited (in the field upwards bending) state shows pronounced peaks in the ionization rate at specific large R values. The reason for this behavior are (field-induced) avoided crossings of this state with other higher lying but not (or not as strongly) upwards bending states. Since those higher lying states usually possess higher ionization rates due to their lower ionization potential and since this ionization rate is shared between two states showing an avoided crossing occurs, the upward bending state shows a pronounced peak in its ionization rate close to the avoided crossing. It is important to again emphasize that enhanced ionization occurs only

---

[1] Although the name bond hardening appears to be more popular as it implies the opposite effect to bond softening, it is not really appropriate, since the repulsive field-free state does not support any bond that can be "hardened".

in the excited adiabatic field dressed state. Since this state is supposed to be not noticeably populated in the first ionization step ($H_2 \rightarrow H_2^+$), the occurrence of enhanced ionization requires some nonadiabatic coupling between the two lowest states of H_2^+.

In view of the fact that the energy difference between the ground and first excited field dressed adiabatic states of H_2^+ is much smaller than the gap between H_2 and H_2^+ it is in the case of many experiments more appropriate to interpret the ionization of H_2 in the quasi-static picture, but the transition from the ground to the first-excited state of H_2^+ (though field distorted!) by means of (multi-)photon absorption. A recent work [34] has nicely demonstrated how the transition between the quasi-static and the multi photon picture, especially the multi photon transitions between field-distorted potential curves arises in the Floquet picture. With the aid of the very recently developed pump-probe experiments [35,36] with laser pulses of a pulse length of 12 fs and less it became now possible to monitor the wave packet motion of H_2^+ in real time. These experiments show clearly the effect of bond softening, i.e., the motion of the wave packet on field-distorted potential curves. The recent experiments [36] also indicate the occurrence of more than a single enhanced ionization peak in agreement with the older theoretical predictions.

In view of these strong-field effects specific to molecules (and absent for atoms) it is of course of interest whether they occur also for neutral molecules like H_2. Hiskes considered in fact this question with respect to bond softening and concluded that it should be absent for a molecule like H_2 (and all other typical covalent diatomic neutral molecules with an even number of electrons). The reason is quite straightforward. Although the electronic ground state of H_2 is also degenerate with an excited state for $R \rightarrow \infty$, the two degenerate states are not coupled by an electric field, since the excited state has triplet symmetry. This conclusion was seemingly not questioned for many years. In [37] it was, however, found from a numerical calculation for a 1D model of H_2 that enhanced ionization may occur for H_2.

A full ab initio treatment of molecules in laser fields is nontrivial, even if the quasi-static approximation is adopted. The reason is the requirement to evaluate the eigensolutions of the Hamiltonian describing the molecule and the laser field (usually only its dominant electric component) at a given instant of time. This is equivalent to the calculation of the eigenstates of a molecule in a strong static electric field. While standard quantum chemistry codes nowadays allow to calculate the molecular states in weak electric fields, the adopted procedures do not work for strong electric fields. The reason is that in such fields the states are unstable with respect to ionization. Thus one has to treat the metastability of the molecular states in a proper way. A correlated, fully three-dimensional calculation of the eigenstates of H_2 exposed to strong electric fields has been presented in [38]. Using a complex-scaled geminal approach both potential curves and ionization rates were given as a function of R. In a later, more detailed work also rovibrational states (within the Born-Oppenheimer approximation) were calculated and the problem of

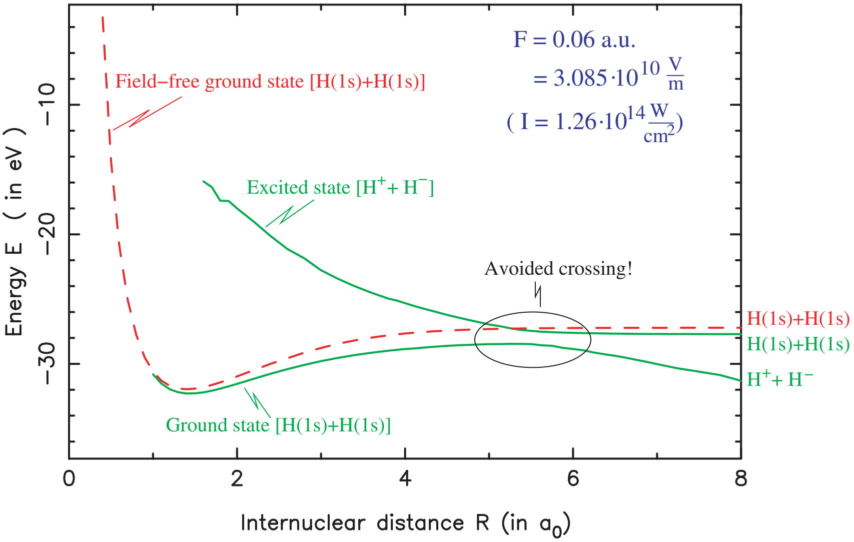

Fig. 6.2. The two energetically lowest lying adiabatic potential curves of H_2 (green) in a static field with strength $F = 0.06\,a_0$ (corresponding to a laser intensity of $I = 1.26 \times 10^{14}\,\mathrm{Wcm}^{-2}$) (cf. [38,39]). For comparison, the adiabatic field-free potential curve is also shown (dashed red). A dominant covalent or ionic character is indicated by the corresponding dissociation limits [H(1s)+H(1s)] and [H^++H^-], respectively.

standard quantum chemistry approaches to treat the metastable states was discussed [39, 40].

In Fig. 6.2 the lowest-lying adiabatic potential curves of H_2 in an electric field with a field strength $F = 0.06\,a_0$ are shown. Clearly, in contrast to the prediction of Hiskes, also neutral H_2 shows the effect of bond softening. In view of possible control applications this is very important, since it implies that a substantial deformation of potential curves is possible, even if there is no degeneracy of two field-free potential curves that is lifted by the field, as was the case for H_2^+. The origin of bond softening for H_2 is also evident from Fig. 6.2. While the covalent ground state of H_2 dissociating into H+H is in fact almost not influenced by the electric field (only a small Stark shift is visible), the state that dissociates into H^++H^- is strongly affected by the field, as it represents a (diverging) dipole for $R \to \infty$. It has to be reminded that this ionic state does not exist in the adiabatic picture. In this picture the ionic character is contained for small R mainly in the $B\,^1\Sigma_u$ state, but for increasing R it is partially transferred to other adiabatic states. The double-well character of some of the excited electronic states is a consequence of the avoided crossings that occur due to the passing of the diabatic ionic state through the sequence of adiabatic states. Since the in the field-free case quite energetic ionic state represents an electric dipole, its energy decreases (to a good approximation) linearly for $R \to \infty$. As a consequence, in a diabatic picture the ionic state will for a sufficiently large value of R cross the covalent ground state. If the covalent ground state and the ionic state possess (at least in the field that breaks parity) the same symmetry, an avoided crossing occurs. This avoided crossing is the one shown in Fig. 6.2. It is responsible for bond softening. As a further consequence, the adiabatic ground-state curve changes its character from covalent (dissociating into H+H) to ionic ($H^+ + H^-$).

6.2.2 *R* dependence of the ionization yield

In Fig. 6.3 the ionization rate of H_2 in an electric field ($F = 0.08\,a_0$) is shown as a function of R. The avoided crossing with the ionic state leads to a pronounced peak in the ionization rate. This confirms the occurrence of enhanced ionization also for neutral H_2 for which an earlier indication was already given by a 1D model calculation [37]. On the basis of the accompanying analysis of the potential curves the origin of enhanced ionization for H_2 is of course evident: at the avoided crossing the adiabatic eigenstate is a mixture of the covalent and the ionic state. Since the latter has a much smaller ionization potential and thus larger ionization rate, the covalent state acquires ionization

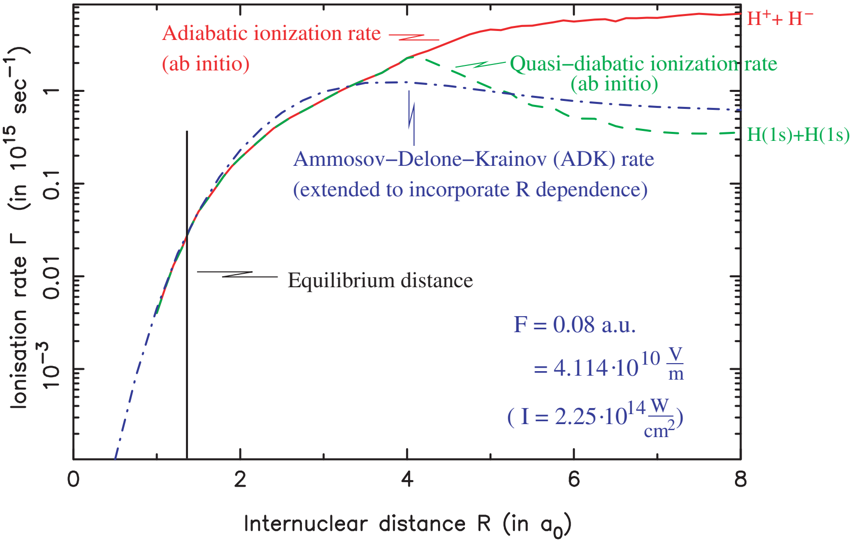

Fig. 6.3. The ionization rate of H_2 in a static field with strength $F = 0.08\,a_0$ (corresponding to a laser intensity of $I = 2.25 \times 10^{14}\,\mathrm{Wcm}^{-2}$) is shown as a function of the internuclear separation R (cf. [38,40]). The ab initio results within the adiabatic (red) and a quasi-diabatic (green) approximation are compared to a simple atomic tunneling model (ADK approximation) that is extended to the molecular case by using an R-dependent ionization potential (blue).

rate from the ionic state [38,39]. If a wave packet moves very slowly over the avoided crossing, it would follow the adiabatic potential curve and thus change character from the covalent to the ionic state. In such a case a step-like feature in the ionization rate occurs at the crossing. If the wave packet moves very fast over the avoided crossing, it will follow the diabatic curves and thus regain its covalent character (and ionization rate) after the crossing. In this case a peak appears in the ionization rate. A time-dependent calculation (for short laser pulses with 800 nm wavelength) has shortly thereafter confirmed the possible occurrence of enhanced ionization in H_2 and its origin due to a change from the covalent to the ionic character [41].

A lesson that can be learned from the examples of H_2^+ and H_2 for strong-field control is the occurrence of potential-curve deformation, if either the field-free degeneracy of states is lifted by the field or if field-induced avoided crossings occur. Clearly, molecular states dissociating into cation-anion pairs will be most strongly affected by the external field. As these states are usually not existent as well-defined states in the adiabatic formulation, but are admixtures of different states, it is clear that already weaker fields than the ones discussed here for the H_2 ground state should have a strong effect on the excited states potential curves. Furthermore, the average energy difference between excited states is usually much smaller than the gap between the electronic ground and the first excited state. As is discussed in [42] a large number of field-induced avoided crossings occur in the electronically excited state spectrum of H_2.

Returning to Fig. 6.3 it may be observed that even in the R range where no avoided crossing occurs, the ionization rate is strongly R dependent (note the logarithmic scale). Already about thirty years ago it was pointed out by Hanson that in the case of H_2 the ionization in a strong electric field should dominantly occur at a larger internuclear distance than the equilibrium one [43]. A more general discussion of the influence of vibrational motion on the laser-field ionization in the quasi-static regime was then given in [44]. In the quasi-static picture (appropriate for sufficiently long pulses for which the ionization during the turn-on and -off process is a negligibly small fraction) and assuming validity of the Born-Oppenheimer approximation the ionization process may be described as a transition from the rovibrational initial state of the neutral to one of the rovibrational states of the ion. This transition is mediated by some electronic transition moment. In the quasi-static approximation this transition moment is the R-dependent ionization amplitude describing the ionization probability (at fixed R) in an electric dc field. As was discussed above, for molecules such ionization amplitudes are difficult to obtain from ab initio treatments. For H_2 ionization rates of the type shown in Fig. 6.3 can be used. In order to obtain approximate R-dependent ionization rates for larger molecules, simpler approaches are required. The probably simplest model one can think of is the very popular Ammosov-Delone-Krainov (ADK) [45] model.

In order to adopt this atomic model to molecules it was proposed to use in the ADK formula an R-dependent ionization potential $E_I(R)$ instead of the physical one [44]. While $E_I(R)$ is the energy difference between the ground-state potential curves of the ion and the neutral, the physical ionization potential is of course the R-independent difference between the rovibrational ground states of ion and neutral. The concept of a substitution of the physical by an R-dependent ionization potential can also be used in other originally atomic laser-field ionization models like the strong-field approximation (SFA), as was mentioned already in [44]. The later on performed full ab initio calculation of the static ionization rate for H_2 [38, 46] confirmed, however, the validity of the ADK model to predict the R dependence of the ionization rate [40] at the static limit. This is also apparent from Fig. 6.3 where both ab initio and ADK (with R-dependent ionization potential) rates are compared. In fact, even the quantitative agreement is very good, as long as the parameters belong to the validity regime of the ADK model. Since the ADK approximation is based on a tunneling model, this approximation is only applicable, if the field distortion of the Coulomb barrier is not so strong that the electron can escape over the distorted barrier, but has to tunnel through it. From classical arguments the field strength where over-the-barrier ionization sets in is given by $F_{\mathrm{BSI}} = E_I^2/4$. Using the ADK tunneling formula outside its validity regime, i.e., for $F > F_{\mathrm{BSI}}$ yields a clear overestimation of the ionization rate. Using the R dependent ionization potential, one obtains $F_{\mathrm{BSI}}(R) = E_I^2(R)/4$ and thus deviations from the ADK behavior occur not only as a function of F but also of R [40]. Of course, ADK is also only valid in the quasi-static limit and not in the multi photon regime. This sets an intensity and wavelength limit from below for the applicability of the ADK model.

Based on the ADK approximation the influence of vibrational motion on strong-field ionization can be visualized with the aid of the example of three prototype diatomic molecules [44]. Assuming for simplicity the same shape of the potential curves of the electronic ground states of the neutral and the ion, one may still distinguish three generic cases. The equilibrium distance of the neutral and the ion ($R_{\mathrm{eq}}^{\mathrm{ion}}$ and $R_{\mathrm{eq}}^{\mathrm{neut}}$, respectively) are either almost identical, or one of the curves is shifted horizontally with respect to the other. Example molecules would be N_2 where the removal of a nonbonding electron results in $R_{\mathrm{eq}}^{\mathrm{ion}} \approx R_{\mathrm{eq}}^{\mathrm{neut}}$, H_2 where removal of a bonding electron gives $R_{\mathrm{eq}}^{\mathrm{ion}} > R_{\mathrm{eq}}^{\mathrm{neut}}$, and O_2 where an antibonding electron is removed and thus $R_{\mathrm{eq}}^{\mathrm{ion}} < R_{\mathrm{eq}}^{\mathrm{neut}}$. As a consequence of the exponential dependence of the tunneling ionization rate on the ionization potential even small shifts of R_{eq} have relatively drastic effects, see Fig. 6.4. Compared to an atom (with R-independent transition rate) the case $R_{\mathrm{eq}}^{\mathrm{ion}} \neq R_{\mathrm{eq}}^{\mathrm{neut}}$ yields a smaller ionization probability (suppressed ionization), but there is a substantial cancelation effect and thus the overall ionization rate (to all possible rovibrational final states) is only slightly suppressed for the given examples (when using realistic molecular data for the mentioned diatomic example systems H_2, N_2, and O_2). More pronounced effects can be expected for nonsequential multiple ionization processes. It has to be emphasized that these three examples serve just as an illustration of

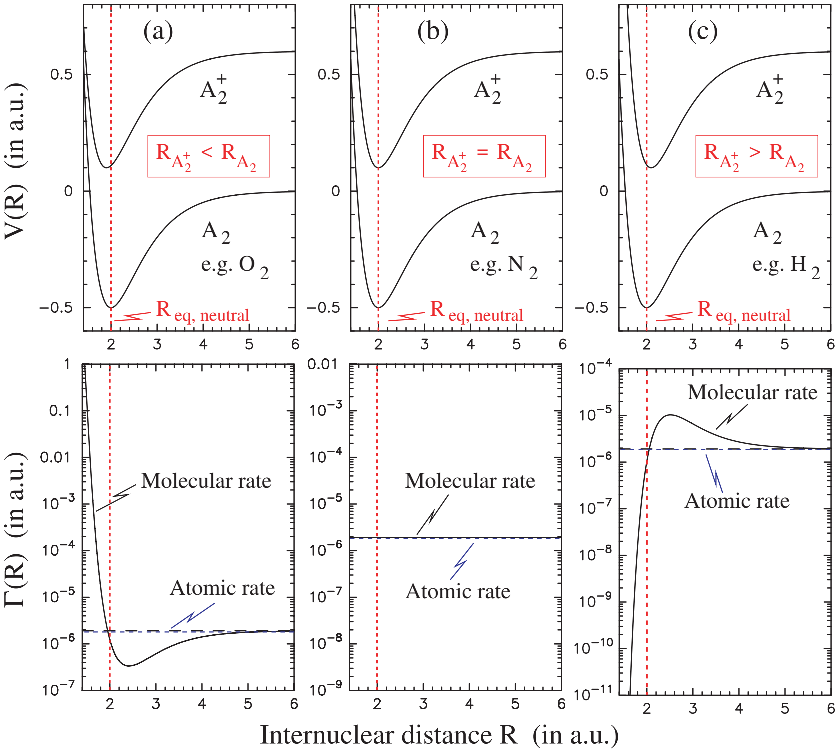

Fig. 6.4. The potential curves (upper row) and ionization widths (lower row) of three prototype diatomic molecules A_2 are shown [44]. The three cases differ in the equilibrium distance of the cation relative to the one of the neutral. If these distances agree (2 nd column) the ionization rate predicted by an R-dependent ADK model agrees with the one of an atom with the same ionization potential. Otherwise, a strong R dependence of the ionization rate is predicted.

how the ionization process can be influenced by structural properties closely related to the vibrational dynamics. As is discussed below, this can serve as a tool for control of vibrational motion. The model proposed in [44] is on the other hand very simple and thus can easily be applied to many molecular systems (using realistic potential curves for neutral and ion), including (especially nonsequential) multiple ionization.

Before discussing consequences of the within the quasi-static approximation predicted pronounced R dependence for molecules like H_2 and O_2, it is of course an important question whether the quasi-static approximation itself is at all applicable for realistic laser pulses. In fact, it was pointed out in [48] that already for the simplest atomic system, the hydrogen atom, the quasi-static approximation is only applicable for extremely high intensities in which for femtosecond lasers saturation occurs. In a very recent work the

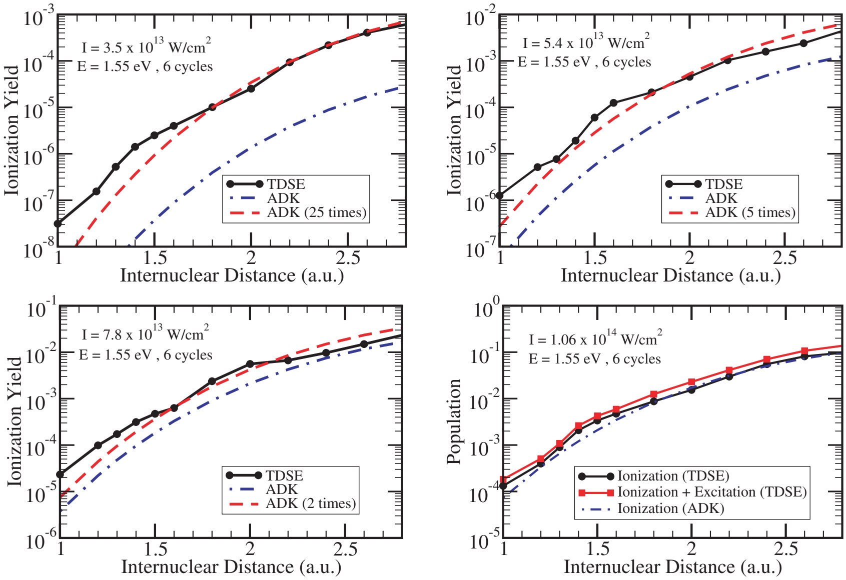

Fig. 6.5. Comparison of the R dependent ionization yield of H_2 in 800 nm laser pulses of 6 cycle duration ($\cos^2$ envelope) and four different peak intensities as specified in the plots [47]. The results of the full TDSE solution (black) is compared to the prediction of the (R-dependent) unscaled (blue) and scaled(red) ADK model that is equivalent to the quasi-static approximation. For 1.06×10^{14} Wcm^{-2} only the unscaled ADK result is shown together with the TDSE result (red) showing population of all but the initial H_2 ground state.

R dependence of the ionization rate of H_2 in a 800 nm laser pulse of 15 fs duration was investigated using a full solution of the TDSE (describing the two electrons in full dimensionality and including correlation, the technical details being described in [49]). It was found that the quasi-static approximation fails in most cases to predict the ionization yield *quantitatively*, but especially the R dependence is very well *qualitatively* described for intensities above 10^{13} Wcm^{-2} [47]. This is seen in Fig. 6.5 that shows the R dependence of the ionization yield in 800 nm laser pulses of about 16 fs duration for different intensities around 10^{13} to 10^{14} Wcm^{-2}. The results are compared to the ones obtained with the ADK model (that for the considered intensities agrees well with the complete quasi-static approximation, cf. Fig. 6.3). If the ADK results are multiplied by an overall multiplicative factor, the agreement to the full TDSE calculations is very good. In fact, for a peak intensity of 1.06×10^{14} Wcm^{-2} even the quantitative agreement is very good, but this is to some extent accidental. For this intensity not only the ion yield (= population of ionic states) but also the population of all but the initial ground state is shown. In agreement with simple strong-field models the excitation of neutral excited states is small at these intensities, and shows almost the same R dependence as the ionization yield.

6.2.3 Deviations from the Franck-Condon approximation

An immediate consequence of a pronounced R dependence of the strong-field ionization rate is the fact that the wave packet created by means of a corresponding laser in the molecular ion will not be correctly described by Franck-Condon factors. The reason is simple. In the derivation of the Franck-Condon factors it is assumed that the electronic transition moment is sufficiently R independent (within the R range covered by the initial vibrational wave packet) to be taken out of the integral over R. This point was already remarked in [44]. Based on the model proposed in that work, the vibrational wave packet created in intense laser fields was predicted and compared to experiment in [50]. The results are shown in Fig. 6.6. The (simple) theoretical model predicts a strong deviation from the Franck-Condon distribution, since the latter is rather broad and has its maximum for $v = 2$. The distributions predicted for strong laser fields (in between 10^{13} and $10^{14}\,\mathrm{Wcm}^{-2}$) are on the other hand much narrower and have their maxima at $v = 0$ (or 1). Within the model it is also predicted that the deviation from the Franck-Condon distribution is more pronounced for lower intensities. In fact, Fig. 6.6 shows for the theoretical data two distributions for every intensity. One simulates a parallel orientation of the field and the molecular axis, the other one a perpendicular orientation. Within the simple model the difference is given by the fact that only for parallel orientation there is a noticeable potential-curve distortion at the considered field intensities. As a consequence of the distortion, the higher lying vibrational states of H_2^+ become unbound and thus yield dissociation. In Fig. 6.6 only the nondissociated H_2^+ ions are shown, since the experiment was only able to measure those.

In Fig. 6.6 also experimental results are given for three peak intensities (covering the range of the theoretical data) for a laser pulse of about 45 fs pulse length. The experimental results are in very good qualitative agreement with the theoretical predictions. One clearly sees a very similar deviation from the Franck-Condon distribution, and the same trend as a function of intensity (stronger deviation for lower intensities) is also visible. Finally, Fig. 6.6 shows also the result obtained with a ns laser pulse. According to the discussion given above, one expects that in the ns pulse the molecules will be quite well aligned, while in the 45 fs laser pulse they will be more or less randomly oriented. The sharper cut-off (due to dissociation) predicted by the theory for a parallel aligned sample is also seen in the experiment. In conclusion, the experiment confirms the predicted pronounced R dependence of the strong-field ionization rate of molecules like H_2. This is in contrast to the multi photon regime (LOPT or weakly perturbative) that shows only very little R dependence, if no resonances are involved. As a consequence of the R dependence in the

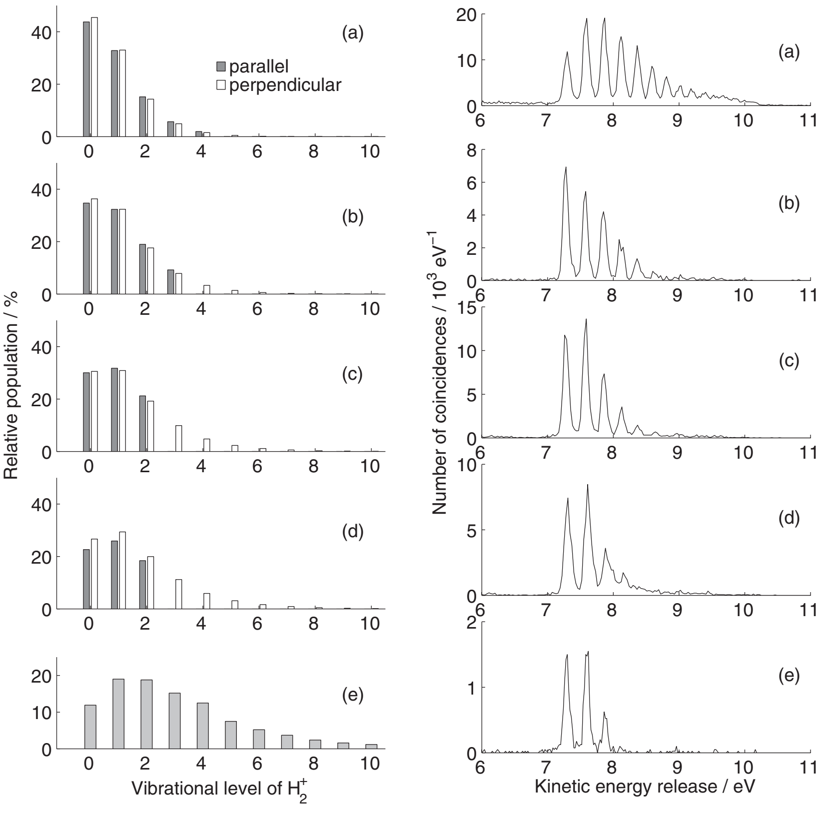

Fig. 6.6. Distribution over bound vibrational states of H_2^+ formed in strong laser-field ionization of H_2. Left panel: theoretical prediction on the basis of the quasi-static approximation for laser peak intensities (a) 3.5×10^{13}, (b) 5.4×10^{13}, (c) 7.8×10^{13}, and (d) 1.1×10^{14} Wcm^{-2}. The dark-gray bars correspond to a parallel, the white bars to a perpendicular orientation of the molecular axis with respect to the linear-polarized laser field. Right panel: Experimental results for laser peak intensities (a) 3×10^{13}, (b) 4.8×10^{13}, and (c) 1.5×10^{14} Wcm^{-2} and pulses of about 50 fs FWHM pulse duration. In (d) the distribution measured with a laser peak intensity of 1×10^{14} Wcm^{-2} but a pulse length in the ns range is shown.

strong-field regime it is possible to control the shape of the formed vibrational wave packet by varying the intensity of the laser.

6.2.4 Formation of vibrational wave packets in the nonionized neutral initial state

The pronounced R dependence of the strong-field ionization rate of molecules like H_2 may also be used in a different way to influence and control vibrational motion. In [51] it is proposed that with the aid of a sufficiently short pulse it

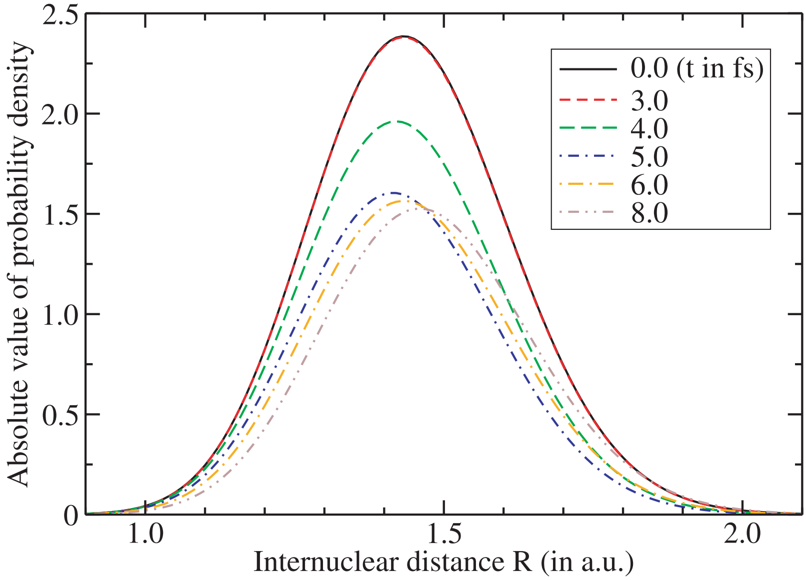

Fig. 6.7. The vibrational wave packet in the electronic ground state of H_2 is shown at different times for a laser pulse with 800 nm, 8 fs duration ($\cos^2$-envelope), and peak intensity 6×10^{14} Wcm^{-2} [51].

is possible to create a vibrational wave packet in the nonionized neutral H_2 molecules. For the theoretical modeling of this process the model proposed in [44] was extended in such a way that the vibrational motion was treated explicitly. For this purpose, the time-dependent Schrödinger equation describing vibrational motion of H_2 was solved. The ionization process was described with the aid of an imaginary (optical) potential. For the considered intensities the influence of potential-curve distortion was assumed to be negligible and thus omitted for clarity. The resulting wave packet motion, i.e., snapshots at specific time intervals, is shown in Fig. 6.7. Besides the overall decrease of the amplitude of the wave packet due to ionization one notices that in fact, as expected from the R dependence of the ionization rate, the wave packet is preferentially ionized and thus decreases more pronounced at larger values of R. If this R-dependent depletion process occurs fast enough to not be washed out by vibrational motion (for H_2 the ionization should occur within at least 5 to 10 fs), the laser pulse leaves behind a vibrational wave packet in the neutral H_2 molecules. It should be emphasized that this is a purely quantum-mechanical effect that cannot be explained with any ensemble statistics, since in a (semi-)classical world the molecules that happen to have a larger R value when being hit by the laser pulse would only be ionized with a higher probability. However, the molecule would be either ionized or not. In both cases no wave packet in the nonionized molecules can be created.

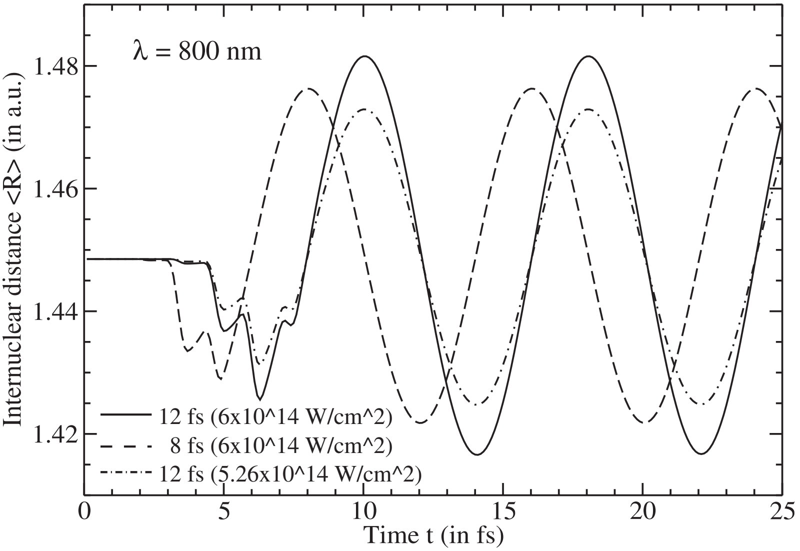

Fig. 6.8. The variation of the mean value of the internuclear separation $\langle R\rangle$ as a function of time in laser pulses with $\cos^2$ envelope, 800 nm, peak intensity $I = 6 \times 10^{14}\,\mathrm{Wcm}^{-2}$, and a duration of 12 fs (solid) or 8 fs (dashed) [51]. Also shown (chain) is the result for a 12 fs pulse with the same ionization rate as the 8 fs pulse which is achieved by lowering the intensity to $I = 5.26 \times 10^{14}\,\mathrm{Wcm}^{-2}$.

The creation of the wave packet is better monitored by plotting the time-dependent mean value of R as is shown in Fig. 6.8. In the beginning of the pulse (once the intensity is sufficient to ionize) R decreases due to the R-dependent depletion. However, while the linearly polarized laser changes field direction, its field component passes through zero. During this period of low intensity no further ionization occurs and the already created wave packet starts to swing back (R increases). In the following half cycle further ionization occurs, and R decreases even more. This continues until the pulse envelope decreases so much that no further ionization occurs. Now the created wave packet swings back and forth. Since the wave packet is formed from vibrational states of the same electronic state of the homonuclear H_2 molecule, the decoherence time is expected to be extremely long. The reason is that the wave packet can only relax via spontaneous two-photon emission, because one-photon transitions are dipole forbidden. The wave packet shows also a surprisingly clean oscillation without evident collapses and revivals etc. This is a consequence of the fact that in the considered intensity regime the wave packet consists almost exclusively of $v = 0$ and $v = 1$ components. The contributions of higher v components are to a good approximation negligible. Therefore the oscillation period is very accurately given by the one determined by the energy difference between $v = 0$ and $v = 1$ of H_2 which is about 8 fs.

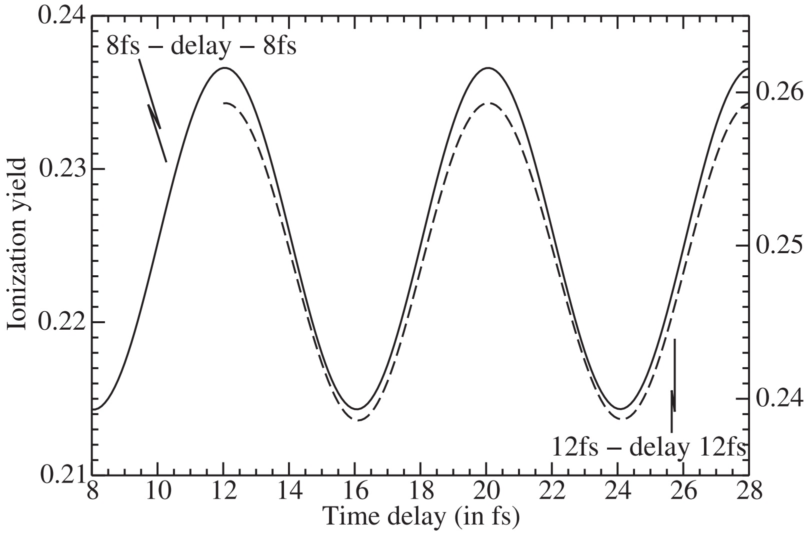

Fig. 6.9. Theoretically predicted total ionization yield measured in a pump-probe experiment on H_2 using either two identical laser pulses with 8 fs (solid) or 12 fs (dashed) duration. The pulses possess peak intensity $6 \times 10^{14}\,\mathrm{Wcm}^{-2}$, a $\cos^2$ envelope, and 800 nm wavelength [51].

Most surprisingly, the wave packet formation process happens to be very robust with respect to the field parameters. The amplitude of the created wave packet depends on the exact form of the pulse, but its shape is almost independent of the exact pulse parameters. For example, changing the wavelength (as long as the quasi-static description is valid) from 800 to 1064 nm or the absolute carrier-envelope phase by $\pi/2$ does practically not influence the final form of the wave packet. Therefore, no stabilization of the carrier-envelope phase is, e.g., required for the wave packet formation and also the finite bandwidth (quite substantial for ultrashort laser pulses) does not pose any problem. The remaining question is, of course, whether the predicted wave packet can be experimentally verified. As is clear from Fig. 6.8, the oscillation takes place in a very small interval of R values. However, the pronounced R dependence of the ionization rate that was the origin of the wave packet may also be used for its detection. As is discussed in [51], performing a pump-probe experiment with a second very short pulse (possibly a replica of the first one, since this is most easily experimentally accessible) uses also in the probe step the strongly nonlinear R dependence. In Fig. 6.9 the result of such a simulated pump-probe experiments is shown.

Already very shortly after its prediction, the wave packet formation was experimentally confirmed by a pump-probe experiment as the one proposed in [51]. Performing the experiment on D_2 and using laser pulses of a FWHM

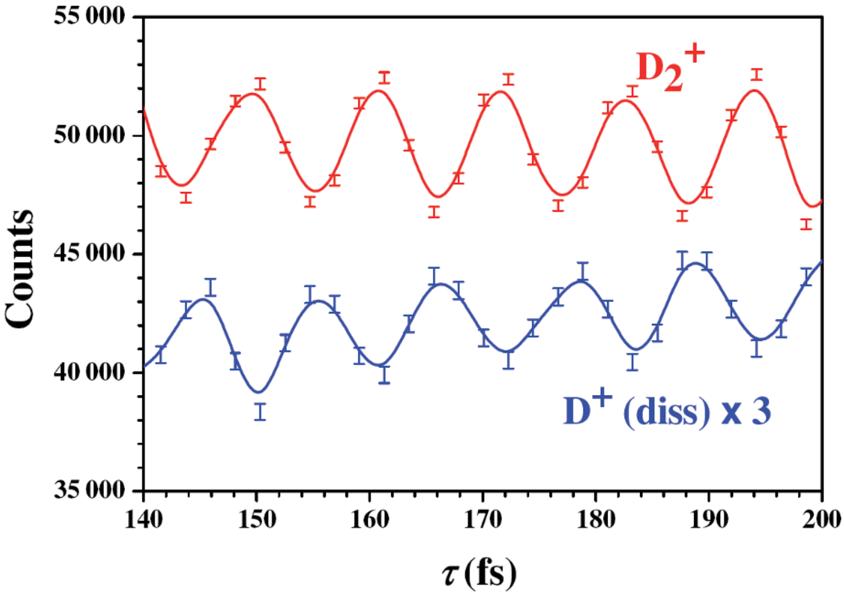

Fig. 6.10. Experimentally measured ion counts measured in a pump-probe experiment on D_2 using two identical 780 nm laser pulses with 7 fs FWHM duration. The peak intensity is $4\,(\pm 1) \times 10^{14}\,\mathrm{Wcm}^{-2}$. Shown are the counts for nondissociated D_2^+ (red) and dissociated D^+ (blue) ions [52].

of about 8 fs a clear oscillation signal of both ionization and dissociative ionization was found as can be seen in Fig. 6.10 [52]. The oscillation period is in very good agreement with the predicted one (when taking into account the mass scaling between H and D) and even the oscillation depth is in reasonable agreement with the theoretical prediction. Since the experiment was capable of following the oscillation over a very long time interval of up to 1200 fs, the expected long decoherence time is also confirmed.

The intensities used in the experiment were, however, slightly lower than the ones used in the theoretical work. Therefore, it was less clear, whether the wave packet formation was really due to the selective R-dependent depletion or due to bond softening. The latter, already discussed effect theoretically predicted in [38, 39] has so far not been experimentally verified for neutral molecules like H_2, and thus even this would certainly be an interesting outcome. However, since the general effect of bond softening is already known (though only for ions like H_2^+ but not for covalent neutral molecules like H_2), the selective depletion (termed *Lochfrass*) would be even more spectacular. In any case, it is of course very interesting to determine the exact mechanism of the wave packet formation. It turns out that the already discussed robustness of the formation process is the key, together with the impressive stability of the experimental set-up. As is shown in Fig. 6.9 for different pulse lengths and was also demonstrated with respect to the absolute carrier-envelope phase or wavelength of the laser pulse, the absolute phase of the oscillation signal of the pump-probe experiment is independent on the mentioned laser parameters. The same is valid for wave packets formed by bond softening. However, there is an almost maximum phase lag in between the wave packets created by the two different formation processes. As a consequence, it is possible to distinguish the two mechanisms by the absolute phase. In a very simple picture the origin of this phase lag may be understood in the following way, illustrated schematically with Fig. 6.11.

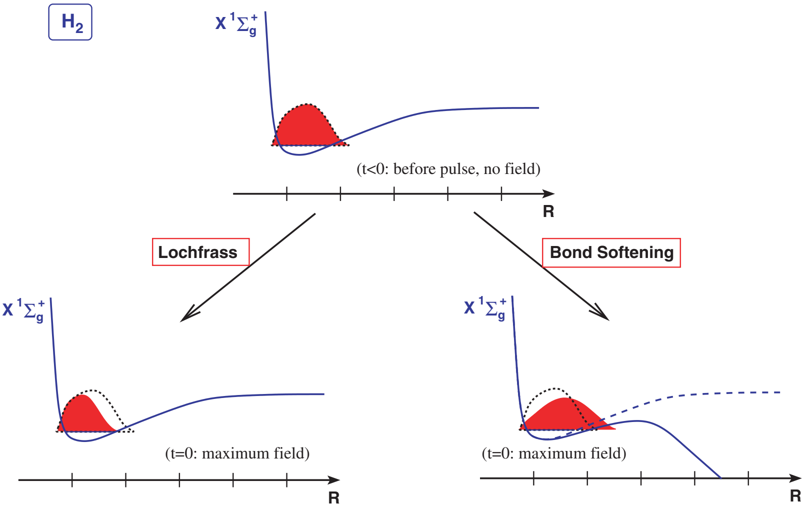

Fig. 6.11. Sketch of the two possible mechanisms responsible for the formation of a vibrational wave packet in the H_2 electronic ground state and their possible distinction by the absolute phase. In the case of *Lochfrass* the initial wave function is depleted at large R values and thus at $t = 0$ (maximum field strength) it is created at its inner turning point, moving initially to larger R. In the case of bond softening the wave packet flows over the field-distorted (lowered) potential well. At $t = 0$ (maximum field strength) it is at its outer turning point, moving initially to smaller R.

In the case of *Lochfrass*, the laser pulse depletes first the wave packet at the outer turning point. In the case of bond softening the wave packet escapes during the pulse over the field-distorted barrier. At the end of the laser pulse the wave packet created by bond softening is thus located with its maximum at the outer turning point and moves toward the inner one. In the case of *Lochfrass* the wave packet was depleted at the outer turning point and thus its maximum is located at the inner side of the potential well. The wave packet then starts moving toward the outer turning point. Therefore, the two creation mechanisms are distinguishable by the phase of the oscillation at zero delay time. This phase is, however, not directly experimentally accessible, since delay time zero means pump and probe pulses overlap completely in time. However, scaling the oscillation signal by the oscillation period and thus plotting the oscillation as a function of the number of oscillations, it is possible to extrapolate to time zero. Of course, this is only unambiguously possible, if the oscillation signal is very stable over many oscillation periods. Since this is the case, the experiment revealed that *Lochfrass* appears to be the dominant creation mechanism, see Fig. 6.12. In this figure the results of a theoretical simulation based on the bond-softening proposed in [38] and *Lochfrass* discussed in [51] are compared (on a relative scale) to the experimental results. In order to obtain very good agreement between experiment and theory, a small contribution of bond softening (in agreement with the theoretical prediction) has to be assumed.

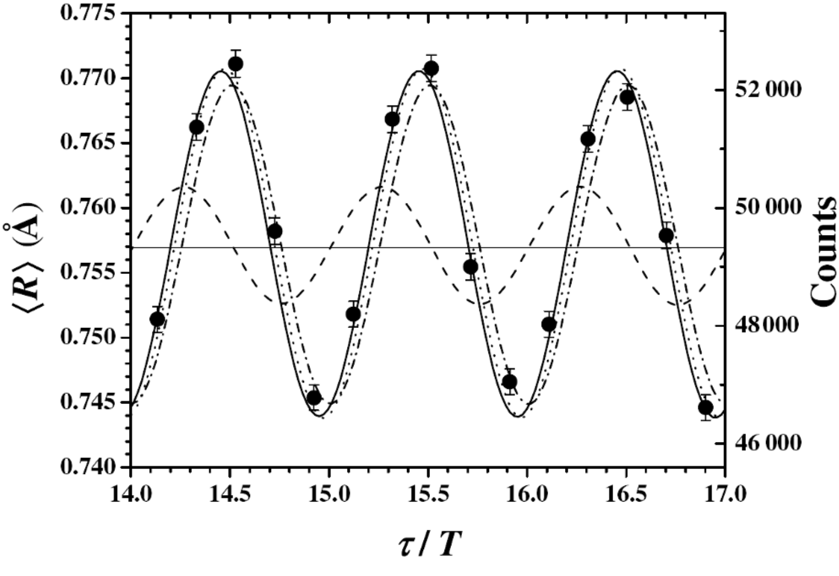

Fig. 6.12. Comparison of a numerical simulation of the R variation expected for *Lochfrass* (chain) or bond softening (dashed) only, and both effects (dotted) together. Also shown is the experimentally measured oscillation signal (dots) of the pump-probe experiment [52]. To guide the eye, a best-fit of the experimental data to a sinusoidal curve is also shown (solid).

Returning to Fig. 6.10, one notices a clear out-of-phase oscillation of the ionization (D_2^+) and the dissociative ionization (D^+) signals. Clearly, it is possible to control the two product channels by varying the delay time be-

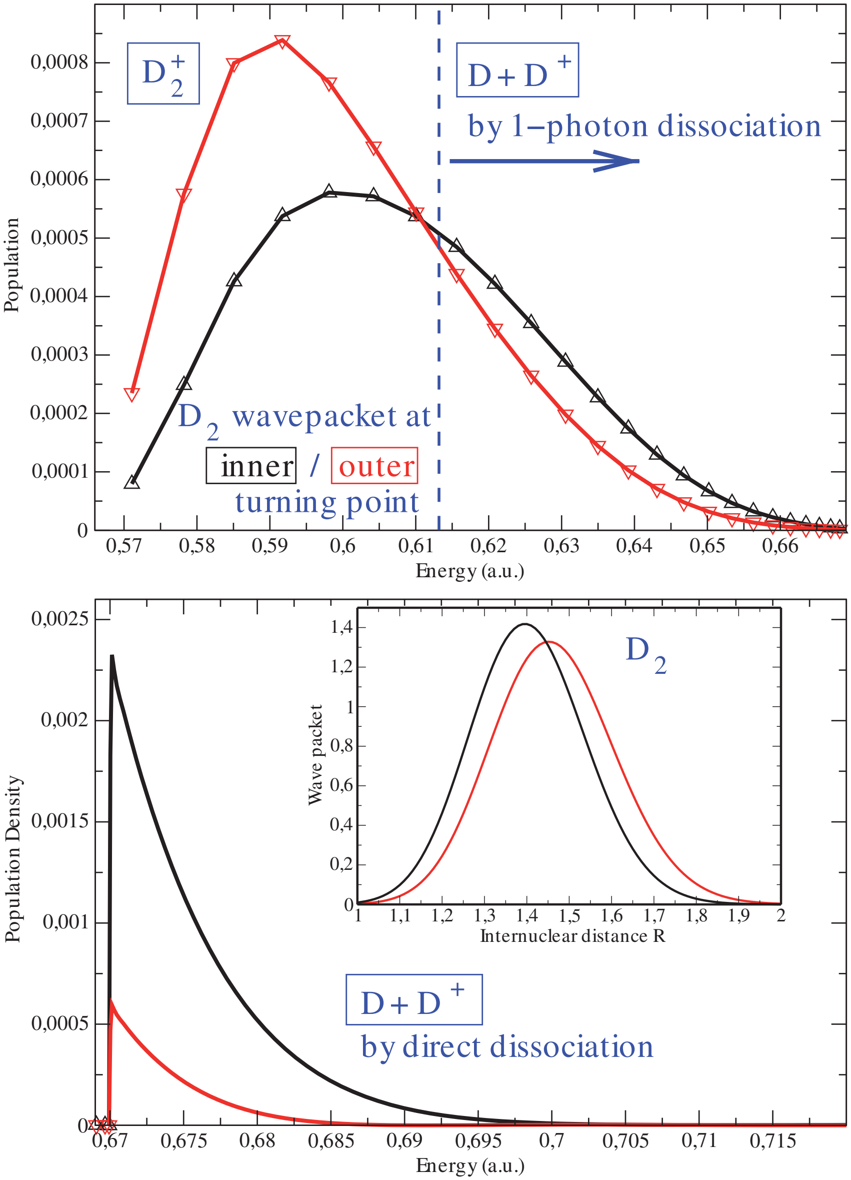

Fig. 6.13. Distribution over the vibrational states of D_2^+ following the laser-field ionization of the wave packet in the electronic ground state of D_2 (shown in the insert) at its inner (black) or outer turning (red) point. The upper spectrum shows the population of the field-free bound (nondissociative) states, the lower spectrum the continuous distribution in the dissociative continuum. The vertical dashed blue line indicates those states that can dissociate by one-photon absorption. (To guide the eye, also in the upper spectrum the discrete points are connected by lines.)

tween the pump and the probe pulses. Notably, depending on when the H_2 wave packet is probed, different products are preferentially produced. Even this phenomenon can be explained with the aid of the simple model proposed in [44] that describes the interplay between electronic and vibrational motion in strong fields. Analyzing not only the total ion rate of the pump-probe experiment as was done in [51], but predicting the vibrational distribution of the H_2^+ ion for the H_2 wave packet created by *Lochfrass* at its inner and outer turning points, it is possible to show that at the outer turning point not only the total ionization rate is larger than at the inner turning point, but also the vibrational distribution shifts to lower vibrational states, see Fig. 6.13. Therefore, at the outer turning point H_2^+ is preferentially formed in the low lying vibrational states that are harder to dissociate. At the inner turning point the total ionization rate is smaller, but the formed H_2^+ ions are preferentially formed in dissociative states or those states that can more easily dissociate. Since the H_2^+ wave packet formed in the pump pulse has practically no time to dissociate by passing over the field-suppressed barrier, it is most likely that (besides direct dissociation of those wave packet components that lie above the field-free potential barrier) dissociation occurs via one-photon absorption in the pedestal of the probe pulse. This is again in agreement with the simple theoretical model that predicts that the H_2^+ wave packet created at the inner turning point of the H_2 wave packet will populate preferentially those vibrational states that can directly or by one-photon absorption dissociate. Therefore, the dissociation signal has its maximum at the minimum of the ionization signal. In this context it may be noted that in another very recent theoretical work the enhancement and control of dissociative vs. nondissociative ionization of H_2 in intensive ultrashort laser pulses has been reported [53]. In contrast to the example discussed above, the process described in [53] takes place in the multi photon regime and involves VUV photons. In any case, these examples demonstrate the richness of the control scenarios in the strong-field regime.

6.3 Strong field chemistry and control

Dmitri A. Romanov and Robert J. Levis

6.3.1 Molecules in intense laser fields

When a 3-atomic or larger molecule interacts with an intense laser pulse a number of product channels may be accessed. Some of the potential outcomes are listed in Fig. 6.14 where coupling into the nuclear, electronic and nonlinear optical channels are delineated. Initial intuition suggested, incorrectly, that intense, short duration laser pulses interacting with polyatomic molecules would result primarily in multiphoton dissociation as shown in the first channel. Early experiments using intense nanosecond, picosecond and femtosecond pulses provided ample evidence for the second and third coupling channels in Fig. 6.14, which may be described as dissociative ionization and Coulomb explosion [54], respectively. Pulses of femtosecond duration have been shown to couple into electronic channels resulting in ionization without nuclear fragmentation for molecules like benzene and naphthalene [5]. In such experiments the energy in excess of the ionization potential (up to 50 eV!) [55, 56] couples mainly into the kinetic energy of the photoelectron. In terms of control experiments, the ability to produce intact ions at such elevated laser intensities suggested the possibility that intense lasers could be used to guide the dynamics of a molecule into a desired channel.

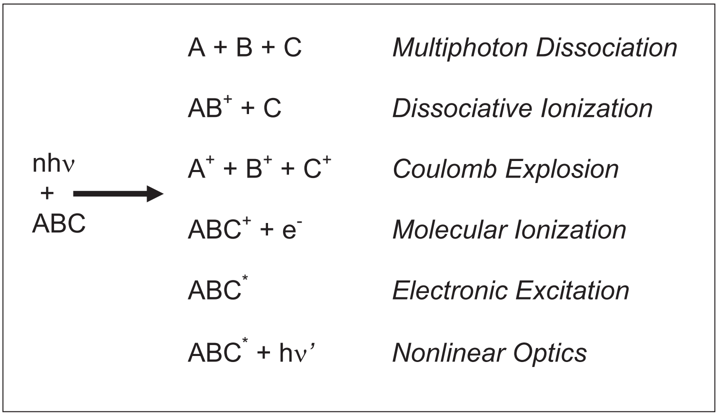

Fig. 6.14. Potential outcomes of the interaction of intense laser radiation with a molecule. At the present time the wavelengths used for the interaction range between 10 μm and 200 nm. The wavelengths employed in the studies reported here range between 750 and 850 nm with intensities of 10^{13}-10^{15} Wcm^{-2}

The relative importance of each product channel shown in Fig. 6.14 is dictated by the Hamiltonian for the molecule-radiation system. The understanding of the Hamiltonian for polyatomic molecules in general, and the more complex Hamiltonian for the interaction between strong fields and molecules in particular, is rather limited at the present time [7]. One would like to have high quality time-dependent calculations to model the strong field interaction, but these are simply intractable with current computational technology. Calculations for simple systems containing up to three protons and one or two electrons have been performed and these systems are reasonably well-understood [57–59]. For polyatomic systems, the number of degrees of freedom is too large for first-principles calculations. Thus, simple models have been employed to gain some insight into the mechanisms of interaction between intense laser pulses and atoms.

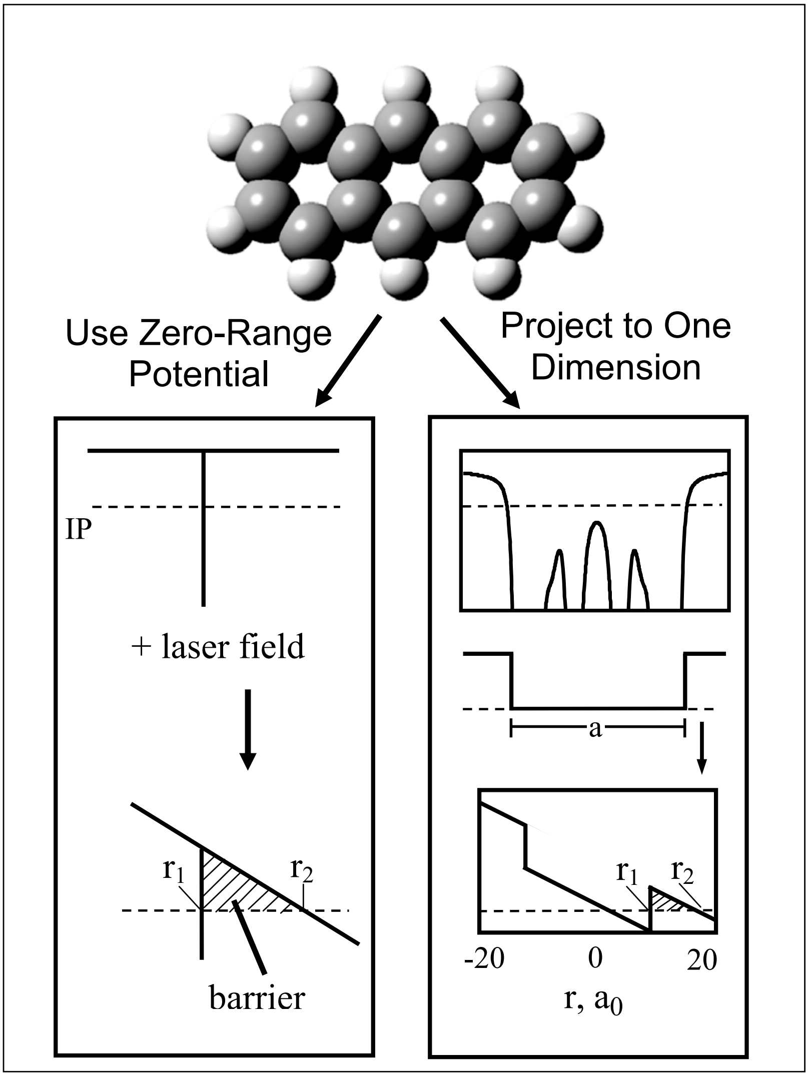

Fig. 6.15. A schematic of the structure-based model for representing molecules in intense fields. The presentation in the right hand panel is the zero-range model where only the ionization potential of the system is employed in calculations. The presentation in the left hand panel represents the use of the electrostatic potential of the molecule in determining an appropriate one-dimensional rectangular well to represent the spatial extent of the system. To compare the models an electric field of 1 V/Å is superimposed on each potential to reveal the barrier for tunnel ionization.

There is a hierarchy of models for representing molecules interacting with intense laser fields. The earliest models viewed the potential energy of interaction between the electron and the core as a delta function having a single state at the ionization potential of the system (called a zero-range potential) [22]. Subsequently, a Coulomb potential was employed for calculations in atoms [45, 60]. This was followed by a rectangular potential for molecules defined within the context of the structure-based model as shown in Fig. 6.15 [7, 23, 55, 61, 62]. The rectangular potential approximates the delocalization of electrons over the length scale of the molecular dimension by defining the width of the well to be equal to the characteristic length of the molecule. The characteristic length is defined as the largest distance between classical turning points in the three-dimensional electrostatic potential energy surface at the ionization potential of the molecule. The height of the rectangular well is the ionization potential of the molecule. A further advance incorporated time-dependence into the radiation-molecule interaction to go beyond the quasi-static regime [24].

6.3.1.1 Electronic dynamics of molecules in intense laser fields

To describe the mechanisms of strong field control of chemical processes it is important to consider the influence of the intense laser field on electrons in the molecule. For instance, we will see that bound electrons can gain significant ponderomotive energy ($\approx$ 1-5 eV) during the pulse and eigenstates can shift by similar energies [63]. In the case of the interaction of a laser pulse with a molecule, the appropriate starting point is the Hamiltonian for a multielectron system interacting with an electromagnetic field:

$$\begin{aligned}H = \frac{\boldsymbol{P}_c^2}{2M} + \frac{1}{2m_e}\sum_{I=1}^{Z}\boldsymbol{P}_I^2 + \frac{1}{m_n}\sum_{i>j=1}^{Z}\boldsymbol{P}_i\cdot\boldsymbol{P}_j + V(x_1,\ldots,x_i,\ldots,x_c) + \\ \frac{e}{m_e c}\boldsymbol{A}(\boldsymbol{x_c},t)\times\sum_{i=1}^{Z}\boldsymbol{P}_i + \frac{Ze^2}{2m_e c^2}\boldsymbol{A}^2(\boldsymbol{x_c},t) \qquad (6.7)\end{aligned}$$

where $\boldsymbol{P}$ is momentum, V is the potential energy as a function of position, Z is the nuclear charge, and $\boldsymbol{A}(\boldsymbol{x_c},t)$ is the vector potential of the laser radiation. The first four terms describe the field free motion of the system. The last two terms describe the effect of the laser radiation on the population of eigenstates and corresponding shifts in the eigenstates of the system. In the electric field gauge the last term becomes:

$$\frac{Ze^2}{2m_e\omega_L^2}\boldsymbol{F}^2(\boldsymbol{x_c},t) \qquad (6.8)$$

where $\boldsymbol{F}$ is the electric field of the laser, and ω_L is the frequency of the laser. The average of this term over the period of oscillation for linearly polarized light is known as the ponderomotive potential U_p (see (6.4) in Sect. 6.1). In strong fields this term shifts all eigenstates upward in energy equally by U_p. A differential shifting of eigenstates results from the $\boldsymbol{A} \cdot \boldsymbol{P}$ term. To first and higher order, the $\boldsymbol{A} \cdot \boldsymbol{P}$ term may used to describe allowed transitions of amplitude between eigenstates. To second and higher order this term will describe differential shifting of the eigenstates. The magnitude and sign of the shift of a given state is dependent on the wavelength and the electronic structure of the system. Pan et al. [64] have derived expressions for the shifting of the ground state and Rydberg/continuum states of a model system. A lowest nonvanishing order perturbation theory treatment yields the ground ($\mathit{\Delta} E_g$) and Rydberg level ($\mathit{\Delta} E_R$) energy shifts as [64]:

$$\begin{aligned} \mathit{\Delta} E_g &= -\frac{Ze^2F_0^2}{4m_e\omega_L^2} - \frac{1}{2}\alpha F_0^2 \\ \mathit{\Delta} E_R &\approx 0 \end{aligned} \tag{6.9}$$

where α is the ground state polarizability. The first term in (6.9) is the negative of the ponderomotive potential U_p. The second term is equivalent to the dc Stark shift. This treatment is valid when the ground state is deeply bound and separated from adjacent eigenstates by many times the photon energy, $h\nu$ (the low frequency approximation). This is valid for most atoms and molecules investigated with near infrared or longer wavelength light. High lying bound states and all continuum states experience no $\boldsymbol{A} \cdot \boldsymbol{P}$ shift whereas deeply bound states of the atom experience a much greater, negative shift [65]. The pertinent shift in the states as a function of the terms in the Hamiltonian in the long wavelength limit is summarized in Fig. 6.16.

The laser intensities employed in recent high field experimental manipulation of chemical reactivity range up to $5 \times 10^{14}\,\mathrm{Wcm}^{-2}$. This corresponds to ponderomotive shifts up to 10 eV with similar shifts in the separation of the ground and excited state potential energy levels. The laser employed in these investigations has a period of 2.5 fs and an envelope with FWHM of 60-170 fs corresponding to at least a several hundred significant oscillations in the electric field vector interacting with the molecule. The states of the molecule undergo an associated oscillation in the splitting between energy levels that may result in periodic excitation on a time scale of the period of the laser. This dynamic shifting of energy levels implies that there will be transient field-induced resonances (or Freeman resonances) [66]. Evidence for these resonances in the case of molecules has been obtained by measuring the strong field photoelectron spectroscopy of a number of molecules including acetone, acetylene [63], water, benzene and naphthalene [67]. The oscillatory nature of the intense laser excitation also leads to above threshold ionization (ATI) peaks in the photoelectron spectrum [2]. These are denoted by peaks spaced by the photon energy extending to many photons above the minimum number required for ionization.

An important consideration for the control of chemical reactivity in the strong field regime is the order of the multiphoton process during excitation.

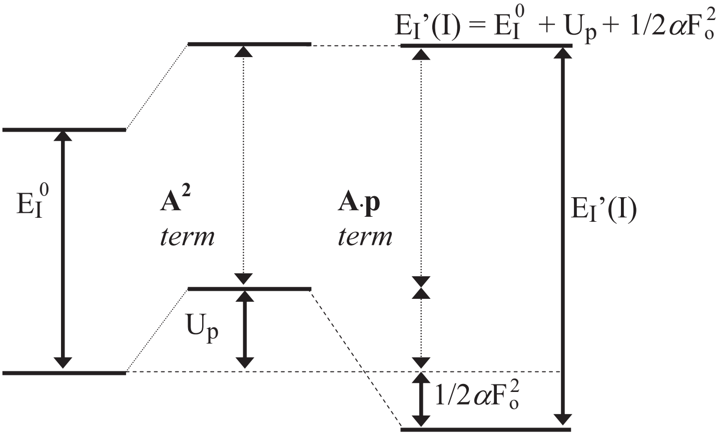

Fig. 6.16. The effect of various terms in the Hamiltonian for a charged particle in an oscillating electromagnetic field is shown. The ionization potential of the system remains unchanged by the $\boldsymbol{A}^2$ term as all states are raised equally. The $\boldsymbol{A} \cdot \boldsymbol{P}$ term lowers the ground state of the system by an amount equal to the $\boldsymbol{A}^2$ term plus an additional amount due to the induced polarization of the system. The net result is an increase in the ionization potential by an amount approximately equal to the ponderomotive potential of the laser pulse.

This order indicates the maximum number of photons that are available to drive a chemical reaction. Some indication of the number of photons involved in the strong field excitation process can be gleaned from measurements of strong field photoelectron spectra. Figure 6.17 displays the photoelectron kinetic energy distribution for benzene with the energy axis rotated by 90 degrees. The energy scale has been offset to include the energy of the ground and ionization potential of the molecule in the absence of the strong electric field. The arrows on the Figure represent the photons involved in both exceeding the ionization potential and in creating the ATI photoelectron distribution. At least six photons are required to surmount the ionization potential of benzene. Recall that in the presence of the strong electric field, the ionization potential will increase by an amount greater than the ponderomotive potential, further increasing the actual number of photons involved in the excitation process. At the intensity of $10^{14}\,\mathrm{Wcm}^{-2}$ in this measurement, on the order of 10 photons may be absorbed to induce the photoelectron spectra shown. Including the photons required to reach the ionization potential, this means that approximately 20 photons may be involved in the excitation process. With the shaped pulses used in the experiments described in Sect. 6.3.2, the intensities are lower and on the order of 10 or fewer photons are likely involved in the excitation process.

Several other methods have been developed to predict the ionization probability of molecules. One is based on discretizing a molecule into a collection

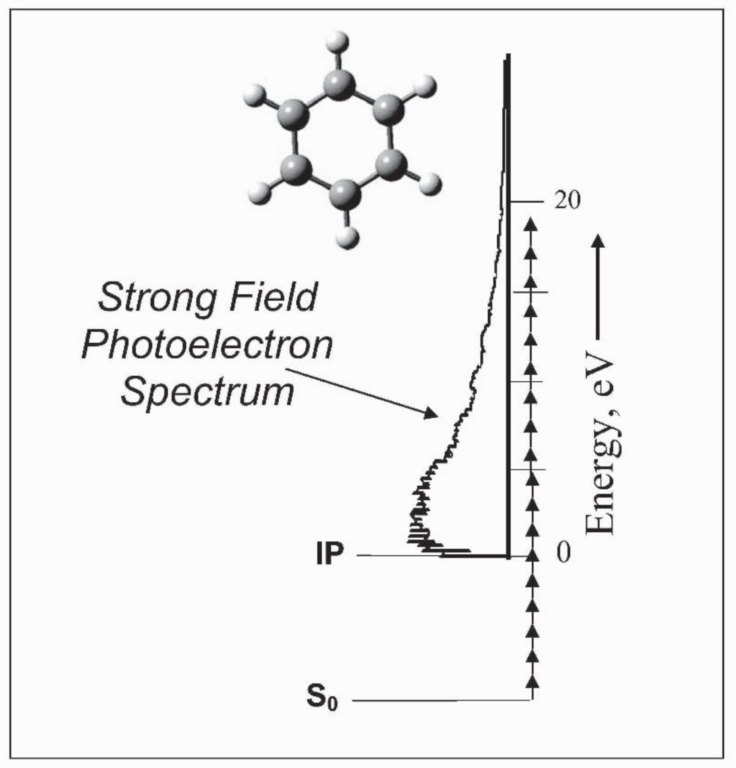

Fig. 6.17. The strong field photoelectron spectrum for benzene shown on an energy axis that includes the photons necessary to induce ionization. The photoelectron spectrum was obtained using $2 \times 10^{14}\,\mathrm{Wcm}^{-2}$, 800 nm radiation of duration 80 fs. The quantum energy of the photons are shown to scale and indicate that 10-20 photons are available to drive excitation processes in the strong field excitation regime. In addition, uncertainty broadening of the pulse will also produce a distribution of allowed photon energies that approaches the photon energy when multiphoton processes of order ten are approached.

of atomic cores that individually interact with the strong laser field and emit electrons [68, 69]. In this model, a carbon atom, for instance, is represented by an atom with an effective potential. The ionization probability is then a function of the individual ionization probabilities from atoms with opportunity for quantum interference during the ionization event. Unfortunately, the method must be parameterized for each molecule at the present time. The second method under development employs S-matrix theory [70] to calculate the ionization probability for atoms and molecules. This method focuses on the interference of the outgoing electron wave. Predictions about relative ionization probabilities are based on the symmetries of the highest occupied molecular orbital.

6.3.1.2 Nuclear dynamics of molecules in intense laser fields

The response of a molecule to a time-dependent electric field is the means by which chemical reactivity is controlled in these experiments. In the case of weak laser fields the response can be calculated with reasonable accuracy [71–73]. In the case of strong fields, the situation is much more complex, but the dynamical possibilities are much richer. In principle, the nuclear dynamics in strong laser fields could be determined using exact numerical solutions of the time-dependent Schrödinger equation. Such solutions are possible only for the simplest of molecules at the present time [57–59]. In fact, the bulk of such simulations have been performed using a one-dimensional model for the H_2^+ system [31, 74, 75]. These calculations show the presence of non-Born-Oppenheimer electron-nuclear dynamics. Since the nuclei move considerably on the time scale of the laser pulse, electronic wave functions are necessarily coupled with nuclear motion. Three distinct final states have been observed in strong field (no pulse shaping) mass spectra of polyatomic molecules: production of intact molecular ion, ionization with molecular dissociation, and removal of multiple electrons to produce Coulomb explosion [7]. The hallmark of the latter process is production of ions substantial ($> 5\,\mathrm{eV}$) kinetic energy. The presence of Coulomb explosion has been shown to depend on charge resonance-enhanced ionization (CREI) [76] which becomes the dominant mechanism at large critical internuclear distances. Interestingly, the production of high charge states in molecular clusters can be controlled using pump-probe excitation schemes [77].

At intensities that are lower than the threshold for multielectron ionization, the majority of molecules display some fraction of intact ionization. This phenomenon is not expected intuitively because the ionization processes are not resonant with low order multiples of the fundamental frequency implying that intense pulses must be employed for excitation. None the less, many molecules have been investigated to date and all appear to provide some degree of intact molecular ionization when 800 nm excitation is employed. The mechanism behind this ionization appears to involve suppression of ladder switching coupled with coherent excitation of electronic wave functions. The state of this subject has been reviewed in [7, 78, 79].

To measure the amount of energy that may couple into the nuclear degrees of freedom during the intense laser excitation event, we have investigated [56] the kinetic energy release in H^+ ions using both time-of-flight and retarding field measurements. A typical time-of-flight mass spectroscopy apparatus employed to make such measurements is shown in Fig. 6.18. In the series benzene, naphthalene, anthracene, and tetracene the most probable kinetic energy in the measured distributions was observed to increase as the characteristic length of the molecules increased as shown in Fig. 6.19. The corresponding retarding field measurements are shown in Fig. 6.20. Again the coupling into nuclear degrees of freedom was observed to increase in the larger molecules. The most probable kinetic energies increased from 30 eV for benzene to 60 eV

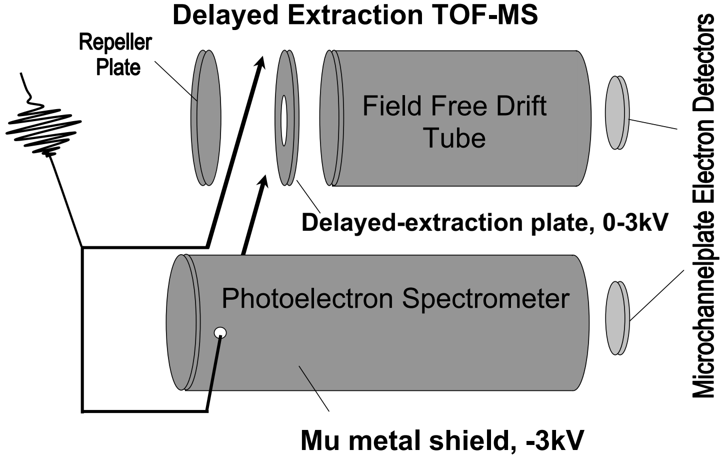

Fig. 6.18. Schematics of the photoelectron spectrometer and the time-of-flight ion detector used for measuring the kinetic energy distribution and molecular weight of the product ions.

for tetracene when a $1.2 \times 10^{14}\,\mathrm{Wcm}^{-2}$ laser excited the molecules. In terms of providing an enabling capability for strong field control, these results suggest that up to 80 photons may be involved in the excitation process when a molecule such as tetracene is excited under strong field conditions.

A general observation after ionization of large polyatomic molecules is the measurement of an enhanced degree of dissociation as the length of the molecule increases. This was first attributed to field-induced effects [5] without a quantitative model. Recently, a strong field nonadiabatic coupling model has been introduced to account for the enhanced coupling into nuclear modes in molecules with increasing characteristic length [24]. This excitation is akin to plasmon excitation where the precise energy of the resonance depends on the coherence length and binding energy of the electrons and the strength and frequency of the driving field. The model considers the amplitude of electron oscillation in comparison with the length of the molecule. If the amplitude of oscillation is small, the molecule may first absorb energy nonresonantly and then ionize from the excited states. The amplitude of the electron oscillation in an laser field is given by $a_{osc} = F/\omega_L^2$. In the event that the $a_{osc} < \ell$, where ℓ is the characteristic length of the molecule, the electron gains ponderomotive energy from the laser. Given an energy level spacing of Δ_0, the probability of nonadiabatic excitation within the Landau-Zener model becomes $\exp(-\pi\Delta_0^2/4\omega_L F\ell)$. As described in [22], the threshold for nonadiabatic excitation (when $\Delta_0^2 = \omega_L F\ell$) of a 4 eV transition for a system having $\ell = 13.5\,\text{Å}$ with 700 nm radiation occurs at $5.6 \times 10^{12}\,\mathrm{Wcm}^{-2}$. This theory implies that the probability for exciting nuclear modes in large molecules with delocalized electronic orbitals increases monotonically with characteristic length as

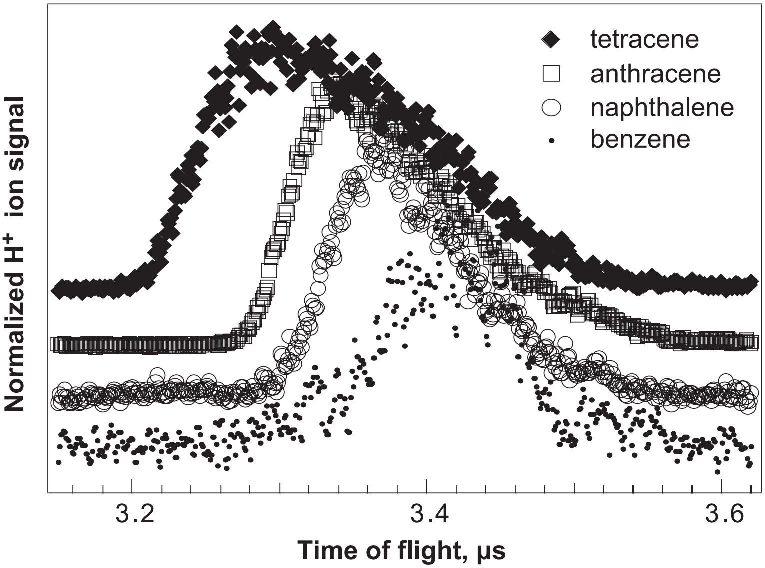

Fig. 6.19. Time-of-flight distributions for the H^+ ions for benzene, naphthalene, anthracene and tetracene after excitation using 2×10^{14} Wcm^{-2}, 800 nm radiation of duration 80 fs. The time of arrival distributions were measured by allowing the ions to drift in a field free zone of length 1 cm prior to extraction into the drift tube. In this experiment, earlier arrival times denote higher kinetic energies.

observed experimentally [5, 24]. The theory also suggests that intact molecular ionization will increase with increasing excitation wavelength for large molecules and this has been confirmed [24].

In this simple model, the extent of the excitation and ionization processes is singularly determined by the spatial size of the molecule. Experiments, however, reveal a much more complex picture of the nonadiabatic excitation mechanism and the corresponding products in real polyatomic molecules. One reason for this complexity is that a large molecule actually has two energy scales: (i), the gap between the ground state and the excited state manifold; and (ii), the gap between energy levels in the excited state manifold. The former is usually much greater than the inter-level distances in the manifold. As a result, the first step in the excitation process requires a special treatment. Accordingly, a consistent model of dissociative ionization caused by nonadiabatic excitation has been developed [80, 81] that is based on three major elements: (i), the doorway state for the nonadiabatic transition into the excited state manifold (the state that has the maximum transition dipole matrix element with the ground state); (ii), multielectron polarization of the ground state and the doorway state (that is, the dynamic Stark shift that strongly modifies the transition rate); (iii), sequential energy deposition in the neutral

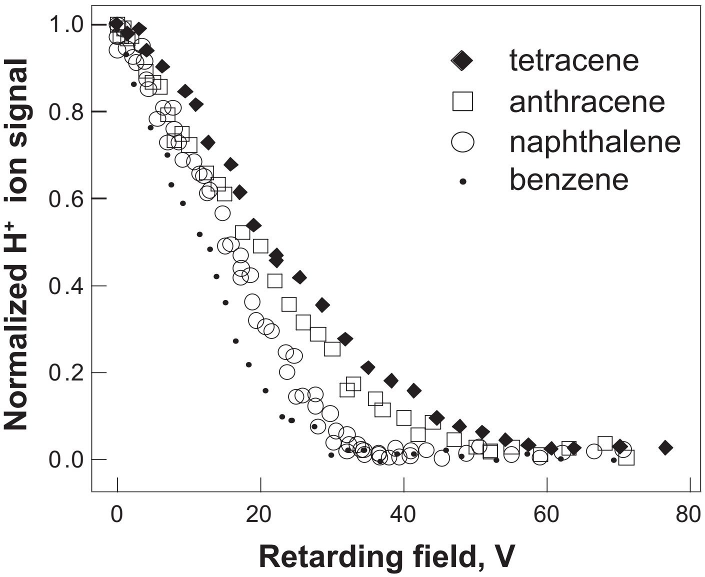

Fig. 6.20. Retarding field measurement of the H^+ ion kinetic energy distributions arising from benzene, naphthalene, anthracene and tetracene after excitation using $2 \times 10^{14}\,\mathrm{Wcm}^{-2}$, 800 nm radiation of duration 80 fs. The measurements reveal that as the characteristic length of the molecule increases, the cutoff energy increases monotonically.

molecules and corresponding molecular ions (for large molecules, the ionic transition dipole and the dynamic Stark shift are usually greater than those for the neutral molecule, while the bottleneck energy gap between the ground state and the doorway state is typically smaller) [82]. In this model, the first excitation stage leads to ionization; the second (and subsequent) stages result in the molecular ion fragmentation.

The predictions of the model have been compared with experimental data on dissociative ionization for two series of related molecules as a function of laser intensity. In Series a, benzene, naphthalene, anthracene, and tetracene, the characteristic length of the aromatic molecules increases from benzene to tetracene; along with the extent of π-electron delocalization that should directly affect the dipole transition matrix element and the energy distance for the electronic excitation from the ground state to the doorway state. In Series b, 1,2,3,4,5,6,7,8-octahydroanthracene (OHA), 9,10-dihydroantracene (DHA), and anthracene, the characteristic lengths are similar but the extent of π-delocalization nevertheless increases from OHA to anthracene, with increasing number of unsaturated aromatic rings. The mass spectra were obtained at laser intensities between $0.1 \times 10^{13}\,\mathrm{Wcm}^{-2}$ and $25.0 \times 10^{13}\,\mathrm{Wcm}^{-2}$. The extent of nonadiabatic energy transfer and the subsequent molecular frag-

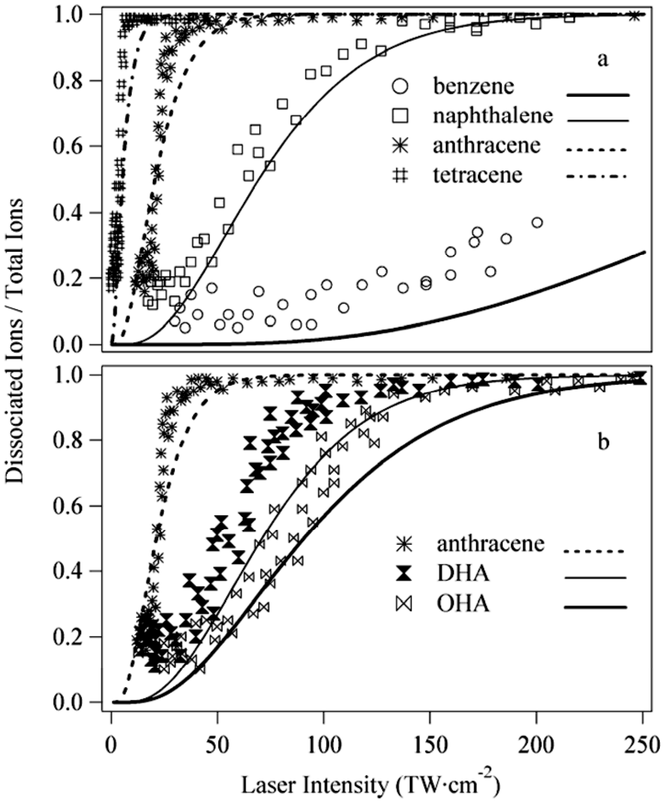

Fig. 6.21. Fragmentation fraction and nonadiabatic multielectron dynamics calculation: a) benzene-naphthalene-anthracene-tetracene series; b) anthracene-DHA-OHA series. The curves show the calculated fraction of the molecular ions excited nonadiabatically by the end of a laser pulse (integrated conditional probabilities of two-stage nonadiabatic excitation).

mentation was quantified by plotting the ratio of fragment ion signal to the total ion signal vs. the laser intensity. The plots in Fig. 6.21 reveal that the onset of extensive dissociation occurs at lower laser intensities with increasing molecular size for Series a and increasing degree of unsaturation in Series b. Note that this observation apparently runs contrary to the conventional multiphoton perturbative picture. Indeed, for larger molecules (tetracene, anthracene) the number of photons required for electronic excitation decreases and thus the intensity dependence should be of lower order than for smaller molecules (naphthalene, benzene). However, the molecular excitation/double ionization curves calculated as functions of the laser intensity according to the above-delineated model, agree quantitatively well with the experimental data.

(Fig. 6.21) This agreement is especially remarkable because the all the model operates with the transition dipoles, energy gaps, and dynamic polarizabilities taken from ab initio calculations and thus does not contain any fitting parameters.

Additional information on the process of the nuclear subsystem excitation and possibilities to control this process can be gleaned from the kinetic energy distributions of the ionized fragments released after excitation [83, 84]. From this standpoint, the most informative fragments are the positive hydrogen ions (protons). Because of their small mass, they (i) move substantially on the timescale of the pulse duration; and (ii) acquire more kinetic energy than their massive counterparts. In large molecules protons usually occupy peripheral positions thus having an unobstructed outgoing trajectory. As an example of such proton-related information, we present in Fig. 6.22 the energy distributions of protons resulting from the dissociative ionization (Coulomb explosion) of anthracene subjected to intense laser pulses ($\sim 10^{14}\,\mathrm{W cm^{-2}}$ intensity, 800 nm wavelength, and 60 fs duration) and demonstrate counterintuitive details of the pulse-driven fragmentation process. Two distinct regimes of proton ejection dynamics were observed: at lower laser intensities the proton kinetic energy release increases rapidly with the laser intensity, only to saturate at higher laser intensities. Most surprisingly, the proton kinetic energies occur to exceed 30 eV; actually, the cutoff of the energy distribution reaches 52 eV. To account for this excessive energy, a strong-field charge localization model was suggested. It assumes that nonadiabatic dynamics of charge distribution in a large (multiply) ionized molecule leads to charge localization on one side of the molecule, sustained through successive ionizations of the molecular ion. The model explains quantitatively the dependence of the proton kinetic energy on the laser intensity (Fig. 6.22). Dissociative ionization of a polyatomic molecule enabled by long-lived charge localization is a specific strong-field phenomenon that can well serve as a useful physical mechanism of electron-nuclear dynamics control.

Yet another type of strong-field electron-nuclear dynamics emerges from comparison of proton kinetic energy distributions of two similar molecules: anthracene and 9,10-anthraquinone as illustrated in Fig. 6.23 [84]. These distributions are similar at lower laser intensities but differ significantly at higher intensities: starting at $\sim 9.0 \times 10^{13}\,\mathrm{W cm^{-2}}$, a high-energy mode with a cutoff value extending to approximately $83 \pm 3\,\mathrm{eV}$ forms in the anthraquinone spectra. These higher kinetic energies are not due to higher degree of ionization, because the rate of nonadiabatic excitation and ensuing ionization of anthraquinone is actually even smaller than that for anthracene. Instead, the high-energy mode is explained by restructuring of the anthraquinone molecule prior to its Coulomb explosion. Model dynamical calculations based on Gaussian 03 geometry optimization and local charge distributions show that anthraquinone can form a field-dressed enol zwitterion where one of the "inner" protons (1,8,4, or 5 in Fig. 6.23) migrates to oxygen creating an O-H bond. The strong-field polarization of the zwitterion in the O-O direction provides

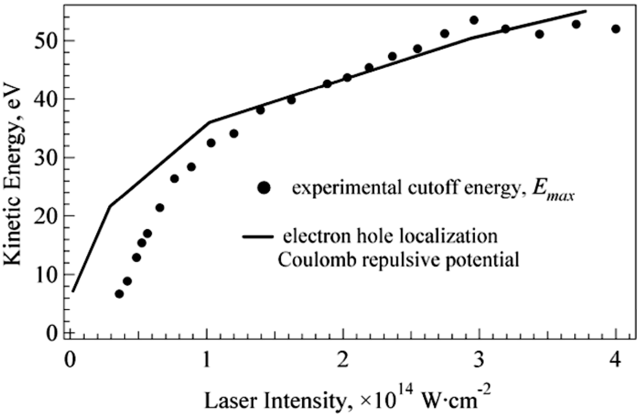

Fig. 6.22. The cutoff values of the proton kinetic energy distributions and model maximum Coulomb potential expelling protons, as functions of the laser intensity.

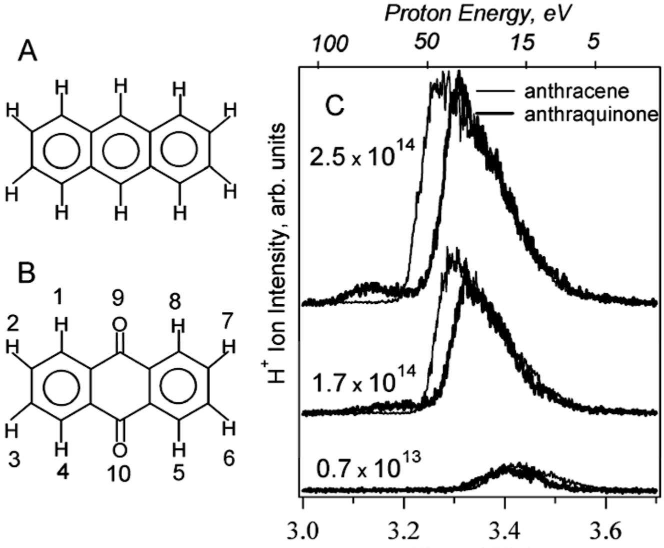

Fig. 6.23. Structures of anthracene (A) and 9,10-anthraquinone (B) with labeled proton positions. C: time-of-flight distributions of protons ejected from anthracene (thin line) and anthraquinone (thick line) at three different laser intensities (Wcm^{-2}).

the necessary degree of charge separation and ensuing nonadiabatic charge localization to eject the observed high-energy protons. These results demonstrate that modification of nuclear potentials of a polyatomic molecule by a strong oscillating electric field can force dynamic nuclear rearrangement into metastable positions that are quasi-bound in the presence of the field. (Note that this effect differs essentially from weak-field rearrangements, where one-photon electronic transition is followed by slow internal conversion on excited potential energy surfaces; it is rather analogous to bond softening in diatomic molecules during an intense laser pulse.) Thus, direct manipulation of intramolecular nuclei motion can be achieved in polyatomic molecules by strong laser fields.

Whether the nonadiabatic excitation can be controlled remains an open question at the present time. The present successes [85–87] in controlling chemical reactivity suggest that nonadiabatic processes either are not significant or that the closed loop control method is able to effectively deal with this excitation pathway.

6.3.2 Strong field control using tailored laser pulses

The use of strong fields to control chemistry is quite new, while the area of coherent control research has broad foundations [88–90] (see also Chapter 2, Sect. 2.4). The essence of the control concept in terms of optical fields and molecules is captured by the following transformation goal:

$$|\psi_i\rangle \xrightarrow{F(t)} |\psi_f\rangle \tag{6.10}$$

where an initial quantum state $|\psi_i\rangle$ is steered to a desired final state $|\psi_f\rangle$ via interaction with some external field $F(t)$. As a problem in quantum control, the goal is typically expressed in terms of seeking a tailored laser electric field $F(t)$ that couples into the Schrödinger equation:

$$\mathrm{i}\hbar \frac{\partial}{\partial t} |\psi\rangle = [H_0 - \mu F(t)] \, |\psi\rangle \tag{6.11}$$

through the dipole μ. The goal is to create maximum constructive interference in the state $|\psi_f\rangle$ according to (6.10), while simultaneously achieving maximal destructive interference in all other states $|\psi_{f'}\rangle$, $f' \neq f$ at the desired target time T. A simple analogy to this process is the traditional double slit experiment [91]. However, a wave interference experiment with two slits will lead to only minimal resolution. Thus, in the context of quantum control, two pathways can produce limited selectivity when there are many accessible final states for discrimination. Rather, a multitude of effective slits should be created at the molecular scale in order to realize high quality control into a single state [92], while eliminating the flux into all other states.

The requirement of optimizing quantum interferences to maximize a desired product leads to the need for introducing an adjustable control field $F(t)$

having sufficiently rich structure to simultaneously manipulate the phases and amplitudes of all of the pathways connecting the initial and final states. Construction of such a pulse is currently possible in the laboratory using the technique of spatial light modulation [93, 94]. However, calculation of the time-dependent electric fields to produce the desired reaction remains a problematic issue for chemically relevant reactions. Unfortunately, solution of the Hamiltonian at the Born-Oppenheimer level remains largely unknown for polyatomic molecules, and this severely limits the ability to perform a priori calculations at the present time. Even if the field free molecular Hamiltonian were known, the highly nonlinear nature of the strong field excitation process effectively removes all possibility of calculating an appropriate pulse shape in this regime. Thus we are left with the following conundrum: If the design can be carried out reliably, then the physical system will likely not be of much interest, while for interesting physical systems, reliable designs can not be performed. The method of closed-loop control for laser-induced processes [95] offers a way to surmount our lack of knowledge of the Hamiltonian to find appropriate pulse shapes, $F(t)$.

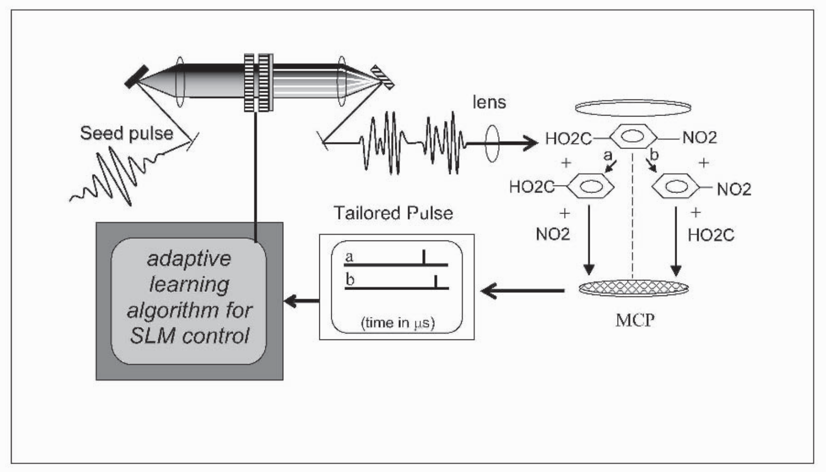

Fig. 6.24. A schematic of the closed loop apparatus for tailoring the time-dependent laser fields to produce the desired reaction product. In this scheme an algorithm controls the spatial light modulator that produces a well-defined waveform. The tailored light pulse interacts with the molecular sample to produce a particular product distribution. The product distribution is rapidly measured using time-of-flight mass spectrometry and the results are fed back into the control algorithm. The same closed-loop concept with other sources or detectors can be applied to control a broad variety of quantum phenomena.

To implement the optical control experiment (OCE) closed-loop control paradigm in the strong field regime three technologies are combined: (1) regenerative amplification of ultrashort pulses; (2) pulse shaping using spatial light modulation; and (3) some feedback detection system, (i.e. time-of-flight mass spectral detection in the experiments presented here). An overview of this implementation of the closed-loop control experiment is shown in Fig. 6.24. Briefly, the experiment begins with a computer generating a series of random, time-dependent laser fields (forty such control pulses are employed in the experiments presented here). In some cases prior estimates for fields might be available by design or from related systems to introduce specific trial field forms. Each of the control pulses is amplified into the strong field regime and subsequently interacts with the gas phase sample under investigation. Products are measured using time-of-flight mass spectrometry and this requires approximately $10\,\mu$s to detect all of the ion fragments. The mass spectra are signal averaged with a number of repeats for the same pulse shape and analyzed by the computer to determine the quality of the match to the desired goal. The remainder of the control fields sequentially interact with the sample and the fitness of the products are also stored on a computer. After each of the forty control fields have been analyzed in terms of the product distribution, the results of the fitness are employed to determine which fields will be used to create the next set of laser pulses for interaction with the sample. The system iterates until an acceptable product distribution has been achieved.

6.3.2.1 Trivial control of photochemical ion distributions

We first consider whether manipulation of the dissociation distribution can be achieved by simple alteration of either pulse energy or pulse duration. These are termed trivial control methods and in either case, there is no need to systematically manipulate the relative phases of the constituent frequency components. Pulse energy modulation is achieved here using a combination of a polarization rotator and beam splitter or by the use of thin glass cover slips to reflect away several percent of the beam. Pulse duration control can be implemented by either restricting the bandwidth of the seed laser or by placing a chirp onto the amplified pulse in the compressor optics.

Investigations of trivial control suggest that the ionization/fragmentation distribution can often be manipulated by altering either pulse energy or pulse duration. As an example, Fig. 6.25 shows the mass spectral distributions measured for p-nitroaniline as a function of either pulse duration (Fig. 6.25a) or pulse energy (Fig. 6.25b). In the case of the transform limited mass spectrum at $10^{14}\,\mathrm{Wcm}^{-2}$, there are many features in the mass spectrum corresponding to production of the $\mathrm{C}_{1-5}\mathrm{H}_x^+$ fragments. There is a minor peak at $m/e = 138\,\mathrm{amu}$ corresponding to formation of the parent molecular ion. We observe that when the pulse duration is increased the fragmentation distribution shifts toward lower mass fragments. This indicates an enhanced opportunity for ladder switching during the excitation process. Ladder switching allows facile excitation of the internal modes of the molecule [7]. Increasing the pulse duration also leads to lowering the pulse intensity. Alternatively to

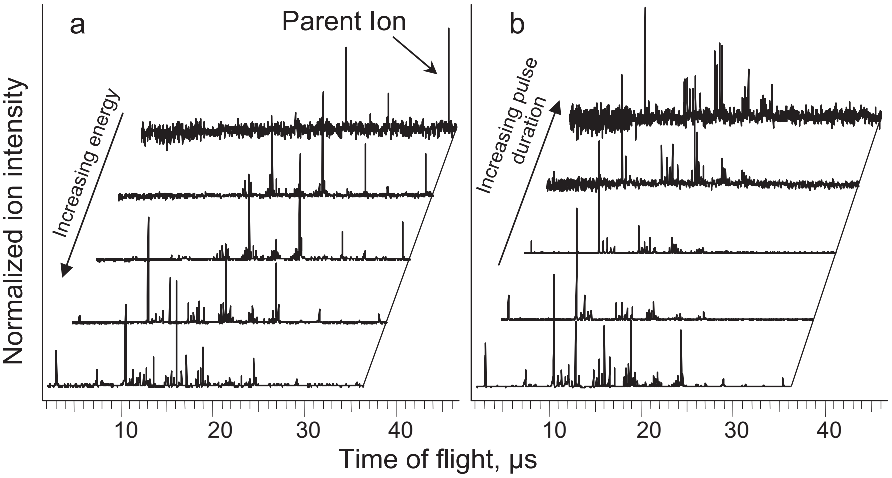

Fig. 6.25. Time-of-flight ion spectra of p-nitroaniline after excitation using pulses centered at 790 nm, of duration 80 fs. In panel a the pulse energy was varied from 0.60 to 0.10 mJ/pulse, the pulse duration was 80 fs. In panel b the pulse duration was varied from 100 fs to 5 ps, the pulse energy was 0.60 mJ/pulse.

lower the pulse intensity, the pulse energy can be reduced. When this form of trivial control is implemented, a completely different mass spectral distribution is obtained, as shown in Fig. 6.25b. When the intensity is reduced by a factor of 5 the parent molecular ion becomes one of the largest features in the mass spectrum. These results suggest that in any control experiment a series of reference experiments probing the products as a function of pulse energy and duration are necessary to rule out the possibility of trivial effects.

6.3.2.2 Closed-loop control of selective bond cleavage processes

Closed-loop control in the strong field regime has now been demonstrated on a series of ketone molecules [85]. We begin with acetone as a simple polyatomic system. Fig. 6.26 displays the transform limited mass spectrum resulting from the interaction of acetone vapor with a pulse of duration 60 fs and intensity 10^{13} Wcm^{-2}. There are a number of mass spectral peaks corresponding to various photoreaction channels as summarized in scheme I. Channel (a) corresponds to simple removal of an electron from the molecule to produce the intact acetone radical cation at $m/e = 58$. As noted in Sect. 6.1, the ability to observe the intact molecule in the mass spectrum reveals that not all of the excitation energy necessarily couples into nuclear modes. The second pathway, (b), observed is cleavage of one methyl group to produce the CH_3CO and methyl ions. The third pathway corresponds to the removal of two methyl species to produce the CO and methyl ions. Only one of the product species

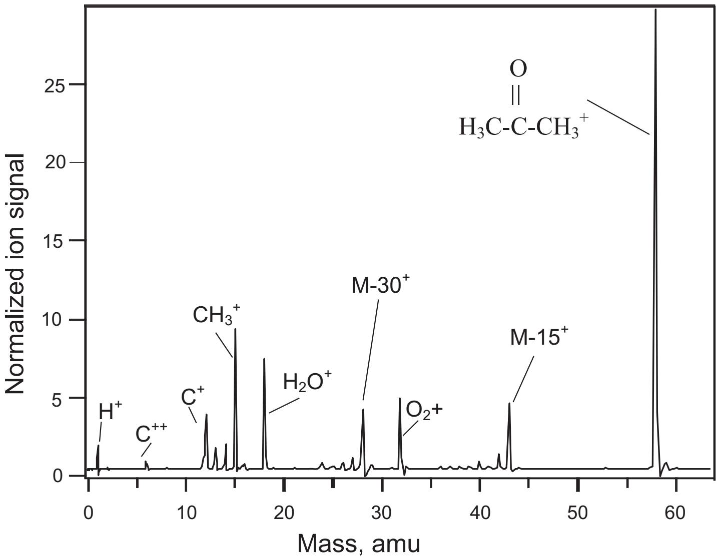

Fig. 6.26. The time-of-flight mass spectrum for acetone after excitation using $5 \times 10^{13}\,\mathrm{Wcm}^{-2}$, 800 nm radiation of duration 60 fs. The prominent peaks in the mass spectrum are marked.

in each channel is shown with a positive charge. Clearly there will be a probability for each of the product species to be ionized that depends on the details of the laser pulse, the fragment's electronic and nuclear structure, and the dissociation pathway.

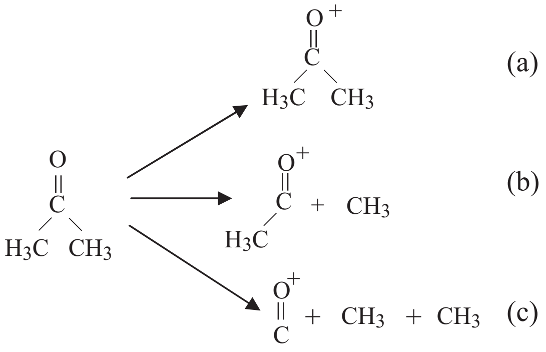

Scheme I

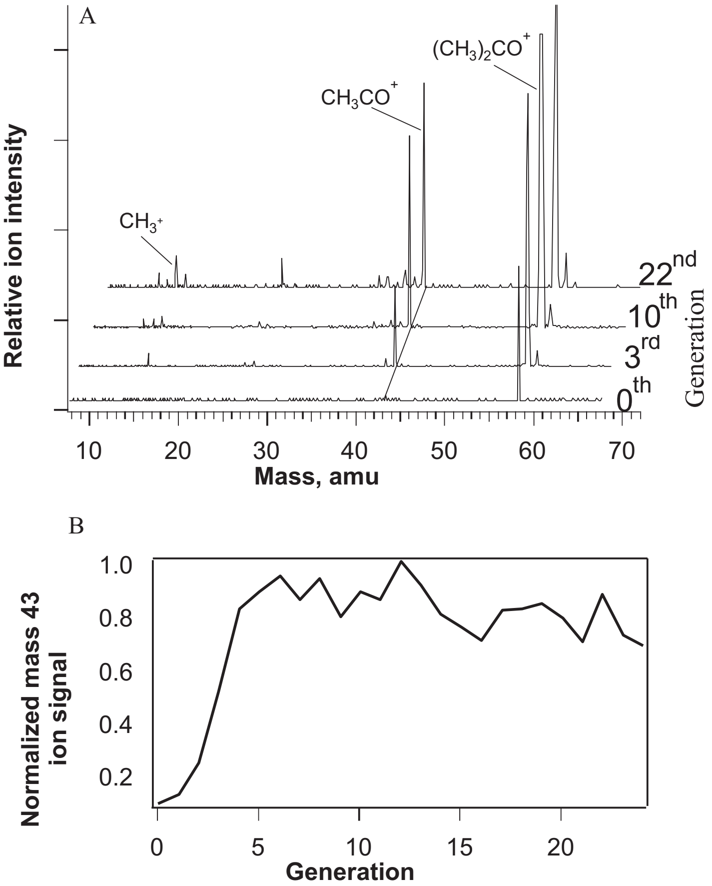

Fig. 6.27. (A) A representative mass spectra of acetone (CH_3-CO-CH_3) for the initial 0th, 3rd, 10th and 22nd generations of the laboratory learning process when maximization of the CH_3CO^+ ion from acetone is specified; (B), The CH_3CO^+ signal as a function of generation of the genetic algorithm. In (B) and the following plots of this type, the average signal for the members of the population at each generation is shown.

One of the simplest illustrations of the OCE closed-loop control algorithm is the case of enhancing the CH_3CO ion signal from acetone. This corresponds to specifying optimization of the second pathway (b) shown in scheme I. Using this criteria, representative mass spectra are shown as a function of generation in Fig. 6.27 when the algorithm has been directed to increase the intensity of the methyl carbonyl ion at $m/e = 43$ amu. The intensity of this ion increases by an order of magnitude by the 5th generation in comparison with the initial randomly generated pulses and is seen to saturate shortly thereafter. The modulation in the signal in subsequent generations is largely due to the algorithm searching new regions of amplitude and phase control field space through the operations of mutation and crossover. The experiment demonstrated two important features of the closed-loop control. The first was that the algorithm was capable of finding suitable solutions in a reasonable amount of laboratory time (10 minutes in this case). The second was that the shaped strong field pulses were able to dramatically alter the relative ion yields and thus the information content in a mass spectrum. We anticipate that the method will have important uses as an analytical tool based on this capability. Finally, the control exerted in this case is of the trivial form, and is due to intensity control as indicated by the masks showing that the optimal pulse was near transform limited and of full intensity. The reference experiments also demonstrated that intense transform limited pulses resulted in a similar fragmentation distribution.

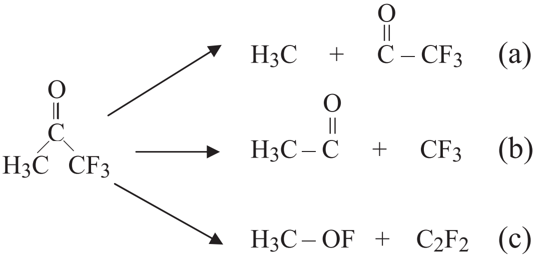

Scheme II

The control over the selective cleavage of various functional groups has been investigated using the molecules trifluoroacetone and acetophenone. Trifluoroacetone was investigated because there are two distinct unimolecular decomposition routes as shown in scheme II (a) and (b). Fig. 6.28 displays the mass spectrum associated with the transform limited, intense laser excitation of trifluoroacetone. The ions of importance in the spectrum include peaks at $m/e = 15$, 28, 43, 69, and 87 corresponding to CH_3, CO, CH_3CO, CF_3 and CF_3CO. These peaks are associated with cleavage of the methyl, fluoryl or both species from the carbonyl group as indicated in scheme II. Interestingly, there is also a feature at $m/e = 50\,\text{amu}$ which can only be assigned to CH_3OF shown in pathway (c). This species must be formed by an intense field rearrangement process and has not been observed in the weak field regime of photochemical reactivity.

The ability of the closed-loop control to cleave a specific bond is demonstrated in Fig. 6.29 where we have specified that the algorithm search for solutions enhancing the signal at $m/e = 69$. This ion corresponds to the CF_3 species. Fig. 6.29 demonstrates that the closed-loop OCE method may be

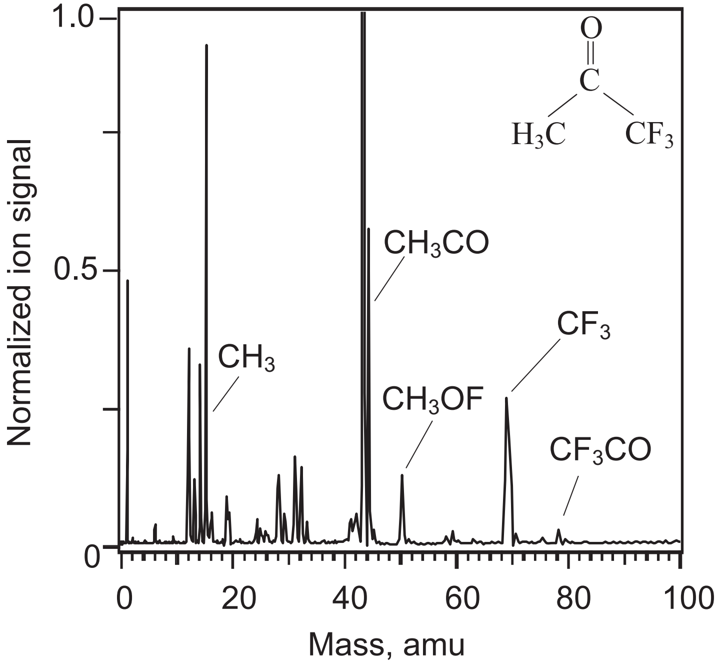

Fig. 6.28. The time-of-flight mass spectrum for trifluoroacetone (CF_3-CO-CH_3) after excitation using 5×10^{13} Wcm^{-2}, 800 nm radiation of duration 60 fs. The prominent peaks in the mass spectrum are marked.

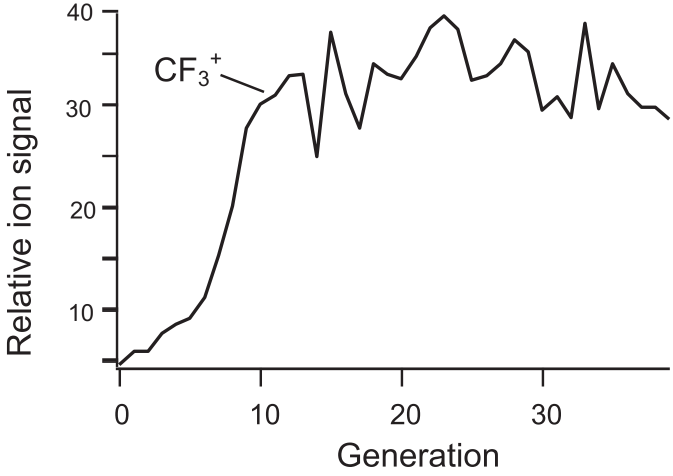

Fig. 6.29. The CF_3^+ signal as a function of generation of the genetic algorithm. In this experiment the cost functional was designed to simply optimize this signal.

used to enhance the desired ion signal by a factor of approximately thirty in comparison with the initial random pulses. While this experiment was successful in enhancing the desired ion yield, it does not necessarily demonstrate control. Control is achieved when one channel is enhanced at the expense of another.

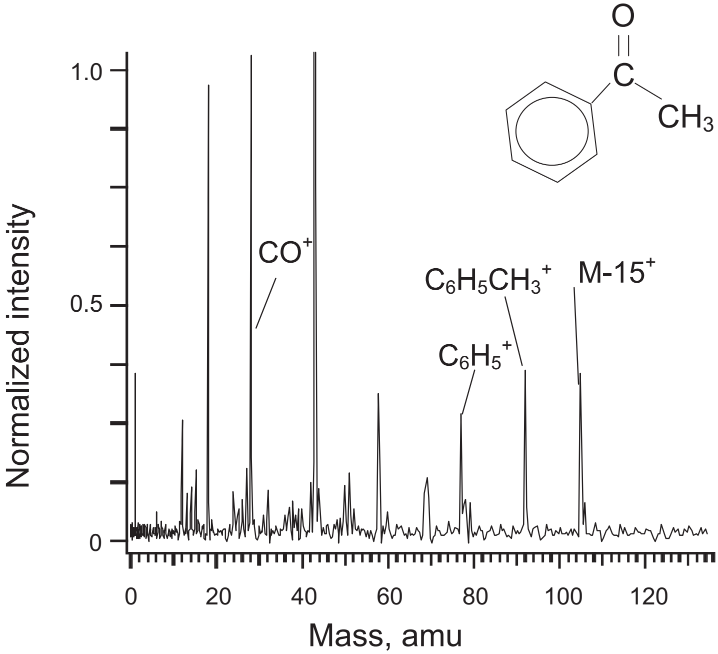

Fig. 6.30. The time-of-flight mass spectrum for acetophenone (C_6H_5-CO-CH_3) after excitation using 5×10^{13} Wcm^{-2}, 800 nm radiation of duration 60 fs. The prominent peaks in the mass spectrum are marked.

To demonstrate control over selective cleavage of specified bonds in a molecule we consider acetophenone, a system that has a carbonyl species bound to methyl and phenyl functional groups. The transform limited mass spectrum for acetophenone is shown in Fig. 6.30. There are numerous peaks detected in the spectrum revealing that there are a multitude of decomposition paths available after excitation. The ions observed at 15 and 105 amu correspond to the species obtained after cleavage of the methyl group. The pair of ions at 77 and 43 amu correspond to cleavage of the phenyl group. The dissociation and rearrangement reactions investigated for this molecule are shown in scheme III. Scheme III(c) implies the rearrangement of acetophenone to produce toluene and CO and this is signified in the mass spectrum by peaks at 92 and 28 amu respectively. To determine whether a path can be

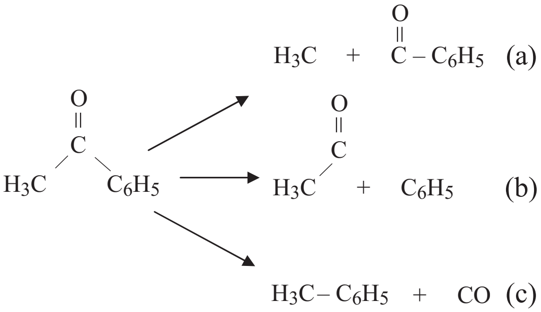

Scheme III

selectively enhanced we specified enhancement of the ion ratio for the species C_6H_5CO/C_6H_5. This denotes selective cleavage of the methyl group at the expense of the phenyl group. Note that we do not stipulate how the ratio should be increased, i.e. increase C_6H_5CO or decrease C_6H_5. Picking a particular path could be done with another cost functional. The ratio as a function of generation is shown in Fig. 6.31. The ratio increases by approximately a factor of 2 after 20 generations. Other ions could have been chosen to control the cleavage reaction, the two chosen happen to be experimentally convenient. Thermodynamically, the goal of enhancing methyl dissociation is the favored cleavage reaction because the bond strength of the methyl group is 15 kcal less than that of the phenyl group [96]. The ratio of phenyl ion to phenyl carbonyl can also be enhanced as shown in Fig. 6.32. The learning curve for this experiment reveals that the phenyl carbonyl ion remains relatively constant while the phenyl ion intensity increases. This is interesting because the energy required to cleave the phenyl-CO bond is 100 kcal while the methyl-CO bond requires 85 kcal. Thus the ratio of these ions can be controlled over a dynamic range of approximately five in the previously reported experiment [85] and a dynamic range of up to 8 has been recently observed.

The goal of laser control of chemical reactivity transcends the simple unimolecular dissociation reactions observed to date [85–87, 97, 98] Observation of the toluene ion in the strong-field acetophenone mass spectrum suggests that control of molecular dissociative rearrangement may be possible. To test this hypothesis we specified the goal of maximizing the toluene yield from acetophenone, as shown in scheme IV. For toluene to be produced from acetophenone, the loss of CO from the parent molecule must be accompanied by formation of a bond between the phenyl and methyl substituents. The closed-loop control procedure produced an increase in the ion yield at 92 amu of a factor of 4 as a function of generation as shown in Fig. 6.33. As a further test, we specified maximization of the ratio of toluene to phenyl ion and observed a similar learning curve to that in Fig. 6.32; with an enhancement in the toluene to phenyl ratio of a factor of 3. Again, the final tailored

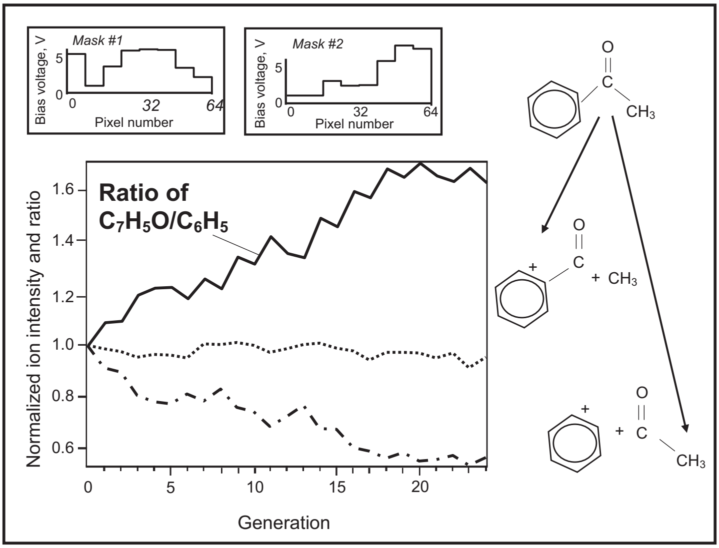

Fig. 6.31. The relative ion yield for phenylcarbonyl (dotted) and phenyl (dashed) and the $C_6H_5CO^+/C_6H_5^+$ ratio (solid) as a function of generation when maximization of this ratio is the specified goal in the closed-loop experiment. The optimal masks resulting from the closed loop process are shown in the inset.

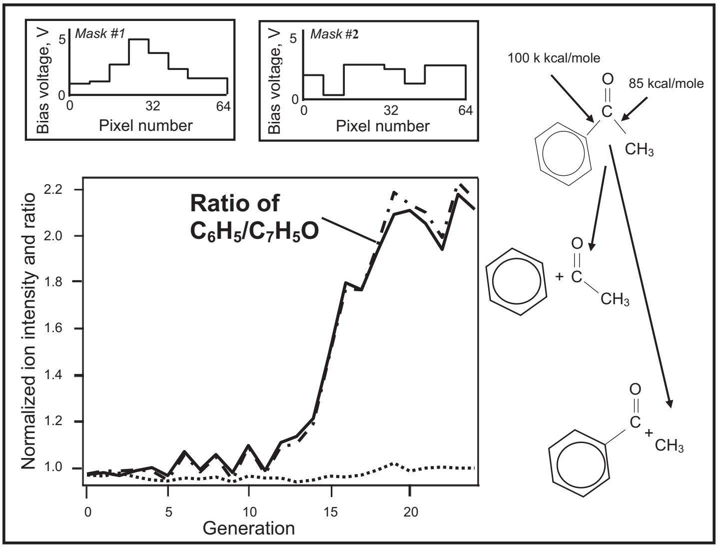

Fig. 6.32. The relative ion yield for phenylcarbonyl (dotted) and phenyl (dashed) and the $C_6H_5^+/C_6H_5CO^+$ ratio (solid) as a function of generation when maximization of this ratio is specified. . The optimal masks resulting from the closed loop process are shown in the inset.

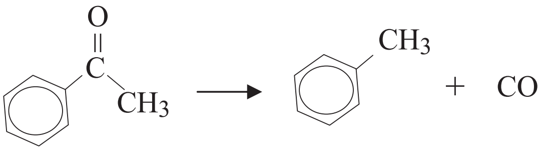

Scheme IV

pulse does not resemble the transform-limited pulse. In order to confirm the identity of the toluene product, measurements on the deuterated acetophenone molecule $C_6H_5COCD_3$ were carried out and the $C_6H_5CD_3^+$ ion was the observed product in an experiment analogous to Fig. 6.33. The observation of optically-driven dissociative rearrangement represents a new capability for strong field chemistry. In fact conventional electron-impact mass spectrometric analysis of acetophenone is incapable of creating toluene in the cracking pattern. In strong-field excitation, the molecular electronic dynamics during the pulse is known to be extreme, and substantial disturbance of the molecular eigenstates can produce photochemical products, such as novel organic radicals, that are not evident in the weak-field excitation regime. Operating in the strong field domain opens up the possibility of selectively attaining many new classes of photochemical reaction products.

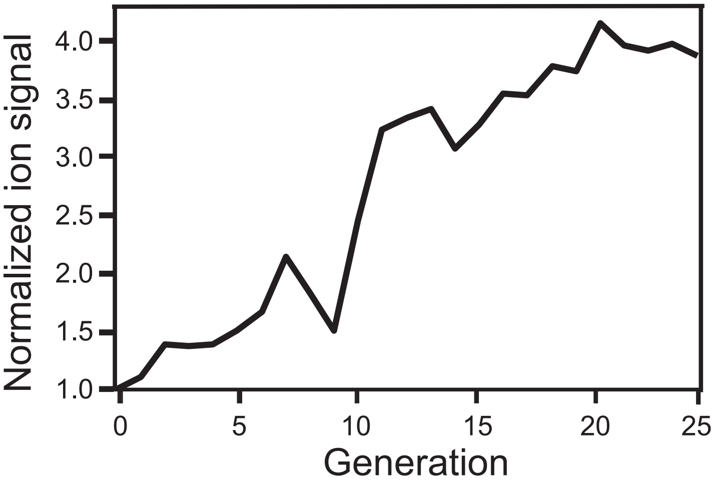

Fig. 6.33. The average signal for toluene, 92 amu, as a function of generation when maximization of the ion signal for this reaction product was specified for optimization. Corresponding electron-impact-ionization mass spectrometry revealed no evidence for toluene in the sample.

Extensive manipulation of mass spectra is possible when shaped, strong field laser pulses interact with molecules under closed-loop control. The control pulses occur with intensity of $\approx 10^{13}\,\mathrm{Wcm}^{-2}$ where the radiation significantly disturbs the field-free eigenstates of the molecule. Even in this highly nonlinear regime, the learning algorithm can identify pulse shapes that selectively cleave and rearrange organic functionality in polyatomic molecules. These collective results suggest that closed-loop strong field laser control may have broad applicability in manipulating molecular reactivity. The relative ease in proceeding from one parent molecule to another should facilitate the rapid exploration of this capability [85].

The limit on the range in control in the examples shown here may be due to a number of factors. The first is that we have employed a limited search space by ganging series of 8 collective pixels in each of the two masks to produce a total of 16 variable elements. We have observed that relaxing this restriction leads to a much longer convergence time, and while a better result is expected, we have not observed such to date. However, other researchers have employed schemes using all pixels, as well as schemes to constrain the amplitude and phase search space [99, 100]. Furthermore, the mass spectrometer was limited to eight averages for these experiments so that convergence can occur on a reasonable time scale. Obviously longer averaging will require longer experiment times. This parameter is under investigation at the present time. Another reason for limited dynamic range is the requirement that the same pulse used to alter the nuclear dynamics also must produce ionization. Each of these processes requires a different pulse timescale. In the case of ionization, the shortest pulse possible, $\approx$ tens of fs, is best for high ionization rates with little dissociation. For the control of the nuclear wave packet it is expected that a pulse with duration on the time scale of nuclear motion, $\sim$ ps, should be optimal. Thus separation of these two processes should lead to a higher dynamic range.

In summary, recent progress in the understanding of fundamental quantum control concepts and in closed-loop laboratory techniques opens the way for coherent laser control of a variety of physical and chemical phenomena. Ultrafast laser pulses, with shapes designed by learning algorithms, already have been used for laboratory control of many quantum processes, including unimolecular reactions in the gas and liquid phases, formation of atomic wave packets, second harmonic generation in nonlinear crystals, and high harmonic generation in atomic gases. One may expect a further increase in the breadth of controlled quantum phenomena, as success in one area should motivate developments in others. The various applications of coherent laser control, no matter how diverse, all rely on the same principal mechanism: the quantum dynamics of a system is directed by the tailored interference of wave amplitudes, induced by means of ultrafast laser pulses of appropriate shape. An important question is whether applications exist for which coherent laser control of molecular reactions offers special advantages (e.g., new products or better performance) over working in the traditional fully incoherent kinetic regime. Finding these applications will be of vital importance for the future progress of coherent control in chemistry and physics.

In addition to the practical utilization of laser control, the ultimate implications for controlling quantum processes may reside in the fundamental information extracted from the observations about the interactions of atoms. The following is intuitively clear, the more complete our knowledge of a quantum system, the better our ability to design and understand successful controls. But, is it possible to exchange the tools and the goals in this logical relationship, and use control as a means for revealing more information on properties of microscopic systems? A challenging objective is to use observations of the controlled molecular dynamics to extract information on the underlying inter-atomic forces. Attaining precise knowledge of inter-atomic forces [101] has been a long-standing objective in the chemical sciences, and the extraction of this information from observed coherent dynamics requires finding the appropriate data inversion algorithms.

Traditionally, the data from various forms of continuous wave spectroscopy have been used in attempts to extract intramolecular potential information. Although such spectroscopic data are relatively easy to obtain, serious algorithmic problems have limited their inversion to primarily diatomic molecules or certain special cases of polyatomics. Analyses based on traditional spectroscopic techniques suffer from a number of serious difficulties, including the need to assign the spectral lines and to deal with inversion instabilities. An alternative approach to the inversion problem is to use an excited molecular wave packet that scouts out portions of the molecular potential surfaces. The sensitive information about the intramolecular potentials and dipoles may be read out in the time domain, either by probing the wave packet dynamics with ultrashort laser pulses or via measurements of the emitted fluorescence. A difficulty common to virtually all inverse problems is their ill-posedness (i.e., the instability of the solution against small changes of the data) which arises because the data used for the inversion are inevitably incomplete. Recent studies suggest that experiments in the time domain may provide the proper data to stabilize the inversion process [102, 103]. In this process, the excitation of the molecular wave packet and its motion on a potential energy surface may be guided by ultrafast control laser fields. Control over the wave packet dynamics in this context can be used to maximize the information on the molecular interactions obtained from the measurements. The original suggestion [104] for using closed-loop techniques in quantum systems was for the purposes of gaining physical information about the system's Hamiltonian. Now that closed-loop OCE is proving to be a practical laboratory procedure, the time seems right to consider refocusing the algorithms and laboratory tools to reveal information on fundamental physical interactions.

6.4 Ionization and fragmentation dynamics in fullerenes

T. Laarmann, C. P. Schulz, and I. V. Hertel

Fullerenes are a special form of carbon clusters, which have been discovered by Curl, Kroto, and Smalley in the mid 80th of the last century [105]. Their discovery has opened a new rapidly growing interdisciplinary research field (see e.g. [106] and references therein). Many of the interesting properties of C_{60} have their origin in its special geometric structure, a truncated icosahedron belonging to the I_h symmetry point group. This unique, football like structure with 12 pentagons and 20 hexagons makes C_{60} the most stable one of the fullerene family. Experimental studies got a strong boost after a method to produce C_{60} in macroscopic quantities was at hand [107]. Ever since, C_{60} became a model for a large finite molecular system with many electronic and nuclear degrees of freedom. Especially, structural and dynamical studies in the gas phase offer a direct way to focus on the properties of isolated C_{60} molecules free from environmental effects. A wide range of processes has been studied leading to a detailed understanding of the mechanism involved in the energy deposition, redistribution, ionization, fragmentation and finally cooling of C_{60}. Just a few early and some recent examples are mentioned out of a wealth of experimental and theoretical studies ranging from thermal heating [108], single-photon [109–111] or multiphoton absorption [112], electron impact [113], collisions with neutral particles [114], atomic ions, including highly charged ions [115–120] as well as molecular ions [121, 122], cluster ions [123] to surface collisions [124–126]. All of these studies have shown that C_{60} is very resilient and can accommodate a substantial amount of energy before it disintegrates. This is mainly due to its highly symmetric structure with 174 nuclear degrees of freedom and 240 valence electrons comprising 60 essentially equivalent delocalized π- and 180 structure defining, localized σ-electrons. The investigation of photon-induced energetics and dynamics have revealed that C_{60} shows atomic properties such as ATI as well as bulk properties such as thermionic electron emission (delayed ionization) [127]. In this sense, photo physical studies of fullerenes cover the whole range from atomic over molecular to solid state physics. The broad band width of responses of C_{60} to strong laser fields and their dependence on the intensity and pulse duration will be discussed in this section.

As has been shown in Sect. 6.3 the photophysics of large finite systems is already at laser intensities below $10^{15}\,\mathrm{Wcm}^{-2}$ dominated by the nonadiabatic multielectron dynamics (NMED), which leads to size and intensity dependent nuclear dynamics and also opens the possibility to control molecular reactions in strong tailored laser fields. These studies have been extended to the C_{60} fullerene and some of the results will be presented in this section. Section 6.4.1 will focus on the ionization process, charge states and fragmentation as observed by mass spectroscopy. Also in this section ATI will be discussed, which has been observed experimentally in photoelectron spectra at different laser intensities. These results will be compared to recent theoretical calculations leading to a critical discussion of the primary excitation mechanism in an intense laser pulse. The single active electron (SAE) picture which is generally used to describe atoms interacting with intense laser light is no longer adequate when describing a system with many almost equivalent electrons. It turns out that many electrons may be excited during the laser pulse. The description of this process has similarities to photo induced processes in the band structure of semiconductors. This will be illustrated in the Sect. 6.4.2 by three characteristic examples: the nonresonant excitation of Rydberg states in C_{60}, the fast fragmentation processes of C_{60} beyond the well established statistical fragmentation processes known from experiments with ns lasers, and the excitation of C_{60} on a time scale below electron-electron and electron-phonon coupling. At the end of this section, experiments to control the energy redistribution in C_{60} using self-learning algorithms with temporally shaped laser pulses will be presented.

6.4.1 Ionization and fragmentation of C_{60} revisited

One of the surprising "early" observations was the delayed ionization of neutral C_{60} on a μs time scale upon irradiation with ns laser pulses [128]. This has been explained by statistical, thermionic electron emission from vibrationally excited molecules. The strong electron-phonon coupling leads to energy exchange between the nuclear and electronic system. Due to the low ionization potential of C_{60} (7.58 eV) compared to the barrier for C_2 loss (> 10 eV), electron emission is the main channel for cooling [129, 130]. Recently, it was found that the ionization behavior sensitively depends on the excitation time scale [127]. The spectacular difference observed in the mass spectra when changing the pulse duration $\Delta\tau$ from 25 fs to 5 ps is illustrated in Fig. 6.34. These mass spectra were obtained for nearly equal laser pulse energies (fluences) of about 20 $\mathrm{Jcm^{-2}}$, the corresponding intensities being $1\times10^{15}\,\mathrm{Wcm^{-2}}$ and $3.2\times10^{12}\,\mathrm{Wcm^{-2}}$, respectively. A strong contribution of multiply-charged C_{60}^{q+} ions together with their large fragments (C_2 evaporative cooling) is very clearly seen in the 25 fs spectrum. However, extremely little fragmentation is detected for singly charged C_{60}^{+} – as illustrated by the insert – and only a few small fragments if any. In contrast, only singly charged ions and massive fragmentation are observed with 5 ps pulses. The large fragment ions in both case are highly vibrationally excited up to an effective temperature of 4000 K and undergo metastable fragmentation μs-ms after the initial energy deposition has occurred [131]. The corresponding mass peaks are marked with asterisks. Fig. 6.34 also shows the typical delayed ionization tail in the 5 ps mass spectrum on the C_{60}^{+} mass peak which is not present for 25 fs.

On first sight, the large finite molecular system behaves as one might intuitively expect: For short pulses of 25 fs length, one (active) electron is ionized by the absorption of many photons and carries most of the energy. In contrast, energy can be transferred efficiently into vibrational modes during a

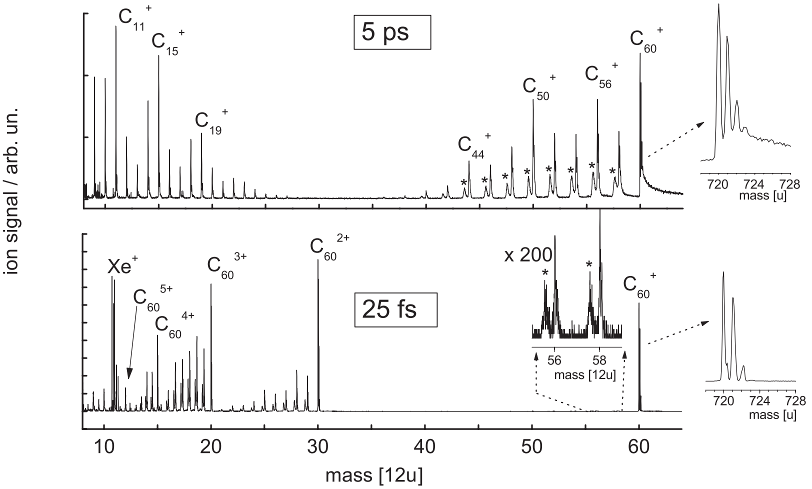

Fig. 6.34. Typical mass spectra taken from [26] obtained from C_{60} by ionizing with Ti:Sa laser pulses of 5 ps (top) and 25 fs duration (bottom) at equal laser fluence. For details, see the text.

laser pulse of 5 ps, since electron-phonon coupling is on the order of 200-300 fs [129]. However, important details remain unexplained in this intuitive picture: Can the different magnitudes of the ion signals be explained quantitatively? Why are multiply charged fragments so dramatically more abundant than singly charged ones – a prominent phenomenon observed for all pulse durations below a few 100 fs and a wide range of intensities? Several mechanisms might be held responsible but one may be related to another important question: How many electrons are actually excited when the electronic ground state is coupled to the continuum by means of the intense, ultrashort laser pulse? This will determine whether the electronic system of the remaining C_{60}^{+} ion core is hot or cold after the first electron has been ejected in a strong fs laser field. If the molecular ion is mainly in its electronic ground state then a theoretical description of the ultrafast perturbation using a single active electron model for the ionization process might be a valid approximation.

Photoelectron spectra can give a complementary and more detailed view of laser induced electron and nuclear dynamics in strong fields compared to mass spectroscopy. Fig. 6.35 shows photoelectron spectra recorded with laser pulses of different duration. Below ~500 fs the excitation energy remains mainly in the electronic system and ionization is due to statistical electron emission after equilibrium among the electronic degrees of freedom [129]. Thermalization within the electron bath due to electron-electron scattering occurs on a time-scale below ca. 70 fs. The photoelectron spectra recorded with very short pulses of $\Delta\tau < 70$ fs at a few 10^{13} Wcm^{-2} clearly show an atom-like behavior

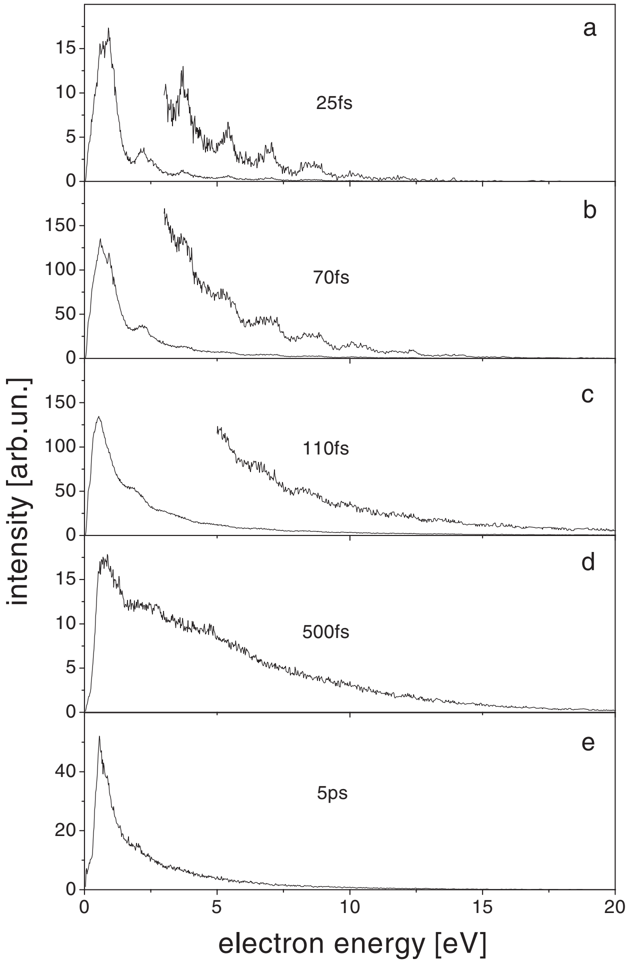

Fig. 6.35. Photoelectron spectra from C_{60} as a function of pulse duration (a)-(d) $8 \times 10^{13}\,\mathrm{Wcm}^{-2}$, and (e) $5 \times 10^{12}\,\mathrm{Wcm}^{-2}$, taken from [127].

of C_{60} with the characteristic ATI structure [132]. This is a fingerprint for direct multi photon ionization in which one active electron absorbs more laser photons than necessary to overcome the ionization potential. Consequently, a kinetic energy distribution of photoelectrons is observed, which exhibits a series of equally spaced maxima separated by the photon energy $h\nu$, as well known from atomic systems [2]. From this point of view, the SAE description of photoinduced processes in the limit of ultrashort laser pulses is appropriate. However, it should be recalled that even ATI in C_{60}, a genuine SAE effect, exhibits multielectron signatures according to recent time-dependent density functional theory (TDDFT) calculations by Bauer et al. [26, 133]. The starting point of these calculations is a jellium-like potential, which is then used to derive Kohn-Sham orbitals for all relevant π and σ electrons.

With this approach it is possible to distinguish between ionization, single particle transition, and plasmon excitation, and also to account for higher order processes beyond single particle-hole excitations. One nice advantage of theoretical simulations is that one can easily switch certain interactions on and off. Doing so, one can either propagate all Kohn-Sham orbitals in time (many active electron, MAE picture), or "freeze" all orbitals except the outermost one, suppressing all MAE effects and following the SAE dynamics exclusively. It turns out that in the SAE model the degree of C_{60} ionization is higher because energy cannot be transferred to the other electrons and the ATI lines are much narrower due to the lack of electron-electron interaction. It seems that for a complete description of the photoinduced dynamics in C_{60} the full MAE picture is needed.

6.4.2 Multielectron excitation, energy dissipation and coupling to the nuclear backbone

As already discussed in the previous Sect. 6.4.1, one of the interesting but also difficult to analyze facets of intense laser field interaction with C_{60} fullerenes is the large variety of potential responses ranging form atom-like to solid-like behavior such as ATI on one side and thermionic electron emission on the other side depending on the laser pulse duration. This raises the question when the SAE dynamics dominating the strong field response of atoms [22, 45, 60] passes over to the multielectron response in large finite systems [134–137]?

While such information cannot be extracted from presently available experimental data, one can try to identify specific aspects of the response of C_{60} to strong fields as being attributable to the one or the other of these "two faces". One example is the observation of Rydberg states [138]: while the population mechanism of these states is clearly driven by multielectron excitation, the binding energies of the Rydberg states themselves can be derived in a very simple SAE approach describing the almost atom-like single Rydberg electron in its orbital far away from the C_{60} ion core [139, 140]. Consequently, this is an ideal observable to address these questions, which will be discussed in the following Sect. 6.4.2.1.

It has been shown in Sect. 6.4.1, that the efficient excitation of the electronic system and the subsequent heating of the nuclear backbone lead to extensive fragmentation depending on the laser parameters. Many aspects of this process such as the high excitation threshold for fragmentation (kinetic shift) and the bimodal fragment distribution at high excitation energies can be explained very well in terms of statistical theory, essentially on the basis of knowing the energetics of the system as described, e.g., in [131]. However, recent experiments give also evidence to direct, nonstatistical processes driven by bond-softening and/or repulsive state crossings induced by the strong laser field [141]. This leads back to a more molecular description of dissociation, where the system "surfs" on potential energy surfaces rather than being exclusively controlled by statistics. This coexistence will be discussed in the Sect. 6.4.2.2 underlying the complex energetic and dynamics of fullerenes.

Interesting parallels can be found when comparing collision studies on C_{60} with fs laser excitations when looking at the ultrafast electronic and nuclear response (see e.g., [142, 143]). Ultrashort pulses as well as fast collisions deposit energy predominantly into the electronic system. Naively, one could imagine that the shorter the ultrafast perturbation of the C_{60} molecule the easier the absorption process can be understood. Of course, this is partly true since energy redistribution processes such as (i) electron-electron scattering and (ii) electron-phonon coupling increase the complexity of the energy absorption process if the laser pulse is still "on". The characteristic coupling time constants estimated experimentally are for process (i) < 70 fs and for process (ii) 200-300 fs [127, 129]. On the other hand, rather complex MAE effects might come into play in the limit of ultrashort (sub-10 fs) pulses. This issue is addressed in detail in the last Sect. 6.4.2.3, where time-of-flight mass spectroscopic data will be discussed, which were recorded upon irradiation of C_{60} with intense laser pulses down to 9 fs pulse duration.

6.4.2.1 Population of C_{60} Rydberg states beyond the single active electron picture

Sharp peaks were discovered in photoemission studies of C_{60} on top of the ATI series and the thermal electron contribution after Ti:Sa laser excitation at a few $10^{12}\,\mathrm{Wcm}^{-2}$ as shown in Fig. 6.36. By solving the Schrödinger equation for a single active electron in a jellium-like potential [144], this structure could be clearly assigned to the population of several Rydberg series with binding energies E_b between 0.5 and 1.5 eV [138]. By studying the effect of different laser parameters such as excitation wavelength, intensity, polarization, and positive, respectively negative chirp on the excitation dynamics of Rydberg states further insight into the underlying processes was obtained [140]. The results from single pulse spectroscopy can be summarized as follows. The *excitation* of Rydberg states occurs mainly during the first part of the laser pulse while the *ionization* takes place toward the end of the pulse. The spectra recorded for different Fourier-limited pulse durations $\Delta\tau$ and corresponding bandwidths ΔE – albeit broadened in accord with the bandwidth – indicate that the excitation mechanism must be very fast: traces of a Rydberg population can be observed even for pulses as short as 30 fs [140]. The final single photon ionization step in the cascade is supported by studying details of the photoelectron spectra depending on the laser photon energy. The kinetic energy of photoelectrons converges toward the respective photon energy, i.e., the accessible excited state for ionization is limited by the photon energy [140].

The observation of Rydberg peaks seems to be a clear fingerprint of the SAE picture. However, some important aspects warrant further discussion. Most critical is the energy mismatch between the observed excitation energy

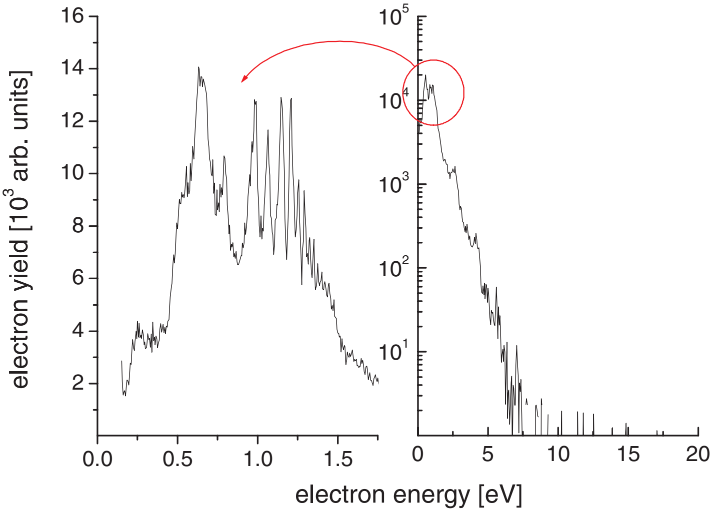

Fig. 6.36. Photoelectron spectra of C_{60} for 800 nm, 1.5 ps laser excitation at $1.1 \times 10^{12}\ \mathrm{Wcm}^{-2}$, in log-lin scale to show the signal over a wide range of electron energies (right) and with linear scales to show the pronounced Rydberg structure on top of the first ATI peak (left). Reproduced from [138]

of the Rydberg states $(E_I - E_b)$ and a multiple of the photon energy: It is simply not possible to be in resonance with all observed Rydberg states simultaneously through the absorption of n photons with a given energy. The Fourier-limited energy bandwidth of the up to 2 ps long laser pulse is much too narrow to allow for the excitation of Rydberg states covering 1-2 eV in energy. Moreover, in this intensity regime the field-induced ponderomotive shift of the energy levels is also too small (< 100 meV) to account for the observed energy mismatch. Thus, key mechanisms such as line broadening and energy sweeping, known from atomic systems in strong laser fields [145], cannot explain the Rydberg excitation process under the present conditions in C_{60} fullerenes. In contrast, a plausible explanation may be to invoke excitation of intermediate (doorway) states during the laser pulse by single or multi photon processes. The concept of doorway electronic states originates from the fact that the initial step in the excitation cascade is rate limiting and can be considered as a bottleneck for energy coupling into the electronic system [80,81]. Such processes have recently received great attention in the literature and a number of theoretical models have been discussed. Two of them are mentioned explicitly, (i) the nonadiabatic multielectron dynamic (NMED) model introduced by Stolow and collaborators [24,25] and (ii) time-dependent adiabatic potential energy crossings suggested by Kono et al. [146,147]. NMED has been used successfully to describe the dissociative ionization dynamics of different aromatic molecules as a function of their characteristic length and the excitation of the π-electron delocalization. The latter has been applied to lighter molecules in comparison with the NMED studies.

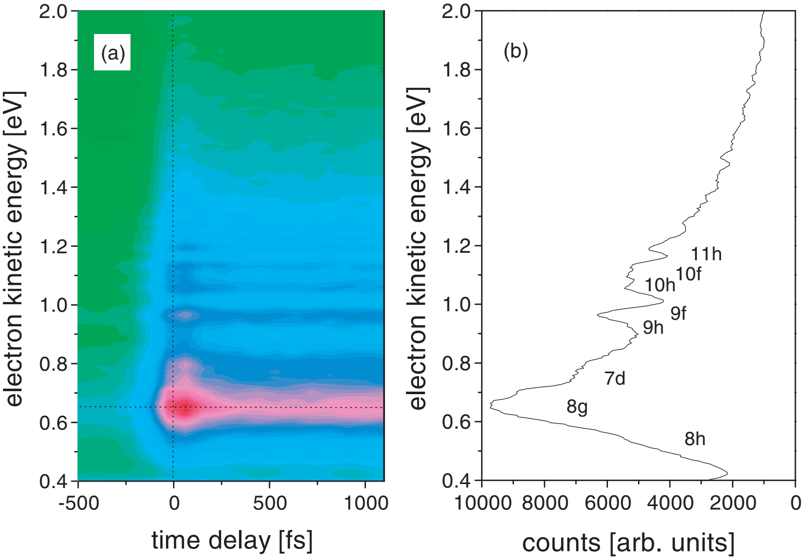

Fig. 6.37. (a) Contour plot of the photoelectron signal as a function of the time-delay between 400 nm pump $1 \times 10^{11}\,\mathrm{Wcm}^{-2}$ and 800 nm probe pulse $2 \times 10^{12}\,\mathrm{Wcm}^{-2}$. (b) Kinetic energy distribution of photoelectrons for zero delay time, which corresponds to a vertical cut in (a) along the dotted line, taken from [140].

It is suggested that the key to understand the population mechanism of the Rydberg series is indeed the MAE/NMED picture which is supported by recent, more detailed studies applying two-color pump-probe spectroscopy [139, 140]. The photoelectron spectra recorded as a function of the time-delay between 400 nm pump ($1 \times 10^{11}\,\mathrm{Wcm}^{-2}$) and 800 nm probe-pulse ($2 \times 10^{12}\,\mathrm{Wcm}^{-2}$) are shown by the contour plot in Fig. 6.37a. A blue 100 fs pump pulse of relatively low intensity, which is resonant to the dipole-allowed HOMO (h_u) → LUMO+1 (t_{1g}) transition, was used to deposit energy efficiently into the electronic system. The dynamics of the energy redistribution within the electronic system and the accompanied coupling to the nuclear motion is then probed by a time-delayed 100 fs red probe pulse. Thus, several steps of the excitation and detection process are separated. A cut through this contour plot for zero time-delay along the vertical dotted line is given in Fig. 6.37b. It corresponds to a photoelectron spectrum which essentially reproduces the Rydberg series obtained in the one color (800 nm) experiments (Fig. 6.36a) – except for a poorer spectral resolution due to the shorter pulses.

At negative time delay when the red pulse leads, almost no photoemission signal from excited Rydberg states is observed. Once pump and probe pulse overlap the photoelectron yield increases dramatically and a maximum population of the Rydberg series is found at a time delay of 50-100 fs. It can be inferred from this observation that the resonant preexcitation of the LUMO+1 (t_{1g}) state by the weak blue laser pulse is essential to populate Rydberg states. At time delays longer than 400 fs the photoelectron spectra remain nearly the same for several picoseconds.

In a classical molecular picture one would typically invoke doubly excited states and internal conversion (IC) to describe such processes. Indeed, similar Rydberg structures have been reported for several organic molecules and the excitation mechanism has been explained there by such "superexcited" states [148, 149]. In the context of the large finite system C_{60} exposed to fs laser radiation the MAE/NMED processes may be considered to be the adequate equivalent to Rydberg state excitation via such superexcited states. This interpretation is confirmed in the calculations by Zhang et al. [135], predicting multielectron excitation of the LUMO+1 level of C_{60} that is accompanied by strong vibrational excitation and massive energy exchange of ~ 1 eV per electron with the $a_g(1)$ breathing mode.

The experimental results point toward an excitation mechanism including four main steps [140]: (i) At the beginning of the laser pulse nonadiabatic multielectron excitation from the HOMO (h_u) leads to a very efficient population of the LUMO+1 (t_{1g}), which is considered to be the doorway state for all subsequent processes. (ii) The rapid thermalization within the electronic system on a time scale below 100 fs and the coupling of the electronic excitation to nuclear motion of the molecule results in the population of a broad energy band of 1-2 eV depending on the photon energy. The energy is stored for at least several ps in the doorway state without discernable relaxation. (iii) The "level broadening" allows the population of Rydberg states via multi photon absorption. (iv) This is followed by single photon ionization from the excited states resulting in a characteristic sequence of photoelectron peaks.

Investigation of cold C_{60} molecular beams with reduced vibrational energy content and hence, reduced phonon density highlight the importance of electron-phonon coupling in the excitation process of Rydberg states. Due to the reduced vibrational coupling, the characteristic signature of populated Rydberg levels in the photoelectron spectra is absent [139]. Time-resolved photoion spectroscopy shows that these mechanisms are also active in multiple ionization and fragmentation of the molecule [140], as will be discussed in the following Sects. 6.4.2.2, 6.4.2.3, and 6.4.3.

6.4.2.2 Ultrafast fragmentation of C_{60} beyond purely statistical, unimolecular decay

The dynamics of the fragmentation in C_{60} following the strong field excitation is far from being fully understood. While it is clear that large fragments arise essentially from evaporative cooling of hot C_{60}^{q+} ions it is not obvious how the substantial amount of internal energy needed for fragmentation is deposited into the system [150]. Absorption bands in the cations have been held responsible [151, 152], excitation of the plasmon resonance [153], or even recollision of the emitted electrons [154]. While neither of these processes explains the general trend to more extensive fragmentation at higher charge states, also observed in fast collisions, shake processes in the ionic system might eventually lead to a more consistent picture [111]. Even less obvious are the pathways to form small carbon cluster ions C_n^+ with odd and even numbers of carbon atoms during longer ps pulses shown in Fig. 6.34. Many different processes and their combination have to be considered, such as asymmetric fission of multiply charged ions [155], complete breakup of highly excited C_n^+, dissociative ionization, postionization of neutral fragments during the laser pulse and photofragmentation of small neutral and ionic clusters C_n, C_n^+ ($n \leq 20$).

In this section first results are reported from an effort to shed light onto this dynamics, focussing mainly on the formation of small C_n^+ [141]. An earlier, pioneering study of Lykke and Wurz [156, 157] may be seen as a precursor of this work: they used ns-laser pulses to preexcite and/or ionize C_{60} and probed the interaction products with a second, postionizing laser, detecting C^+, C_2^+, C_3^+, and C_4^+. Since the fragmentation pattern of larger fullerenes shows only even masses C_{60-2n}^+ one may safely assume that these small ions arise as final products from a series of fragmentation processes, concurrent with the above mentioned studies [158, 159]. No temporal information on the underlying fast dynamics could be derived on the ns time scale. Hence, the basic idea is to use a one color pump-probe scheme with 800 nm laser pulses of 50 fs pulse duration to simulate in a controlled way the effect of broadening the laser pulse which, as shown in Fig. 6.34, generates small fragments. Since the majority of fragmentation channels results in at least one neutral fragment (typically the smaller fragment), the pump-probe postionization method is a useful technique to study directly their formation dynamics. In these experiments a pump pulse at an intensity of $5 \times 10^{13}\,\mathrm{Wcm^{-2}}$ deposits energy into the electronic system by exciting one or more electrons into higher lying states (see Sect. 6.4.2.1). The multielectron dynamics initiated is probed by a weaker probe pulse of $1.8 \times 10^{13}\,\mathrm{Wcm^{-2}}$, which further excites and ionizes by a multi photon process. Fig. 6.38 shows the formation of C^+, C_2^+, C_3^+, and C_4^+.

For negative time delays, the weak pulse leads the strong pulse and a constant signal for each fragment is observed. For positive time delays, when the strong pulse initiates the multielectron dynamics, a dramatic increase in the C^+–C_3^+ ion yields is observed as the separation of the pulses increases, whereas C_4^+ exhibit nearly no dynamic behavior. At time delays > 50 ps the signal remains almost constant up to the longest time scales studied in these experiments (~ 100 ps). It is possible to fit the dynamics using single exponential curves with time constants of 11 ps (C^+), 12 ps (C_2^+) and 18 ps (C_3^+). The

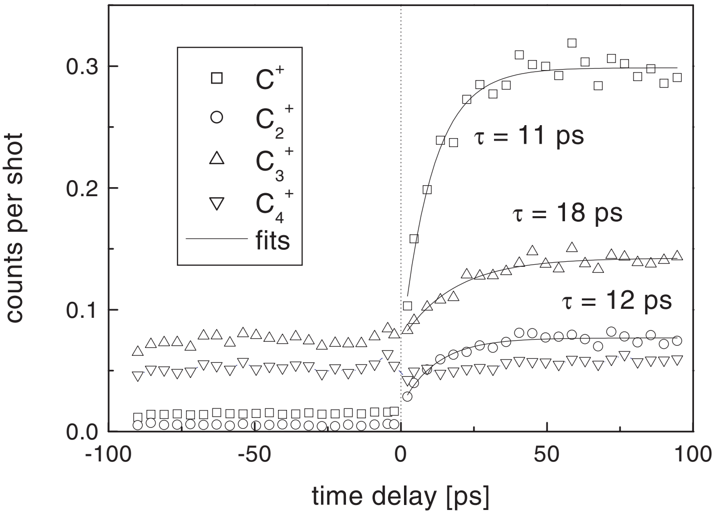

Fig. 6.38. Time-dependent C^+, C_2^+, C_3^+, and C_4^+ ion signals formed by Ti:Sa laser pulses (800 nm, 100 fs) interaction of C_{60} at 5×10^{13} Wcm^{-2} (pump) and ionization at 1.8×10^{12} Wcm^{-2} (probe). For positive delay times, the stronger pulse leads the weaker pulse. From [141]

time constants are found to be almost independent of the weak probe pulse energy, which indicates that the weak probe pulse is not active in the formation process of small neutral fragments [141]. Furthermore, the absence of small fragments in single pulse experiments indicates that the small fragments are initially uncharged.

Clearly, the observed fragmentation times on the order of some 10 ps indicate a non statistical decay: for comparison one estimates from simple RRK considerations [160] that, e.g., a unimolecular C_2 evaporation from C_{60} would require internal energies as high as about 200 eV - while the very low abundance of C_{60-2m}^+ fragments detected shows that only a small part of all parent molecules contains energies above 100 eV.

6.4.2.3 Excitation of C_{60} on a time scale below electron-electron and electron-phonon coupling

The ultrafast response of C_{60} fullerenes to intense, short laser pulses with a duration down to 9 fs has been investigated with pump-probe photoion spectroscopy [153]. The irradiation of a beam of C_{60} with such ultrashort pulses allows one to separate the energy deposition into the electronic system in time clearly from the energy redistribution among the manifold of electronic and nuclear degrees of freedom, because the excitation time lies well below the characteristic time scales for electron-electron and electron-phonon coupling. The goal is to *directly* observe fingerprints of multielectron effects in the initial excitation steps of C_{60} irradiated with ultrashort 9 fs pulses. More specifically, the aim is to find indications for a remaining excited electron cloud after the first electron has been “kicked-out”. In general, the coupling of excited electrons to atomic motion leads to nuclear rearrangement in the ionic or in the neutral molecular system. According to recent theoretical work on C_{60} [135, 161], this results in characteristic oscillations, discussed already in the context of the population mechanism of Rydberg states. Both, multielectron excitation and the characteristic oscillation may be observed with time-resolved mass spectroscopy, since the density of excited electrons and the nuclear geometry are expected to affect the photoionization yield of C_{60} in a time-dependent study. The ultrashort pump pulse with an intensity of $7.9 \times 10^{13}\,\mathrm{Wcm}^{-2}$ solely deposits the energy in the electronic systems during the interaction. The energy redistribution within the electronic and nuclear degrees of freedom is then probed by a delayed, slightly less intense probe pulse ($6.8 \times 10^{13}\,\mathrm{Wcm}^{-2}$).

Fig. 6.39a shows the measured time dependence of the normalized C_{60}^+ ion signal. Particularly, the comparison with the simultaneously measured Xe^+ signal included in the figure is instructive. Xe^+ formation constitutes a genuine direct MPI process with probably only one active electron determining the systems response and, thus, can be taken as an auto-correlation measurement. The C_{60}^+ ion signal is clearly broadened at the bottom of the spectrum. As shown in Fig. 6.39b, the deconvolution of the total ion yield results into two main contributions: direct MPI of C_{60} from the neutral ground state to the continuums state (dark gray-shaded), which essentially follows the Xe auto-correlation plus a significant contribution exhibiting dynamics on a sub-100-fs time scale (light gray-shaded) which is slightly shifted toward positive time delays, when the stronger pump pulse leads the weaker probe pulse. This deviation of the C_{60} ion pump-probe signal from the auto-correlation function can be interpreted as a clear indication of multielectron excitation in a subensemble of C_{60} during the laser interaction. Supported by recent theoretical work, [134, 135, 161] one believes that in addition to the direct MPI process there is a probability to initially excite two or more electrons via the t_{1g} resonant state, which in turn acts as a doorway (bottleneck) to ionization. The observed dynamics is comparable to the characteristic time for thermalization within the electronic system due to inelastic electron-electron scattering ($<$ 70 fs), as previously concluded from single pulse experiments [127, 129]. As intuitively expected the density of the hot electron cloud depends on the laser intensity, and its time evolution on the electron-electron scattering time constant [135]. The excited electron density in the doorway state determines the transition probability into the ionic continuum. Since pump and probe pulse have slightly different intensities (7.9:6.8) the ion distribution due to doorway state excitation is slightly shifted to positive time-delays, as shown in Fig. 6.39b. Based on a rough fit with two response functions for the undelayed, direct SAE/MPI process (proportional to the acf signal) and the MAE/NMED with its memory effect (taken as exponential decay), respectively, an estimate

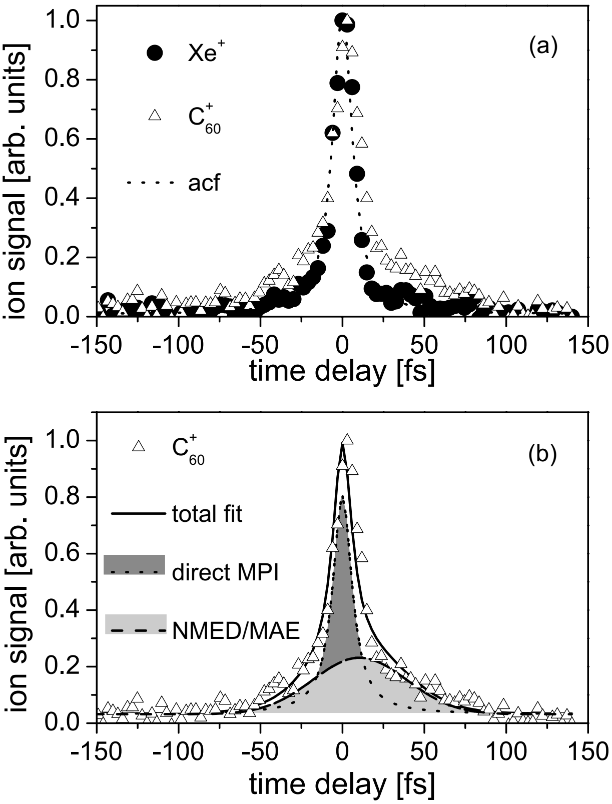

Fig. 6.39. a) C_{60}^+ ion yield (open triangles) as a function of the time-delay between pump ($7.9 \times 10^{13}\,\mathrm{Wcm}^{-2}$) and probe pulse ($6.8 \times 10^{13}\,\mathrm{Wcm}^{-2}$), normalized to the maximum signal. $t = 0$ is defined by the auto-correlation function (acf, dotted line) derived from a fit to the simultaneously measured Xe^+ signal (closed circles). (b) Contributions from direct SAE/MPI (dark gray-shaded) and MAE/NMED (light gray-shaded) refer to our tentative deconvolution of the C_{60}^+ photoion yield, for details see the text. (from [153])

of 65% to 35% for the contribution of SAE and NMED processes to the signal have been obtained.

6.4.3 Control of energy dissipation processes using temporally shaped laser pulses

The previous sections were focused on the *analysis* of photophysical processes in C_{60} by comparing photoelectron or mass spectra taken with different characteristic laser parameters, such as a intensity, pulse duration, photon energy or pump-probe delay. In the following results are presented with the goal to

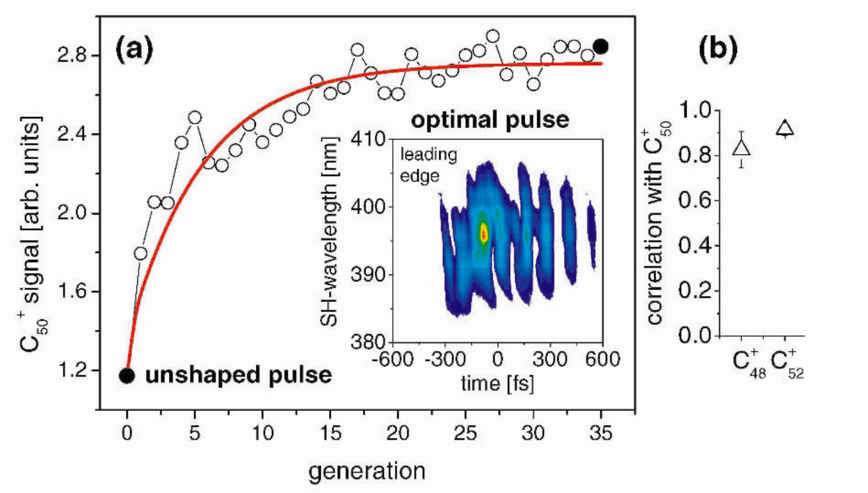

Fig. 6.40. (a) C_{50}^+ signal as a function of generation of the evolutionary algorithm. The inset shows the SH-XFROG trace of the optimal solution. (b) Correlation with neighboring fragment masses C_{48}^+ and C_{52}^+ taking into account 7 independent optimization processes [162].

control the molecular response with suitably tailored fs laser pulses [162]. Details of the self-learning closed-loop adaptive feedback technique can be found in Chapter 2, Sect. 2.4 and also in Sect. 6.3 of the present Chapter. Here, the selective enhancement of C_2 evaporation is reported, a typical energy loss channel upon laser excitation of fullerenes as discussed in previous sections. The learning curve for maximization of the C_{50}^+ fragment ion yield is plotted in Fig. 6.40a. The thus determined optimal pulse shape for this specific target is characterized by means of second-harmonic, cross-correlation frequency-resolved optical gating (SH-XFROG) shown in the inset. As a result, the mass peak increased by a factor of $S \sim 2.0$ compared to the signal recorded with unshaped pulses given as 0th generation. The height of the C_{50}^+ peak was chosen as fitness criterion because its abundance is a measure for the temperature of the nuclear backbone, i.e., indicates efficient energy coupling into nuclear motion. It is well-known that cooling of highly excited C_{60} proceeds mainly via sequential evaporation of C_2 units in a statistical process. This explains why a strong correlation of the C_{50}^+ enhancement with neighboring fragment masses C_{48}^+ and C_{52}^+ is observed when comparing 7 independent optimization runs in Fig. 6.40b. It has to be pointed out that the optimal control scheme applied here is selective for depositing energy into the C_{60} system, and not for selective bond-breaking. The key result is that a sequence of pulses is best suited for most efficient energy coupling into vibrational motion of C_{60}. It gives a direct fingerprint of the laser induced electron and nuclear dynamics with high mode-selectivity as seen in the SH-XFROG trace in Fig. 6.40.

This microscopic view goes beyond the common wisdom where the response of fullerenes to intense laser fields was assumed to be mainly determined by the interaction time scale, i.e., electron-electron and electron-phonon coupling. One may call the observed process "coherent heating".

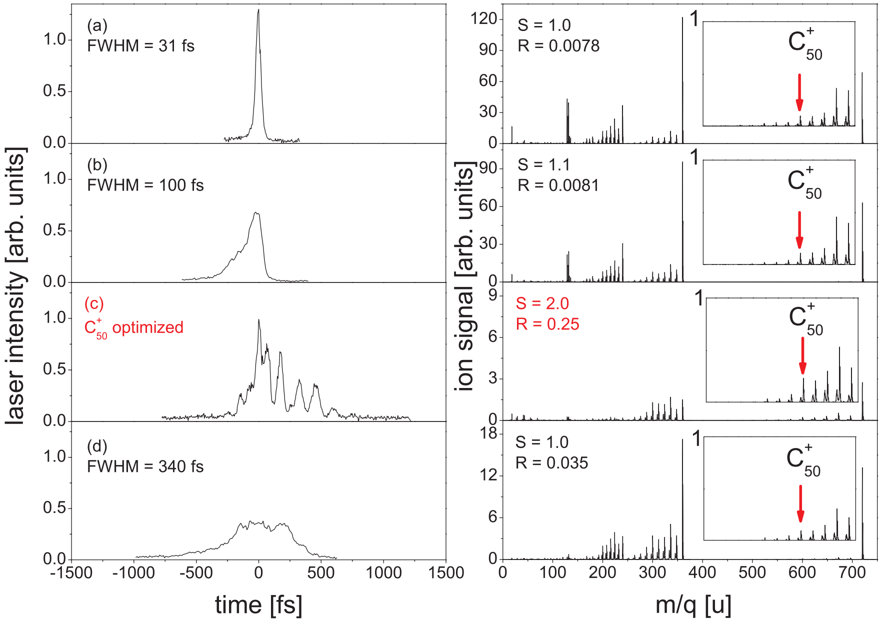

Fig. 6.41. Mass spectra (right panel) recorded with constant pulse energy (260 μJ but different pulse shapes given as projections of the corresponding SH-XFROG-traces (left panel): (a) original pulse (31 fs), (b) stretched pulse to 100 fs, (c) optimal pulse shape, and (d) 340 fs. The insets show the mass range of singly charged, large fragments plotted on the same scale. *S* gives the enhancement of the C_{50}^{+} signal, and *R* denotes the ratio C_{50}^{+}/C_{60}^{+}. (From [162])

Fig. 6.41a-d compares mass spectra recorded for stretched pulses with the optimal control result regarding the formation of C_{50}^{+} fragments in order to proof the relevance of the pulse sequence for most efficient coherent heating. Pulse broadening was achieved by applying parabolic spectral phase functions that keep the energy constant at 260 μJ. The temporal shapes are given as projections of the corresponding SH-XFROG traces on the left. From the mass spectra shown on the right, where the singly charged ion signals are all plotted on the same scale (insets), it is obvious that the pulse sequence of the optimal control field (c) is the key for enhanced energy coupling followed by statistical evaporation of C_2 units and not simply the increased overall pulse width. Both, stretched pulses of (b) 100 fs and (d) 340 fs duration result in significantly less singly charged fragments.

The combination of optimal control with comprehensive studies using 2-color pump-probe spectroscopy (not shown here) allows us to pinpoint the mechanism of optimal heating nuclear motion in C_{60} fullerenes, namely (multi)electron excitation via the t_{1g} doorway state followed by efficient coupling to the $a_g(1)$ breathing mode of the nuclear backbone.

This section has touched some aspects of the present state-of-the-art of research on the ultrafast laser interaction with C_{60} as a model for large finite systems with many active electrons and vibrational degrees of freedom. The comparison of experimental results using time-resolved photoelectron and mass spectroscopy with recent theoretical work gives a strong indication that nonadiabatic multielectron dynamics (NMED) plays a key role for the understanding of the molecular response to short-pulse laser radiation. Nevertheless, one is still far from fully understanding the intricacies of intense field interaction with such a complex system. Rigorous theoretical efforts are needed to quantitatively explain the key aspects of the experimental observations presented here and those to emerge in the near future: the nature of the ionization and fragmentation mechanisms which produce predominantly multiply charged fragments, the excitation dynamics for the population of Rydberg states, the long lifetimes observed in the doorway state and the ultrafast fragmentation mechanism. On the other hand, further experimental work is needed – preferentially with even shorter pulses (and better tunability of the fs light sources) – to perform sophisticated and direct multicolor pump-probe experiments. Experimental detection schemes need to become more sophisticated, e.g., the ion imaging technique promises a new view into the dynamics discussed here. This will, in connection with coincidence techniques, allow to follow fragmentation cascades directly and to separate prompt ionization from postionization processes. Furthermore, new laser schemes for intense radiation at shorter wavelength such as high-harmonic generation, table-top plasma sources, and Free-Electron Lasers, are expected to open completely new horizons for strong field laser-matter interaction.

6.5 Time-dependent electron localization function: A tool to visualize and analyze ultrafast processes

A. Castro, T. Burnus, M. A. L. Marques, and E. K. U. Gross

The classical picture of chemical bonding in terms of electron pairs that are shared by atoms in order to form molecules was nicely systematized by G. N. Lewis, in his seminal work entitled “The Atom and the Molecule” [163], dated 1916. Lewis noticed the overwhelming evidence pointing to the “pairing” of the electrons, as well as the preference to close “shells” of eight electrons. Soon afterwards, the pairing of electrons was explained in terms of the Pauli exclusion principle together with the electronic intrinsic one-half spin, whereas the number eight in fact emanates from both Pauli's principle and the spherical symmetry of atoms in a three dimensional world. Lewis, however, was some years too early, and designed "the theory of the cubical atom", with the electrons occupying the vertex of a cube (although he acknowledged the picture to be more methodological than fact-founded), and pointed to a breakdown of Coulomb law at short distances in order to explain the electron pairs. Despite these exotic suggestions, the usefulness of Lewis model has persisted even until today's textbooks.

The reason is that electrons do indeed "localize" in pairs when forming molecules, and a big amount of the basic machinery of Chemistry is rather well explained with Lewis arguments. In fact, more generally, Chemistry is intuitively understood in terms of "localized" groups of electrons, either pairs of electrons shared between atoms ("bonds"), nonbonding pairs of electrons ("lone pairs"), and also larger groups – double, triple bonds –, atomic inner shells, π electronic systems, etc.

With the advent, in the past years, of sources of coherent light featuring high intensity and ultrafast pulses (in the femtosecond [164], or already below the femtosecond limit [165]), it has become possible to *time resolve* the intermediate steps of chemical reactions – paving the way to the possibility of analyzing and controlling chemical reactions. These technical advances stress the need of understanding how the electrons rearrange, forming and destroying bonds, in the midst of a laser pulse, and during the possible ionic recombination. The chemical concepts of bonds, lone pairs, etc. have to be fathomed also for time-dependent phenomena.

Unfortunately, the transformation of these concepts into a mathematically rigorous scheme for classifying the elements of the chemical bonding turns out to be astonishingly difficult. The canonical single-particle orbitals that stem from Hartree-Fock (HF) calculations are not very helpful, since they, typically, have sizable contributions from many regions in space. Moreover, they are only one possible choice, since unitary transformations within the subspace of solutions yield equally legitimate orbitals. There are several ways in which one can perform these unitary transformations in order to obtain localized functions [166], but these methods are also not unique, and may result in qualitatively different information.

In any case, HF is but one of the possible schemes to obtain an approximate solution to the many-body problem. A definition based on the HF solution would always be affected by the HF error – absence of correlation effects. It is desirable to have a scheme that does not rely on a particular method. Kohn-Sham (KS) [167] density functional theory (DFT) [168–170] also provides single-particle orbitals (in this case unique, except for degenerate groundstates), but they are usually also very delocalized in real-space. The electronic density is an observable, and thus independent of the method. Moreover, it contains all the information of the system by virtue of Hohenberg-Kohn theorem [171]. Unfortunately, the density itself is not suitable to visualize chemical bonding: It does not peak in the position of the bonds, it does not show the shell structure of atoms, and lone pairs, also, are poorly represented.

The key to comprehending electron localization is, in fact, Pauli's exclusion principle, and, relatedly, the Fermi hole: Bader and collaborators [172] demonstrated how all manifestations of the spatial localization of an electron of a given spin are the result of corresponding localizations of its Fermi hole. An appropriate localization function should be closely related to this Fermi hole or to an analysis of Pauli's principle. This is indeed the case for the function to which we devote this section: Becke and Edgecombe's electron localization function [173] (ELF), as generalized by Burnus, Marques, and Gross for time-dependent cases [174]. Section 6.5.1 will show how the Fermi hole appears naturally in the derivation of the ELF.

An alternative way to rationalize the ELF definition is to think in terms of how Pauli's exclusion principle affects the kinetic energy. This principle applies to fermionic systems; the kinetic energy of a bosonic system is a lower bound to the local kinetic energy of a fermionic one [175]. Thus we can define an *excess kinetic energy*, which would be the difference between the two of them. Intuitively, in a region of electron localization (electrons forming pairs, isolated electrons), their behavior is more bosonic-like. So we will require, to define localization, that the excess kinetic energy is minimized. This is indeed the case for the ELF, as it will be demonstrated later.

The ELF, as introduced by Becke and Edgecombe, involved two approximations: (i) First, it assumed that the many-electron wave function is a single Slater determinant. The natural choice is the Hartree-Fock solution. (ii) Secondly, it assumed that the single-particle orbitals that form the single Slater determinant are *real functions*. This prevents its validity in a time-dependent formalism, or for static but current-carrying states. A generalized derivation that lifted this restriction was presented by Dobson [176], and later by Burnus, Marques, and Gross [174] who demonstrated how this general form could be applied for time-dependent processes. The observation of this function is useful for the study of chemical reactions and for processes that involve the interaction of molecular systems with high-intensity ultra-short laser pulses (femtosecond or even attosecond regime), or collision processes between molecules and/or ions. In this time scale, and for these probably violent deformations of the molecular fields, the electrons are bound to exhibit a complex behavior: bonds are destroyed or created, bond types change as the molecules isomerize, dissociate, or recombine in chemical reactions. These events are especially patent in the evolution of the ELF.

Next subsection is dedicated to the definition of the (possibly time-dependent) ELF. In Sect. 6.5.2, some examples of the ELF for systems in the ground state are shown, in order to illustrate the association between ELF topological features and Chemistry bonding elements. Sect. 6.5.3 provides examples of time-dependent calculations in which the TDELF is monitored: collision processes leading to chemical reactions, and interaction of molecules with laser pulses. The chapter closes, in Sect. 6.5.4, with an example in which the coupled evolution of electrons and nuclei, both treated quantum-mechanical, is computed for a model system. The ELF is then used to learn about the strength of nonadiabatic effects.

6.5.1 The time-dependent electron localization function

6.5.1.1 General definition

We depart from the definitions of the one and two-body density matrices for a system of N electrons [177, 178], whose evolution is described by the wave function $\Psi(\boldsymbol{r}_1\sigma_1, ..., \boldsymbol{r}_N\sigma_N; t)$:

$$\Gamma^{(1)}_{\sigma_1|\sigma_1'}(\boldsymbol{r}_1|\boldsymbol{r}_1'; t) = N \sum_{\sigma_2,\ldots,\sigma_N} \int \mathrm{d}^3r_2 \ldots \int \mathrm{d}^3r_N \, \Psi^\star(\boldsymbol{r}_1\sigma_1, \boldsymbol{r}_2\sigma_2, ..., \boldsymbol{r}_N\sigma_N; t) \times \Psi(\boldsymbol{r}_1'\sigma_1', \boldsymbol{r}_2\sigma_2, ..., \boldsymbol{r}_N\sigma_N; t)\,, \tag{6.12}$$

$$\Gamma^{(2)}_{\sigma_1,\sigma_2|\sigma_1'\sigma_2'}(\boldsymbol{r}_1, \boldsymbol{r}_2|\boldsymbol{r}_1'\boldsymbol{r}_2'; t) = N(N-1) \sum_{\sigma_3,\ldots,\sigma_N} \int \mathrm{d}^3r_3 \ldots \int \mathrm{d}^3r_N \, \Psi^\star(\boldsymbol{r}_1\sigma_1, \boldsymbol{r}_2\sigma_2, ..., \boldsymbol{r}_N\sigma_N; t)\Psi(\boldsymbol{r}_1'\sigma_1', \boldsymbol{r}_2'\sigma_2', ..., \boldsymbol{r}_N\sigma_N; t)\,. \tag{6.13}$$

The spin-densities are defined in terms of the diagonal one-body density matrix:

$$n_\sigma(\boldsymbol{r}, t) = \Gamma^{(1)}_{\sigma|\sigma}(\boldsymbol{r}|\boldsymbol{r}; t)\,. \tag{6.14}$$

For equal spin ($\sigma_1 = \sigma_2 = \sigma$), the diagonal of the two-body density matrix, that is, $\Gamma^{(2)}_{\sigma\sigma|\sigma\sigma}(\boldsymbol{r}_1, \boldsymbol{r}_2|\boldsymbol{r}_1\boldsymbol{r}_2; t)$, is the same-spin pair probability function, $D_\sigma(\boldsymbol{r}_1, \boldsymbol{r}_2; t)$. Its value is the probability of finding one electron at $\boldsymbol{r}_1$ and another electron at $\boldsymbol{r}_2$, both with the same spin σ:

$$D_\sigma(\boldsymbol{r}_1, \boldsymbol{r}_2; t) = \Gamma^{(2)}_{\sigma\sigma|\sigma\sigma}(\boldsymbol{r}_1, \boldsymbol{r}_2|\boldsymbol{r}_1, \boldsymbol{r}_2; t)\,. \tag{6.15}$$

If the electrons were *uncorrelated*, the probability of finding the pair of electrons at $\boldsymbol{r}_1$ and $\boldsymbol{r}_2$ would be the product of the individual probabilities: $D_\sigma(\boldsymbol{r}_1, \boldsymbol{r}_2; t) = n_\sigma(\boldsymbol{r}_1; t)n_\sigma(\boldsymbol{r}_2; t)$. Electrons are, however, correlated, and the same-spin pair density is less than that value by a factor that is defined as the *pair correlation function*:

$$D_\sigma(\boldsymbol{r}_1, \boldsymbol{r}_2; t) = n_\sigma(\boldsymbol{r}_1; t)n_\sigma(\boldsymbol{r}_2; t)g_{\sigma\sigma}(\boldsymbol{r}_1, \boldsymbol{r}_2; t)\,. \tag{6.16}$$

The difference between the correlated and the uncorrelated case is also contained in the *Fermi hole* function $h_\sigma(\boldsymbol{r}_1, \boldsymbol{r}_2; t)$:

$$D_\sigma(\boldsymbol{r}_1, \boldsymbol{r}_2; t) = n_\sigma(\boldsymbol{r}_1; t)\left(n_\sigma(\boldsymbol{r}_2; t) + h_{\sigma\sigma}(\boldsymbol{r}_1, \boldsymbol{r}_2, t)\right)\,. \tag{6.17}$$

The same-spin *conditional* probability function, $P_\sigma(\boldsymbol{r}_1, \boldsymbol{r}_2; t)$ is then defined as the probability of finding a σ-spin electron at $\boldsymbol{r}_2$, knowing that there is one σ-spin electron at $\boldsymbol{r}_1$. It can be expressed in terms of the previous definitions:

$$P_\sigma(\boldsymbol{r}_1, \boldsymbol{r}_2; t) = \frac{D_\sigma(\boldsymbol{r}_1, \boldsymbol{r}_2; t)}{n_\sigma(\boldsymbol{r}_1; t)} = n_\sigma(\boldsymbol{r}_2; t) g_{\sigma\sigma'}(\boldsymbol{r}_1, \boldsymbol{r}_2; t) = n_\sigma(\boldsymbol{r}_2; t) + h_{\sigma\sigma}(\boldsymbol{r}_1, \boldsymbol{r}_2; t) . \tag{6.18}$$

From this equation, the meaning of the Fermi hole (a negative function at all points) is more transparent: it is a measure of how probability at $\boldsymbol{r}_2$ is reduced due to the spreading out of the same spin density originated at $\boldsymbol{r}_1$.

However, it will be more useful to define an alternative same-spin conditional pair probability function: given a reference electron of σ-spin at $\boldsymbol{r}$, we are interested in the probability of finding a same-spin electron at a distance s. This involves taking a spherical average on a sphere of radius s around point $\boldsymbol{r}$, $S(s, \boldsymbol{r})$:

$$p_\sigma(\boldsymbol{r}, s; t) = \frac{1}{4\pi} \int_{S(s,\boldsymbol{r})} \mathrm{d}S P_\sigma(\boldsymbol{r}, \boldsymbol{r}'; t) . \tag{6.19}$$

The integration is done for the $\boldsymbol{r}'$ variable. For small values of s one can obtain the following Taylor expansion:

$$p_\sigma(\boldsymbol{r}, s; t) = \frac{1}{3} \left[\frac{1}{2} \frac{\left[\nabla^2_{\boldsymbol{r}'} D_\sigma(\boldsymbol{r}, \boldsymbol{r}'; t)\right]_{\boldsymbol{r}'=\boldsymbol{r}}}{n_\sigma(\boldsymbol{r}, t)} \right] s^2 + \mathcal{O}(s^3) . \tag{6.20}$$

In this expansion, the term in s^0 is absent due to the Pauli exclusion principle. The linear term in s is also null [179]. The coefficient of s^2 (except for the one-third factor) thus tells us about the same-spin pair probability in the vicinity of $\boldsymbol{r}$:

$$C_\sigma(\boldsymbol{r}) = \frac{1}{2} \frac{\left[\nabla^2_{\boldsymbol{r}'} D_\sigma(\boldsymbol{r}, \boldsymbol{r}'; t)\right]_{\boldsymbol{r}'=\boldsymbol{r}}}{n_\sigma(\boldsymbol{r}, t)} . \tag{6.21}$$

This function is an *inverse* measure of localization: it tells us how large the same-spin conditional probability function is at each point in space. The smaller this magnitude is, the more likely than an electron *avoids* electrons of equal spin.

In addition to having an inverse relationship to localization – for example, it is null for perfect localization –, C_σ is not bounded by above. Visually, it does not mark the chemical structure with great contrast. These reasons led Becke and Edgecombe to suggest a re-scaling, noticing that, for the homogeneous electron gas, C_σ is nothing else than the kinetic energy density (atomic units will be used in all equations of this section):

$$C_\sigma^{\mathrm{HEG}} = \tau_\sigma^{\mathrm{HEG}} = \frac{3}{5}(6\pi^2)^{(2/3)} n_\sigma^{(5/3)} . \tag{6.22}$$

One may then refer the value of C_σ at each point to the value that the homogeneous electron gas would have for the density of that point at that time t,

$C_\sigma^{\mathrm{HEG}}(\boldsymbol{r};t)$. Moreover, since there is an inverse relationship between C_σ and localization, it is useful to invert it. The final expression for the “electron localization function”, $\eta_\sigma(\boldsymbol{r})$, is

$$\eta_\sigma(\boldsymbol{r};t) = \frac{1}{1 + (C_\sigma(\boldsymbol{r};\boldsymbol{t})/C_\sigma^{\mathrm{HEG}}(\boldsymbol{r};t))^2}\,. \tag{6.23}$$

6.5.1.2 Expression for one-determinantal wave functions

Up to this point, the equations allow for complete generality. Equation (6.23) in particular, together with (6.21), defines the ELF for any system, either in the ground state or in a time-dependent situation, and regardless of which scheme is chosen to approximate a solution to the many electron problem. However, the ELF was originally introduced assuming a Hartree-Fock formulation (one determinantal character of the many-body wave function). The formulation may thus be translated to the Kohn-Sham (KS) formulation of density-functional theory (DFT).

For one-determinantal wave functions, the function C_σ (6.21) may be explicitly calculated. Let us assume the Slater determinant to be formed of the orbitals $\{\varphi_{i\uparrow}\}_{i=1}^{N_\uparrow}$ and $\{\varphi_{i\downarrow}\}_{i=1}^{N_\downarrow}$, for spin up and down, respectively ($N = N_\uparrow + N_\downarrow$). In this case, one can use the two following identities:

$$\Gamma^{(1)}(\boldsymbol{r}_1\sigma|\boldsymbol{r}_2\sigma;t) = \sum_{i=1}^{N_\sigma} \varphi_{i\sigma}^*(\boldsymbol{r}_2;t)\varphi_{i\sigma}(\boldsymbol{r}_1;t)\,. \tag{6.24}$$

$$\text{(This implies immediately:} \quad n_\sigma(\boldsymbol{r},t) = \sum_{i=1}^{N_\sigma} |\varphi_{i\sigma}(\boldsymbol{r},t)|^2\,.\text{)}$$

$$D_\sigma(\boldsymbol{r}_1.\boldsymbol{r}_2;t) = n_\sigma(\boldsymbol{r}_1;t)n_\sigma(\boldsymbol{r}_2;t) - |\Gamma^{(1)}(\boldsymbol{r}_1\sigma|\boldsymbol{r}_2\sigma;t)|^2\,. \tag{6.25}$$

Equations (6.24) and (6.25) are then introduced in the expression for C_σ, (6.21):

$$C_\sigma(\boldsymbol{r};t) = \frac{1}{2}\left[\nabla^2_{\boldsymbol{r}'} n_\sigma(\boldsymbol{r}';t)\right]_{\boldsymbol{r}'=\boldsymbol{r}} - \frac{1}{2}\left[\nabla^2_{\boldsymbol{r}'}\frac{|\Gamma^{(1)}(\boldsymbol{r}'|\boldsymbol{r};t)|^2}{n_\sigma(\boldsymbol{r};t)}\right]_{\boldsymbol{r}'=\boldsymbol{r}}\,. \tag{6.26}$$

And after some algebra [180]:

$$C_\sigma(\boldsymbol{r};t) = \tau_\sigma(\boldsymbol{r};t) - \frac{1}{4}\frac{(\nabla n_\sigma(\boldsymbol{r};t))^2}{n_\sigma(\boldsymbol{r};t)} - \frac{j_\sigma^2(\boldsymbol{r};t)}{n_\sigma(\boldsymbol{r};t)}\,. \tag{6.27}$$

where $\tau_\sigma(\boldsymbol{r};t)$ is the kinetic energy density,

$$\tau_\sigma(\boldsymbol{r};t) = \sum_{i=1}^{N_\sigma} |\nabla\varphi_{i\sigma}(\boldsymbol{r};t)|^2\,, \tag{6.28}$$

and $j^2_\sigma(\boldsymbol{r};t)$ is the squared modulus of the current density:

$$\boldsymbol{j}_\sigma(\boldsymbol{r};t) = \langle\Psi(t)| \ \frac{1}{2m}\sum_{i=1}^{N}\left[\delta(\boldsymbol{r}-\hat{\boldsymbol{r}}_i)\delta_{\sigma\sigma_i}\hat{\boldsymbol{p}}_i + \hat{\boldsymbol{p}}_i\delta(\boldsymbol{r}-\hat{\boldsymbol{r}}_i)\delta_{\sigma\sigma_i}\right] \ |\Psi(t)\rangle =$$

$$\frac{1}{2\mathrm{i}}\sum_{i=1}^{N_\sigma}\left[\varphi^*_{i\sigma}(\boldsymbol{r};t)\boldsymbol{\nabla}\varphi_{i\sigma}(\boldsymbol{r};t) - \varphi_{i\sigma}(\boldsymbol{r};t)\boldsymbol{\nabla}\varphi^*_{i\sigma}(\boldsymbol{r};t)\right] . \qquad (6.29)$$

Expression (6.27), upon substitution in (6.23), leads to the general form for the ELF, if one assumes one-determinantal wave functions. In the original derivation, however, a further restriction was introduced from the beginning: the system is assumed to be in the a stationary state, and the single-particle orbitals are real, which implies zero current. The derivation presented above [174,180], however, allows for time-dependent Slater determinants (and complex ground-states with non-null current).

The original, "static" ELF, is simply obtained by eliminating the current term from the expression for C_σ (6.27):

$$C^{\mathrm{static}}_\sigma(\boldsymbol{r}) = \tau_\sigma(\boldsymbol{r}) - \frac{1}{4}\frac{(\nabla n_\sigma(\boldsymbol{r}))^2}{n_\sigma(\boldsymbol{r})} \, , \qquad (6.30)$$

and plugging this formula in the ELF definition, (6.23).

At this point, it is worth noting that this expression is nothing else than the "excess kinetic energy" mentioned in the introduction of this Section. The first term, $\tau(\boldsymbol{r})$ (summing over the two spins) is the local kinetic energy of the electronic system. A bosonic system of equal density n, at its ground state, will concentrate all particles at the ground state orbital, $\sqrt{n}/N$. From this fact it follows that the second term of the previous equation is the kinetic energy density of the bosonic system. It is thus clear how the high localization corresponds to a minimization of the excess kinetic energy.

6.5.1.3 Density-functional theory approximation to the ELF

It is useful to briefly recall here the essential equations of DFT [168–170] and of TDDFT [181–186], since these are the theories that are employed to obtain the orbitals from which the ELF is calculated in the examples presented in the following subsection.

There exists a one-to-one correspondence between the ground-state density of a many electron system, n, and its external potential v. This permits to write every observable as a functional of the density. For each interacting system, there also exists an auxiliary noninteracting system of fermions, subject to an external potential different to the one in the original system, such that the densities of the two systems are identical. One can then solve this noninteracting system, and obtain any observable of the interacting system by using the appropriate functional of the density.

The one-particle equations that provide the single-particle orbitals that conform the one-determinantal solution to the noninteracting problem are the so-called Kohn-Sham equations:

$$\{-\frac{1}{2}\nabla^2 + v_{\mathrm{KS}}(\boldsymbol{r})\}\ \varphi_i(\boldsymbol{r}) = \varepsilon_i \varphi_i(\boldsymbol{r})\,, \quad i = 1, ..., N. \tag{6.31}$$

The density of both the interacting and noninteracting system is then simply:

$$n(\boldsymbol{r}) = \sum_{i=1}^{N} |\varphi_i(\boldsymbol{r})|^2\,. \tag{6.32}$$

The problem lies in the calculation of the Kohn-Sham potential, $v_{\mathrm{KS}}(\boldsymbol{r})$, itself a functional of the density. For this purpose, it is usually split into a known and an unknown part – the latter being the so-called exchange and correlation potential $v_{\mathrm{xc}}(\boldsymbol{r})$:

$$v_{\mathrm{KS}}(\boldsymbol{r}) = v(\boldsymbol{r}) + \int \mathrm{d}^3 r'\ \frac{n(\boldsymbol{r})}{|\boldsymbol{r} - \boldsymbol{r}'|} + v_{\mathrm{xc}}(\boldsymbol{r})\,. \tag{6.33}$$

TDDFT extends the parallelism between the interacting and the noninteracting system to time-dependent systems [181]. One then has to deal with time-dependent Kohn-Sham equations:

$$\mathrm{i}\frac{\partial \varphi_i}{\partial t}(\boldsymbol{r};t) = \{-\frac{1}{2}\nabla^2 + v_{\mathrm{KS}}(\boldsymbol{r};t)\}\ \varphi_i(\boldsymbol{r};t)\,, \quad i = 1, ..., N. \tag{6.34}$$

Once again, an approximation to a time-dependent exchange and correlation potential is needed.

The ELF is calculated in terms of spin-orbitals, and is not an explicit functional of the density. One may then approximate the ELF of the interacting system by considering the ELF of its corresponding Kohn-Sham system – whose state is a Slater determinant, and can be calculated using the previous equations. Note that this is a completely different approximation to the one taken by considering the Hartree-Fock ELF – even if it leads to an analogous expression. However, it has been shown that the main features of the ELF are rather insensitive to the method utilized in its calculation [187, 188], even for more approximate schemes such as the extended Hückel model.

6.5.2 Examples in the ground-state

This subsection will present some applications of the ELF for systems in the ground state. All calculations have been done within the KS/DFT formalism. For the exchange-correlation potential, the local-density approximation (LDA) has been employed in all cases, except for the water molecule and the hydroxide ion, for which – both in the ground state calculations and in the collision processes presented in the next subsection – the self-interaction correction was added. The resulting functional is orbital dependent, and in order to calculate it, one has to make use of the optimized effective potential theory – together, in this case, with the approximation of Krieger, Li, and Iafrate [189]. The functions are represented on a real-space regular rectangular grid (base-less approach). The pseudopotential approach is taken for the ion-electron interaction in order to avoid the explicit treatment of the chemically inert core electrons.[2] The motion of the cores is treated classically. The computations have been carried out with the `octopus` code [190, 191].

In order to appreciate the usefulness of the ELF to monitor fast, time-dependent molecular processes, it is important to learn the characteristics of the ELF in the ground state. Silvi and Savin [192] outlined a proposal for the classification of chemical bonds based on the topological analysis of the ELF. Let us recall here some basic ideas, illustrated below with some examples. The ELF is a scalar real function, bounded between zero and one – the value one corresponding to maximum localization. The *attractors* are the points where it has maxima; to each attractor corresponds a *basin*, the set of points whose gradient field drives to the attractor. The shape of the isosurfaces of the ELF is also informative: as we change the isosurface value, it may or may not change – when it does, we have a *bifurcation*, which occurs at ELF *critical values*. The attractors may have zero, one, or two dimensions: In general, only zero dimensional attractor are allowed; however system with spherical symmetry (atoms) will have spherical (2D) attractor manifolds, whereas $C_{\infty v}$ (or higher) systems (linear molecules) may have one-dimensional sets of attractors, forming a ring around the molecular axis.

To each attractor one may associate an *irreducible f-localization domain*. An f-localization domain is the set of connected points for which the ELF is larger than f. It is irreducible if it only contains one attractor. The spatial arrangement of these domains is the key to classify chemical bonds: there are three types of attractors: core (its domain contains a nuclei), bonding (located between the core attractors of different atoms) and nonbonding (the rest, that contain the so-called lone pairs). All atoms will have an associated core attractor, except hydrogen.

In each domain, one may integrate the electronic density, and obtain a number of electrons. In the absence of symmetry, at most two electrons with opposite spins should be found in a basin. An attractor for which the number of electrons in its associated domain is less than two is an *unsaturated attractor*. A multiple bond is created when there is more than one bonding attractor between two core attractors. A ring attractor containing six electrons is also a multiple bond.

---

[2] It may be argued that the ELF that we depict, is, in fact, a pseudo-ELF. The effect of removing the core electrons in the ELF is the removal of localized electrons in the vicinity of the nuclei. This is irrelevant if one is interested in learning about the chemical properties of the systems.

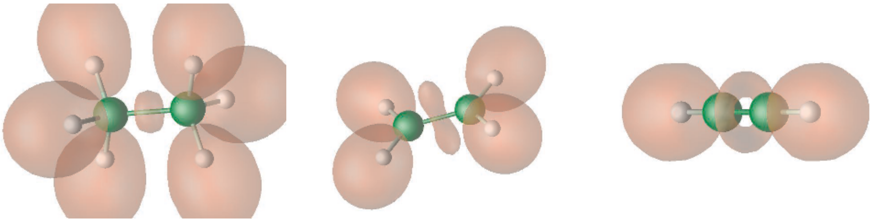

Fig. 6.42. ELF isosurfaces ($\eta = 0.85$) of ethane (left), ethene (center) and ethyne (right).

A first illustrative example is the clear distinction between the single, double and triple bonds of the ethane, ethene and ethyne molecules, as presented in Fig. 6.42. The ethyne (acetylene) molecule is an example of linear molecule ($D_{\infty h}$ symmetry), which allows for continuous ring attractors. These may occur specially for cases in which one expects a triple bond, such as is the case in acetylene. However, other textbook "Lewis" triple bonds do not show a ring attractor: the nitrogen molecule presents only one point attractor between the nuclei, and two other point attractor at their sides. The double bond of ethene (center in Fig. 6.42) is clearly manifested by the presence of two attractors between the carbons. This leads to isosurfaces with a characteristic "eight" shape. The ethane molecule (left), presents only one attractor between the carbons (single bond), and the six domains corresponding to the CH bonds.

It is known that the ring isomer of C_{20} (see Fig. 6.43, left side) does not have a 20th order axis of symmetry, due to the presence of alternating bonds, which reduces the molecule symmetry group to C_{10h}. The different nature of the bonds ("single-triple alternation", in the Lewis picture), is clearly patent in the ELF: the continuous ring of attractors for the triple bonds, whereas one single point attractor for the single bonds. In the case of the C_{60} fullerene (see Fig. 6.43, right side) due to its high symmetry, there are also in principle two possibly different kinds of bonds: the ones for which the bond line is separating two hexagons, and the ones for which the bond line is separating one pentagon and one hexagon. A look at the ELF tells us that the character of these bonds is, however, very similar.

The usefulness of the ELF is specially patent for the analysis of nonbonding electron groups [193]. In Fig. 6.44 two examples are shown: the hydroxide (OH^-) ion, and the water molecule. In the first case (right), there is once again a continuous ring attractor, that contains six electrons. This reflects in the torus-like shape of the isosurfaces defined in its domain. The water molecule, on the contrary, breaks the linear symmetry, and thus does not permit for continuous attractors. In this case one can see, in addition to two isosurfaces in the CH bond basins, one "bean"-shaped isosurface, that contains two point attractors on each side of the oxygen atom. Each irreducible domain, corresponding to each of these two attractors, contains two electrons.

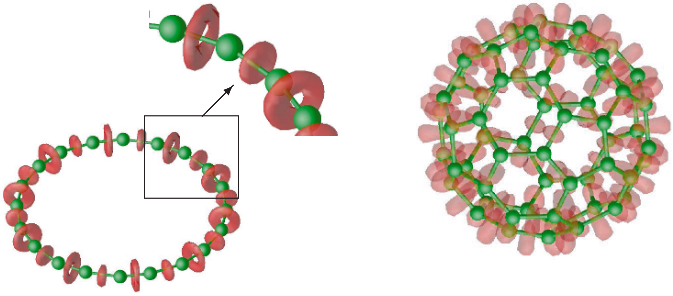

Fig. 6.43. ELF isosurfaces ($\eta = 0.85$) for the ring isomer of C_{20} (left), and for the C_{60} fullerene.

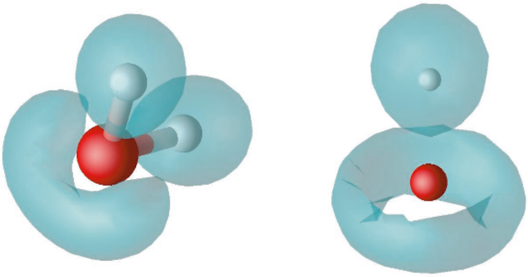

Fig. 6.44. ELF isosurfaces ($\eta = 0.85$) of the water molecule (left), and of the hydroxide ion (right), showing the very different shape of the lone pair basin with four electrons (two point attractors, as it is the case for water), and with six electrons (ring-shaped attractor, as it is the case for the hydroxide ion).

Figs. 6.45 and 6.46 present another case: the formaldimine molecule (also referred to as the smallest imine, or as the smallest unprotonated Schiff base). This molecules presents a double bond between carbon and nitrogen, and a lone pair attached to the nitrogen atom. The upper figures of Fig. 6.45 depict the electronic density: an isosurface on the left, and a logarithmic color map on the plane of the molecule on the right. Below, the figures depict the ELF in the same way – although the scale of the colormap in this case is not logarithmic. Both the bond (and its type) and the lone pair are clearly visible in the ELF, whereas the density presents much less structure.

Fig. 6.46 displays the same formaldimine molecule; however, it shows the gradient lines of the ELF, which converge in the attractors. This alternative pictorial representation is also helpful to identify the positions of the attractors.

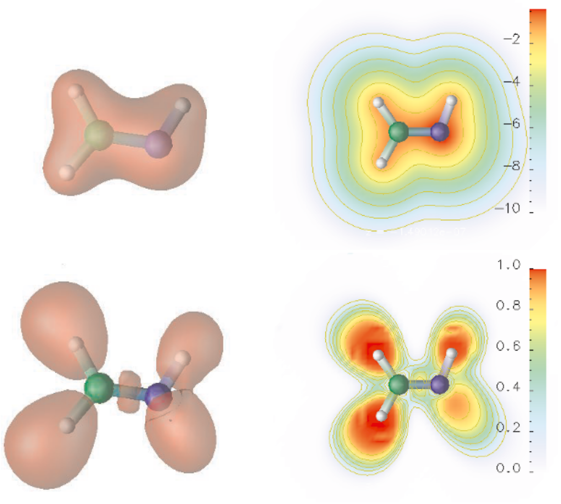

Fig. 6.45. Electronic density (top) and ELF (bottom, see text for its definition) of the ground state of the formaldimine molecule. Left figures show one three dimensional isosurface, whereas the right figures show a color-mapped two dimensional plane. Note that the scale in the case of the density is logarithmic; the values in the legend reflect the exponent.

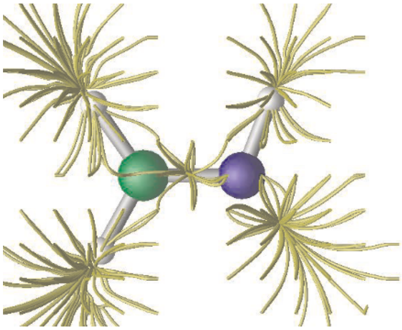

Fig. 6.46. Streamlines running through the gradient field of the ELF of formaldimine, and meeting at the basin attractors – the ELF local maxima.

6.5.3 Fast processes

The following time-dependent calculations of the ELF have been done by making use of TDDFT to describe the many-electron system. On top of this, the ions are also allowed to move. These are treated classically as point particles (the next subsection describes a model in which this restriction is lifted). The forces that define the ionic movement are calculated through Ehrenfest's theorem. It amounts to the simultaneous and coupled evolution of both a classical and a quantum system. The resulting Molecular Dynamics is nonadiabatic, since the electrons may occupy any excited state, and change these occupations.

6.5.3.1 The $H^+ + OH^- \rightarrow H_2O$ reaction.

In the following, the TDELF is used to monitor, “in real time”, the chemical behavior of the electrons involved in a chemical reaction. In this case, a specially simple one: the formation of a water molecule after the collision of a proton and a OH^- group.

One should recall, first of all, the topological differences between the lone-pair basin in the water molecule, containing two pairs, and the ring-shaped basin of the hydroxide ion (see Fig. 6.44). The chemical reaction that produces water should involve the transformation of this lone-pair basin. The collision of the two reactants produces different results depending on the original velocities and orientations; two typical outcomes are presented here: a successful event (meaning formation of water), and an unsuccessful collision, leading to three isolated nuclei.

Fig. 6.47 shows the first of these two cases. At time zero, one can identify the characteristic ELF of the ground-state hydroxide ion. Note that this figure depicts isosurfaces of the ELF at a value of $\eta = 0.8$, and these isosurfaces are color-coded: an intense red means a region of high electronic density, whereas the whitish areas of the isosurfaces correspond to regions of almost negligible density. This is done in order to make apparent one of the less intuitive features of the ELF: it may have large values in regions of low electronic density.

The proton and the hydroxide group initially approach each other with a velocity of 10^{-2} a.u., or 0.21 Å/fs. The proton is directed to the middle point of the ion. As the proton approaches the hydroxide group in the first snapshots, an accumulation of ELF becomes apparent near it. This corresponds to a small transfer of electronic density – even if this density will be strongly localized and very large in size (see that snapshot taken at 9.7 fs), the amount of charge transfer is minute. This fact may be learnt from the lack of red color in this isosurface.

In the snapshots of the second row, the proton collides with the hydroxide group, and as a result the two protons jump away off the oxygen atom. Each proton has now its associated ELF basin, whereas the lone pairs basin associated to oxygen is already distorted. The last snapshots in the third row show the return of the protons to the influence of the oxygen core, which demonstrates that water has been formed. The very last snapshot, some 30 fs after the process was initiated, clearly depicts the lone-pairs basin with the typical “bean” shape corresponding to two electron pairs. Note, however, that both nuclear and electronic degrees of freedom are in highly excited state, and thus the final picture is not a steady structure.

Fig. 6.48 shows another possibility, which occurs for higher proton velocities. In this case, the simulation is illustrated with a different representation

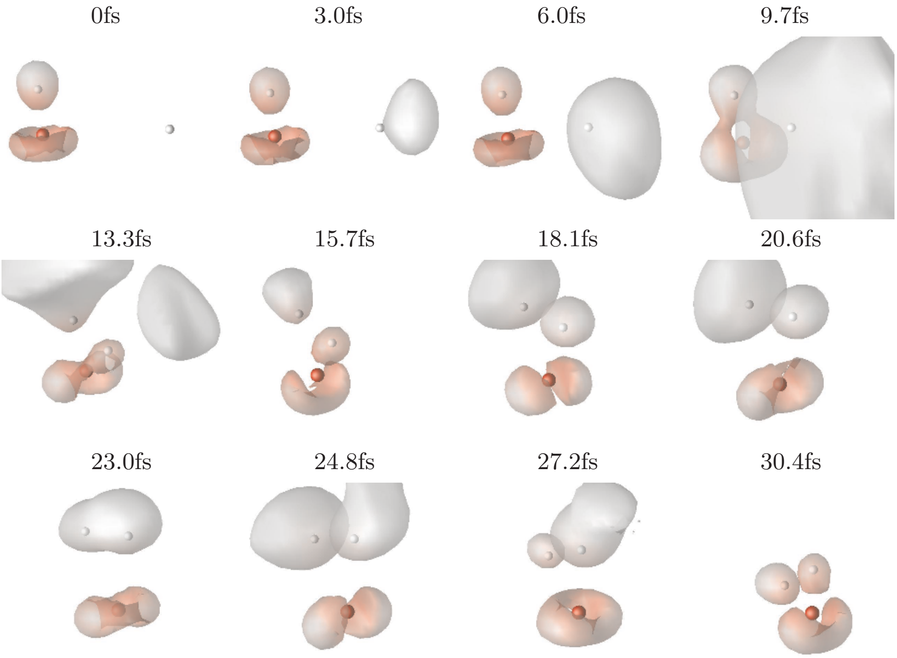

Fig. 6.47. Snapshots taken during the formation of a water molecule due to the collision of a proton and a OH^- group. Isosurfaces for the ELF at a value of $\eta = 0.8$ are shown in red. This red color, however, is graduated depending on the local value of the electronic density: more intense red means higher density. The white areas, thus, correspond to regions of high electronic localization but low density. The oxygen core is colored in red, whereas the protons are colored in white.

procedure: a color map on the plane in which the three atoms move. The initial geometry is similar, but in this case the relative velocity is 5×10^{-2} a.u., or 1.1 Å/fs. Once again, the second snapshot shows how a cloud of localized electrons develops around the proton as it approaches the anion. It becomes specially large after 2.9 fs; note however that it does not mean a large electronic transfer; to learn about that one needs to look at the density. In the fourth snapshot, the incoming proton cleanly passes through the bond. The original shape of the ELF is completely distorted; however the speed of the process did not allow yet for fast movements of the nuclei – except the straight line movement due to their original velocities.

In the second row one may see the proton scatter away from the anion; it does so at an angle from its initial trajectory. The bond of the anion is broken; as a consequence the two nuclei separate from each other. Each of the three nuclei carries away an electronic cloud: a spherical crown in the case of the oxygen atom (corresponding to the typical two dimensional spherical attractor of an isolated many electron atom), and spatially large accumulations of localized electrons for the protons (note, once again, that this does not imply a large number of electrons. In order to learn about the electronic charge carried away by each of the ions, it is necessary to integrate the density in each of the localization domains).

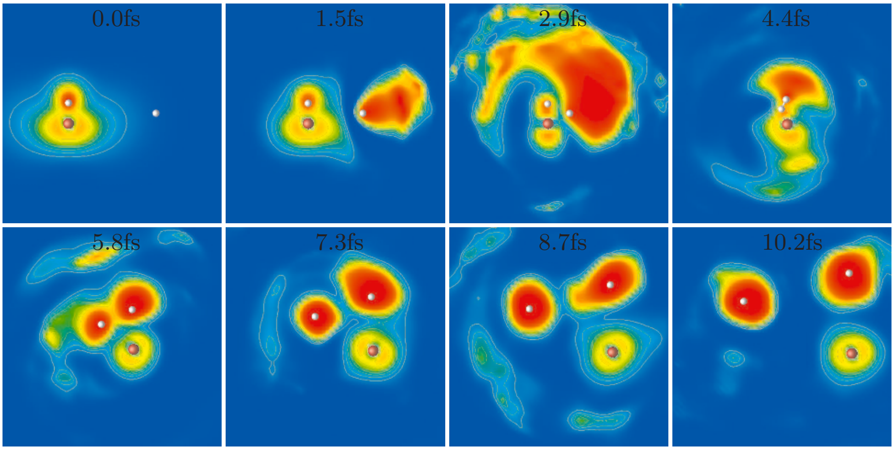

Fig. 6.48. Snapshots taken during the collision of a hydroxide ion with a proton, leading to the dissociation of the hydroxide group.

6.5.3.2 Proton capture by a lone pair

The next case focuses in the formaldimine molecule, Fig. 6.46. It presents one lone pair, which chemically may behave as a possible anchorage for a radical. For example, it may attract a "traveling" proton in an acid environment. This is demonstrated in the simulation depicted in Fig. 6.49.

In the first snapshot, the formaldimine molecule is in its ground state, both its electronic and nuclear degrees of freedom. The topology of the ELF for this particular case was discussed in the previous subsection. A proton travels with a velocity of 5.2×10^{-3} atomic units (corresponding to an energy of $0.673\,\mathrm{eV}$), in the plane of the molecule, and initially aiming to the center of the CN double bond. The lone pair, however, attracts the proton to its basin. As a result, the proton drifts to the right, in the direction of the nitrogen atom, accelerating its movement. The molecule itself also rotates as the nitrogen atom attempts to approach the incoming proton. This enters the nonbonding basin, and transforms it into a bonding NH loge. The ensuing collision results in the proton quickly accelerating out of the molecule; however, the bond has been established, and soon it is driven back. The result is a highly excited molecule: the nuclei will vibrate, whereas the electronic state will also be a mixture of the ground state and higher lying states. Of course, eventually it could relax upon photon emission; this is however not included in the model.

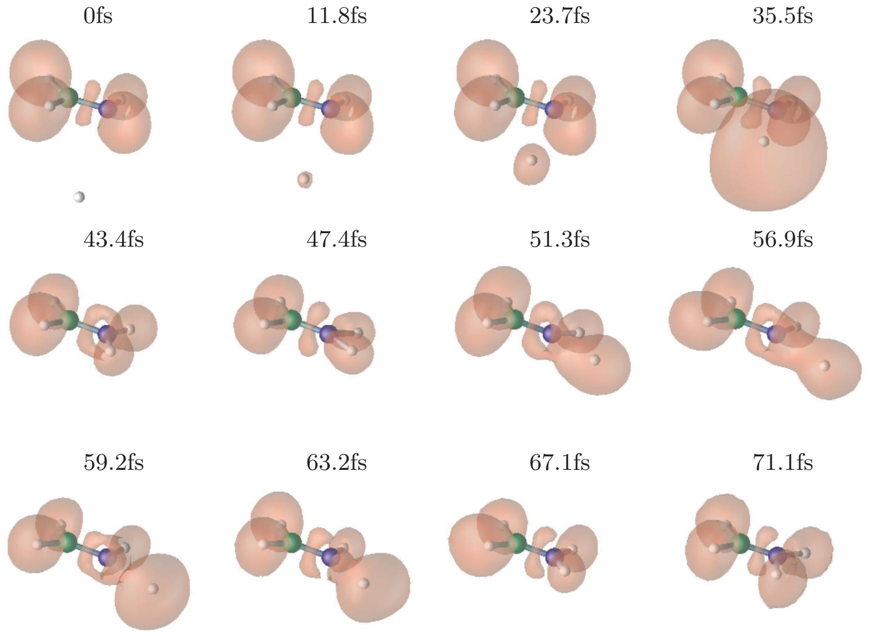

Fig. 6.49. Snapshots taken during the capture of a proton by a formaldimine molecule. Isosurfaces for the ELF at a value of $\eta = 0.8$ are shown in red. The carbon and nitrogen cores are colored in green and blue respectively, whereas the protons are colored in white.

6.5.3.3 Bond-breaking by an intense, ultrafast laser pulse

The next example shows the excitation of the ethyne molecule by means of a strong laser. The aim is especially the triple bond. The laser is polarized along the molecular axis; it has a frequency of 17.15 eV ($\lambda = 72.3\,\text{nm}$) and a maximal intensity of $I_m = 1.19 \times 10^{14}\,\text{Wcm}^{-2}$. Fig. 6.50 depicts snapshots of the ELF of acetylene in form of slabs through a plane of the molecule. At the beginning (a) the system is in the ground state and the ELF visualizes these features: The torus between the carbon atoms, which is typical for triple bonds, and the blobs around the hydrogen atoms. As the intensity of the laser increases, the system starts to oscillate and then ionizes (Fig. 6.50b,c). Note that the ionized charge leaves the system in fairly localized packets (the blob on the left in b, and on the right in c). The central torus then starts to widen (Fig. 6.50d) until it breaks into two tori centered around the two carbon atoms (Fig. 6.50e,f). This can be interpreted as a transition from the π bonding to the $\pi^\star$ nonbonding state. The system then remains in this excited state, and eventually dissociates, after the laser has been switched off. In the process,

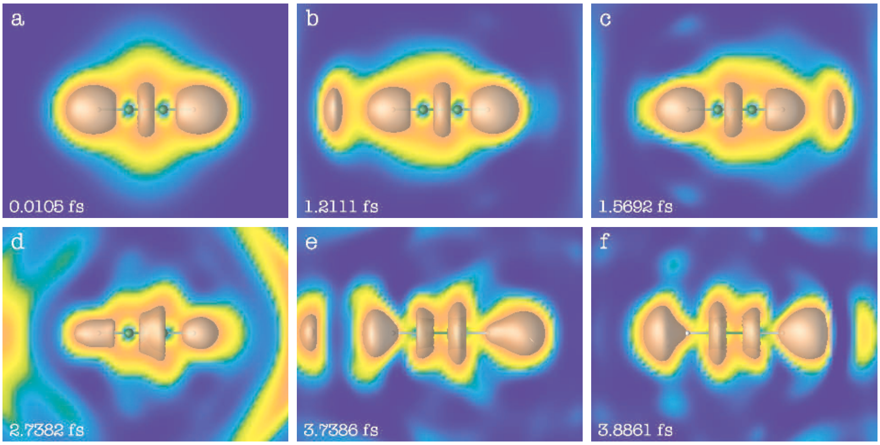

Fig. 6.50. Snapshots of the time-dependent ELF for the excitation of ethyne (acetylene) by a 17.15 eV ($\lambda = 72.3$ nm) laser pulse. The pulse had a total length of 7 fs, a maximal intensity of 1.2×10^{14} Wcm^{-2}, and was polarized along the molecular axis. Ionization and the transition from the bonding π to the anti-bonding $\pi^\star$ are clearly visible.

the molecule absorbs about 60 eV of energy, and looses 1.8 electrons through ionization.

6.5.4 TDELF for coupled nuclear-electronic motion

The examples presented in the previous subsection neglected the quantum nature of the atomic nuclei. Erdmann, Gross, and Engel [194] have presented one application of the TDELF for a model system in which one nucleus is treated quantum mechanically, and the full Schrödinger equation is computed exactly. This model is specially suited to study, from a fundamental point of view, the effects of nonadiabaticity. It is instructive to see how the ELF may help for this purpose.

The model is depicted in Fig. 6.51: two electrons and a nucleus that move in a single dimension between two fixed ions. Its Hamiltonian is:

$$H(x, y, R) = T(x) + T(y) + T(R) + V(x, y, R)\,, \tag{6.35}$$

where $T(x)$, $T(y)$ and $T(R)$ are the kinetic energy operator of the two electrons and of the moving ion, respectively. The potential is:

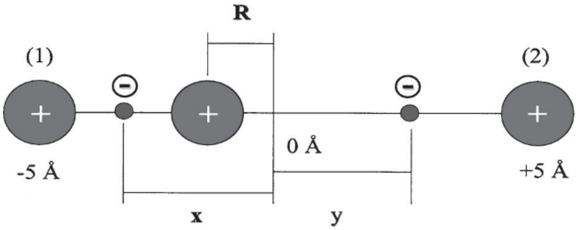

Fig. 6.51. Configuration of the model system: An ion (coordinate R) and two electrons (at x and y) are allowed to move between two fixed ions (1) and (2), fixed at a distance of 10Å.

$$\begin{aligned} V(x,y,R) = {} & \frac{Z_1 Z}{|R_1 - R|} + \frac{Z_2 Z}{|R_2 - R|} + \frac{\mathrm{erf}(|x-y|)}{R_e|x-y|} \\ & - \frac{Z_1 \mathrm{erf}(|R_1 - x|)}{R_f|R_1 - x|} - \frac{Z_2 \mathrm{erf}(|R_2 - x|)}{R_f|R_2 - x|} - \frac{Z \mathrm{erf}(|R - x|)}{R_c|R - x|} \\ & - \frac{Z_1 \mathrm{erf}(|R_1 - y|)}{R_f|R_1 - y|} - \frac{Z_2 \mathrm{erf}(|R_2 - y|)}{R_f|R_2 - y|} - \frac{Z \mathrm{erf}(|R - y|)}{R_c|R - y|} \, . \end{aligned} \tag{6.36}$$

Note that the interactions are screened; The values of the screening are modulated by the parameters R_f (for the interaction electron – fixed ions), R_c (for the interaction electron – moving ion), and R_e (for the electron – electron interaction). By tuning these parameters, the nonadiabatic couplings may be reduced or enhanced [195–199].

The degree of diabaticity is qualitatively pictured in the adiabatic potential energy surfaces (PES) – which show the eigenvalues, parameterized with the nuclear coordinate R, of the electronic equation:

$$\{T(x) + T(y) + V(x,y,R)\}\phi_n^{\sigma\tau}(x,y;R) = V_n^{\sigma\tau}(R)\phi_n^{\sigma\tau}(x,y;R) \, , \tag{6.37}$$

so that $\phi_n^{\sigma\tau}(x,y;R)$ are the electronic eigenfunctions in state n. Two different initial configurations are possible: the two electrons are in the same spin state – corresponding to spatial functions of gerade symmetry –, or in opposite spins – corresponding to ungerade spatial functions. (Note that since the full Hamiltonian does not contain the spin, the system will remain in the same spin configuration during any evolutions). The adiabatic PES are depicted in Fig. 6.52 for the anti-parallel spin (top) and parallel spin (bottom) cases, and for the ground state, and the first three excited states.

In the anti-parallel case, the ground state and the first excited state show an avoided crossing, so we should expect clear nonadiabatic behavior in that region. In the parallel spin case, however, the ground state and the first excited state are well separated from each other and from the higher states, whereas the second and third excited states again show avoided crossings.

The localization functions for this particular model have to be defined. The full time-dependent density matrix is given by:

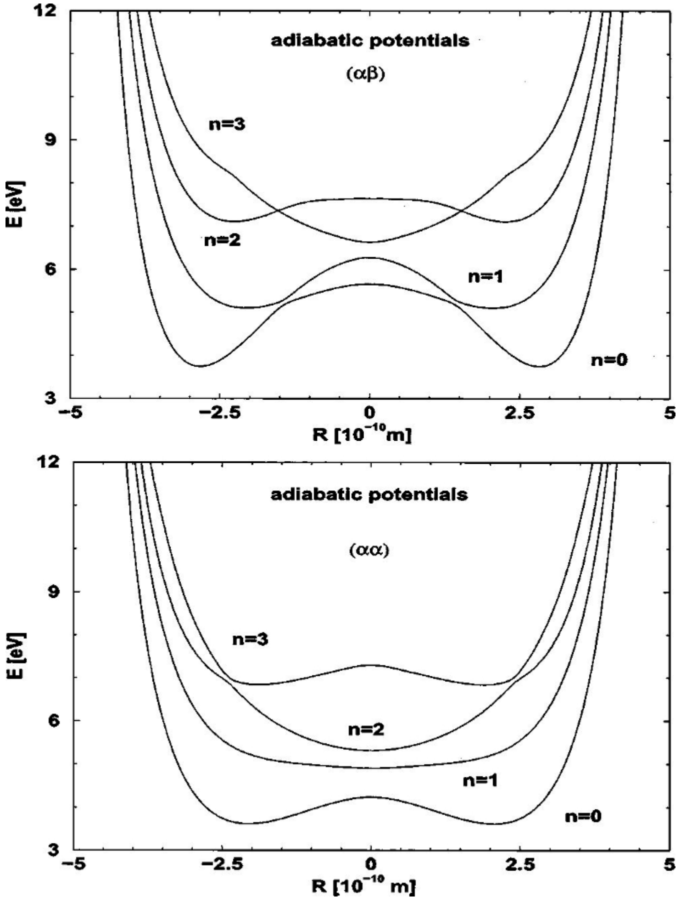

Fig. 6.52. Adiabatic potentials for the anti-parallel (top panel) and parallel spin case (bottom panel). Different parameters were used in the parameterization of the interaction energy: $R_c = R_f = 1.5$ Å; $R_e = 2.5$ Å(left panel), and $R_c = R_f = R_e = 1.5$ Å(right panel).

$$D_{\sigma\tau}(x, y, R; t) = |\Psi(x\sigma, y\tau, R; t)|^2 , \tag{6.38}$$

where Ψ is the full wave function. Integrating out the nuclear degree of freedom, one obtains the density matrix for the two electrons:

$$D_{\sigma\tau}(x, y; t) = \int \mathrm{d}^3 R \, D_{\sigma\tau}(x, y, R; t) , \tag{6.39}$$

and one may then define the conditional pair probability function:

$$P_{\sigma\tau}(x, y; t) = \frac{D_{\sigma\tau}(x, y; t)}{\rho_\sigma(x; t)} , \tag{6.40}$$

where ρ_σ is the electronic one-particle spin-density. Two cases have to be distinguished:

1. Anti-parallel spins: $P_{\alpha\beta}(x,x;t)$ is the conditional probability to find one electron at time t at point x, if we know with certainty that other electron with opposite spin is in the same place. This is an indirect measure of localization. One may define, in analogy to the usual ELF, a time-dependent *anti-parallel spin* electron localization function (TDALF), η^{ap}, as:

$$\eta^{\mathrm{ap}}(x;t) = \frac{1}{1 + |P_{\alpha\beta}(x,x;t)/F_\alpha(x;t)|^2} \,. \tag{6.41}$$

   $F_\alpha(x;t) = (4/3)\pi^2\rho_\alpha^3(x;t)$ is the Thomas-Fermi kinetic energy density for anti-parallel spins and 1D systems.

2. Parallel spins: This would correspond to the usual ELF, presented previously. However, the one-dimensionality of the model changes the derivation since the spherical average is not necessary. Defining $s = x - y$, one may expand $P_{\alpha\alpha}(x,s;t)$ in a Taylor series up to second order around $s = 0$:

$$P_{\alpha\alpha}(x,s;t) = \frac{1}{2}\frac{\partial^2 P_{\alpha\alpha}}{\partial s^2}(x,0;t)s^2 + \mathcal{O}(s^3) \,. \tag{6.42}$$

   The constant term is null due to Pauli's principle, whereas the linear term also vanishes since, according to Kato's cusp theorem [200], the wave function is proportional to s. The s^2 coefficient, $a_{\alpha\alpha}(x;t)$, is now used to define the TDELF with the usual re-normalization precautions:

$$\eta(x;t) = \frac{1}{1 + |a_{\alpha\alpha}(x;t)/F_\alpha(x,t)|^2} \,. \tag{6.43}$$

   In this case, $F_\alpha(x) = (16/3)\pi^2\rho_\alpha^3(x)$.

The nuclear movement is investigated through the time-dependent nuclear density:

$$\Gamma_{\sigma\tau}(R;t) = \int \mathrm{d}^3x \int \mathrm{d}^3y \, D_{\sigma\tau}(x,y,R;t) \,. \tag{6.44}$$

The time-evolution of the system is then initiated from an initial state with the form:

$$\Psi(x\sigma, y\tau, R; t=0) = e^{-\gamma(R-R_0)^2}\phi_n^{\sigma\tau}(x,y;R) \,, \tag{6.45}$$

that is, from the first electronic excited state, and from a Gaussian nuclear distribution around some initial point – in this case, $R_0 = -3.5$ Å.

Once again, two possible spin configurations for the initial state have to be distinguished:

1. Anti-parallel spins.
   This case is shown in Fig. 6.53, left side. The top graph represents the *nuclear* time-dependent density. This density, initially localized around -3.5 Å, travels toward its turning point, while it strongly disperses. Soon,

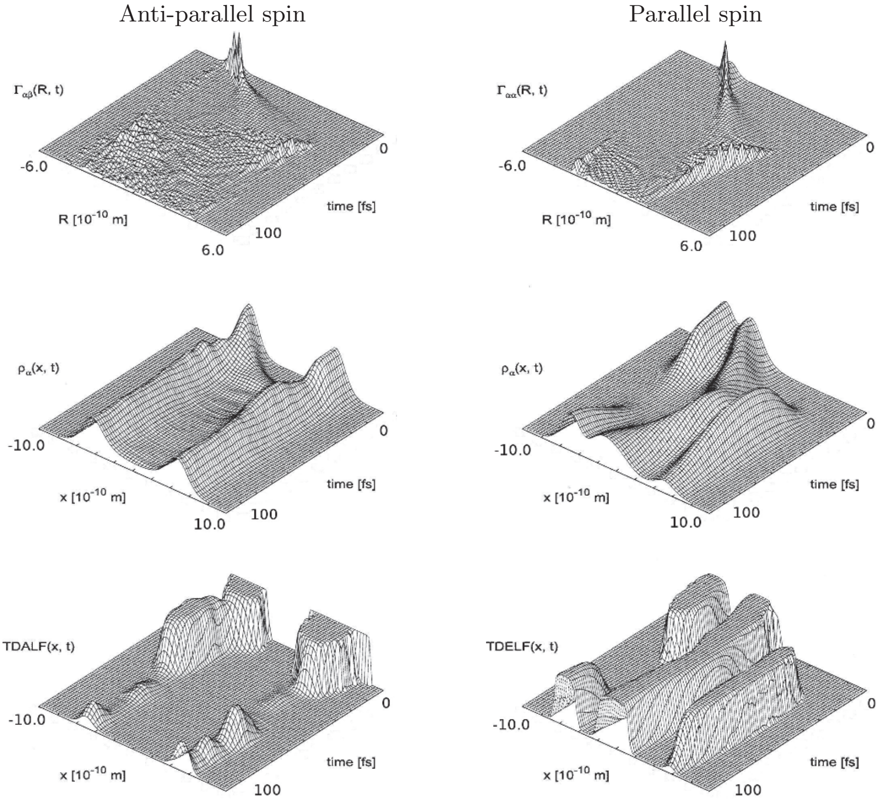

Anti-parallel spin

Parallel spin

Fig. 6.53. Quantum dynamics of the model system presented in Sect. 6.5.4, for the anti-parallel spin (left) and the parallel spin cases (right). The upper panel shows the nuclear density. The time-dependent electron density and TDELF are shown in the middle and lower panels, respectively.

as a consequence of the strong nonadiabatic coupling, the nuclear wave packet becomes extremely broad and a defined structure can no longer be seen.

The electron density (middle panel) seems to be unaware of the nuclear motion. This does not mean that electrons are static; its behavior may be best analyzed by looking at the TDALF (lower panel). We have two localization domains, which correspond also with the initial areas of high density. It may be seen how, as the nucleus transverses this area, the localization amplitude diminishes, and almost vanishes for those two areas. This illustrates how the strong nonadiabatic coupling is effective in decreasing localization.

2. Parallel spins.

   This case is shown in Fig. 6.53, right side. Also, the nuclear time-dependent density is on the top and the time-dependent electron density is in the middle, although in this case it is the usual TDELF (parallel-spins) which is shown in the bottom panel.

   This case has been tailored to avoid the presence of nonadiabatic effects (the first excited state is well separated from the others). As a result, with the chosen initial conditions, the motion takes place exclusively in a single electronic state. The nuclear wave packet is initially localized in the left half of the potential well, and starts moving to the right side where it is repelled by the right side fixed ion at about 40 fs. The wave packet then shows an oscillatory structure, and broadens due to the anharmonicity of the potential.

   The electronic density reflects a charge transfer from the left fixed ion to the right one, with the moving ion acting as an "electron carrier". Initially, there are two maxima in the vicinity of the left fixed ion and on the moving one. After the nucleus crosses the origin, the initial density drops to zero and the new two maxima are on top of the moving ion and on the right side. If the nucleus were not affected by dispersion, the process would reverse with each half-cycle of the nuclear vibration.

   The behavior of the TDELF is now very different with respect to the TDALF in the anti-parallel spin case. The localization remains high at all times, and the transfer of electrons from left to right is clear: Initially there are two localization domains; one around the fixed ion, and another near the origin. As the nuclear movement starts, the first domain vanishes, and a third domain appears near the right fixed ion. After the vibrational period of the nucleus is finished, this third domain disappears, and the initial ELF is however restored. The vanishing of the first domain and the appearance of a third domain indicates that one electron must have been removed from the left fixed nucleus and dragged to the right.

In conclusion, the handful of examples presented in this section illustrate the amount of information that can be gained from the time-dependent ELF in theoretical studies of ultrafast phenomena. One can learn about the time scales of the processes, and/or about how the various sub-events that make up a complex reaction are ordered in time: which bonds break first, which second, how the new links are created, etc. One can observe and interpret intermediate electronic structure that may be short lived but relevant for the overall outcome. This information starts to become available to experimentalists, as the time resolution of the sub-femtosecond laser sources increases.

6.6 Cluster dynamics in ultraintense laser fields

A. Heidenreich, I. Last, and J. Jortner

6.6.1 How intense is ultraintense?

Table-top lasers are currently characterized by a maximal intensity of $\sim 10^{22}$ Wcm^{-2} [201,202], which constitutes the highest light intensity on earth. Such ultrahigh intensity corresponds to an electric field of $\sim 10^{12}$ Vcm^{-1}, a magnetic field of $\sim 10^9$ Gauss and an effective temperature of $\sim 10^8$ K, which exceeds that in the interior of the sun and is comparable to that prevailing in the interior of hot stars. The interaction of ultraintense (peak intensity $I_m = 10^{15}$–10^{20} Wcm^{-2}), ultrafast (temporal length 10–100 fs) laser pulses with matter drives novel ionization phenomena [25,203–251], attosecond electron dynamics [20,154,252,253], the production of high energy particles (i.e., electrons, x-rays, and ions) [9,241,242,245–251,254–268] in atoms, molecules, clusters, plasmas, solids, and liquids. The coupling of macroscopic dense matter with ultraintense laser fields is blurred by the effects of inhomogeneous dense plasma formations, isochoric heating, beam self-focusing and radiative continuum production [269,270]. To circumvent the debris problem from macroscopic solid targets, it is imperative to explore efficient laser energy acquisition and disposal in clusters, which constitute large, finite systems, with a density comparable to that of the solid or liquid condensed phase and with a size that is considerably smaller than the laser wavelength. This section addresses electron and nuclear dynamics driven by ultraintense laser–cluster interaction [9,25,203–251,254–267].

The Rabi frequency for the interaction of an ultraintense laser ($I_m = 10^{20}$ Wcm^{-2}), with an atom or molecule with a transition moment of 1–5 Debye, falls in the range of 2–10 keV. Such high values of the Rabi frequency signal the breakdown of the perturbative quantum electrodynamics approach for the ultraintense laser–atom/molecule interaction. The perturbative quantum dynamic approaches are applicable only for 'ordinary' fields (i.e., $I_m < 10^{12}$ Wcm^{-2}, where the Rabi frequency is lower than ~ 0.1 eV), while for strong laser fields, whose frequency is considerably lower than the atomic/molecular ionization potential, the ionization process can be described as electron removal through an electrostatic barrier in a static electric field. The potential for a q-fold ionized atom (or neutral atom), formed by an electric field of charge $(q+1)$ and an external electric field F, is characterized by a high U_b of the potential barrier [232,243,271]

$$U_b = -2[eF\bar{B}(q+1)]^{1/2} \tag{6.46}$$

where $\bar{B} = 14.4$ eV and eF is given in units of eVÅ^{-1}. The barrier is located at the distance

$$r_b = [\bar{B}(q+1)/eF]^{1/2} \tag{6.47}$$

from the ion center along the electric field direction. When the tunneling through such a barrier is of minor importance [243], as realized for ultraintense laser fields (whose intensity domain will be specified below), a classical barrier suppression ionization (BSI) mechanism can be applied. The BSI of a single ion of charge q is realized when the barrier height, (6.46), is equal, with an opposite sign, to the ionization potential E_I^{q+1} of this ion. The threshold field for inducing ionization is

$$eF = (E_I^{q+1})^2/4\bar{B}(q+1) \tag{6.48}$$

where $F = F_\ell$ is the laser field, with $|eF_\ell| = 2.745 \times 10^{-7} I_m^{1/2}\,\mathrm{eV\AA^{-1}}$, where I_m is given in $\mathrm{Wcm^{-2}}$. The threshold laser intensity for BSI is then given by

$$I_m = 8.295 \times 10^{11} (E_I^{q+1})^4/\bar{B}^2(q+1)^2 \tag{6.49}$$

The barrier distance for the threshold field, (6.47), assumed the form

$$r_b = 2\bar{B}(q+1)/E_I^{q+1} \tag{6.50}$$

The BSI, (6.49), describes multielectron ionization of Xe atoms in the intensity range of $I_m = 10^{15}\,\mathrm{Wcm^{-2}}$ (where Xe^{3+} is produced) up to $I_m = 10^{20}\,\mathrm{Wcm^{-2}}$ (where Xe^{36+} is produced), with the calculated results in the range $I_m = 10^{16}$–$10^{18}\,\mathrm{Wcm^{-2}}$ being in good agreement with the available experimental data [272,273].

To account for tunneling effects in multielectron atomic ionization through the barrier U_b, (6.46), the Amosov–Delone–Krainov (ADK) model [45] gives the ionization probability $W(I(t))$ at the laser intensity $I(t) = I_m \cos^2(2\pi\nu t)$ (where ν is the laser frequency). The peak intensity I_m was determined from the single-cycle averaging $\int_0^{1/\nu} dt W(I(t)) = 1$. In the intensity range $I_m = 10^{15}$–$10^{19}\,\mathrm{Wcm^{-2}}$, the BSI and the ADK results for a single Xe atom agree within 10% and are close to the available experimental data [272, 273]. For lower intensities ($I_m < 10^{15}\,\mathrm{Wcm^{-2}}$), the BSI model is no longer applicable, with the intensity $I_m \geq 10^{15}\,\mathrm{Wcm^{-2}}$ marking the lower limit of the ultraintense laser domain.

The laser driven one-step BSI mechanism for the ionization of a single atom requires a significant extension when applied to cluster ionization. Of considerable interest is the situation when the cluster size characterized by n atomic/molecular constituents and cluster radius $R_0 = r_0 n^{1/3}$ (where r_0 is the constituent radius) significantly exceeds the size of the single constituent barrier distance r_b, (6.50). Under these circumstances a compound cluster ionization mechanism is manifested, which occurs via a sequential-simultaneous inner-outer ionization process [205, 206, 211, 212, 217–219, 231, 243–245]. Electron dynamics triggers nuclear dynamics, with outer ionization being accompanied with and followed by cluster Coulomb explosion (CE), which results in the production of high-energy (keV–MeV) multicharged ions on the (10–500 fs) time scale of nuclear motion.

The realm of ultrafast phenomena in molecular science currently moves from femtosecond dynamics on the time scale of nuclear motion [274–277] toward attosecond electron dynamics [20, 154, 252, 253]. This new attosecond temporal regime for dynamics constitutes a “spin off” of ultraintense laser–matter interactions. In the attosecond domain nonperturbative effects are fundamental and new mechanisms of ionization and of multielectron dynamics in atoms, molecules, clusters, plasmas and condensed matter are unveiled. In this context this section will address the response of clusters to ultraintense laser fields that induces novel ionization processes and manifests new features of electron dynamics [211, 222, 238–244, 267, 278–281], which drives nuclear dynamics of CE [224, 228, 245–251, 254–256, 259].

6.6.2 Extreme cluster multielectron ionization

The cluster response to ultraintense laser fields triggers well-characterized ultrafast electron dynamics (on the time scale of $< 1\,\mathrm{fs}$–$100\,\mathrm{fs}$). The compound, extreme multielectron ionization mechanism of clusters involves three sequential-parallel processes of inner ionization, nanoplasma formation and outer ionization. Inner ionization results in the formation of a charged, energetic nanoplasma within the cluster or in its vicinity, which is followed by the partial or complete outer ionization of the nanoplasma. Extreme multielectron ionization of elemental and molecular clusters, e.g., Ar_n [203, 207, 234–236], Xe_n [25,216,223,231,233], $(\mathrm{H}_2)_n$ [237], $(\mathrm{D}_2)_n$ [221,254,257], $(\mathrm{H}_2\mathrm{O})_n$ [230,234], $(\mathrm{D}_2\mathrm{O})_n$ [224,230,234], $(\mathrm{CH}_4)_n$ [226], $(\mathrm{CD}_4)_n$ [213,226,259], and $(\mathrm{HI})_n$ [9,258, 260], in ultraintense laser fields leads to the production of highly charged ions. These involve the stripping of the valence electrons, or even all the electrons from light first-row atoms, e.g., H^+ and D^+ [208,211,221,226,244,261], O^{q+} ($q = 6$–8) [211,224,241], C^{q+} ($q = 4$–6) [213,221,226,230,242,246,262], as well as the production of highly charged heavy ions, e.g., Xe^{q+} ($q = 3$–26) [216,217,223,239–244,246,257,261,265,278,279,282,283]. These unique inner/outer ionization processes and nanoplasma dynamics and response driven by ultraintense laser–cluster interactions were explored by theoretical models and by computer simulations.

The laser electric field acting on the elemental or molecular cluster is taken as $F_\ell(t) = F_{\ell 0}(t)\cos(2\pi\nu t)$, where ν is the laser frequency and $F_{\ell 0}(t)$ is the pulse envelope function. Molecular dynamics simulations (including magnetic field and relativistic effects) and analyses of high-energy electron dynamics and nuclear dynamics in a cluster interacting with a Gaussian laser field $F_{\ell 0}(t) = F_m \exp[-2.773(t/\tau)^2]$, F_m being the electric field at the pulse peak. The infrared laser parameters used for the simulations reported in this section are $\nu = 0.35\,\mathrm{fs}^{-1}$ (photon energy $1.44\,\mathrm{eV}$ and pulse temporal width (FWHM) $\tau = 10$–$100\,\mathrm{fs}$) [238, 243, 279]. The laser pulse is defined in the time domain $t \geq -\infty$ and the peak of the laser pulse is attained at $t = 0$. An initially truncated laser pulse was used for the simulations, with the initial laser field (corresponding to the threshold of single electron/molecule ionization in the cluster) being located at the (negative) time $t = t_s$, which is laser intensity and pulse width dependent [243, 279]. The end of the pulse was taken at $t = -t_s$ [279]. The simulations of electron dynamics [238, 243–246, 279] elucidated the time dependence of inner ionization, the formation, persistence and decay of the nanoplasma, and of outer ionization.

The cluster inner ionization is driven by two processes:

(A) The BSI mechanism, which is induced by a composite field $\boldsymbol{F} = \boldsymbol{F}_\ell + \boldsymbol{F}_i$, where $\boldsymbol{F}_i$ is the inner field generated by electrostatic interactions with the ions (ignition effects) [210, 243] and with the nanoplasma electrons (screening effects) [243, 282]. The BSI level and time-resolved dynamics were evaluated from (6.48) for the threshold composite field [243, 279].

(B) Electron impact ionization (EII), which involves inelastic, reactive impact ionization of ions by the nanoplasma electrons [223, 243, 278, 283]. EII in Xe_n clusters was explored using experimental data [284–288] for the energy dependence of ionization cross sections of Xe^{q+} ions ($q = 1$–10), which were fit by a three-parameter Lotz-type equation [289]. The proper parameterization [278, 279] of the EII cross sections led to reliable information on the EII ionization levels and their relative contribution to inner ionization and to the nanoplasma populations. At the lower intensity domain of $I_m = 10^{15}$–$10^{16}\,\mathrm{Wcm}^{-2}$, the EII contribution to the inner ionization yield is substantial ($\simeq 40\%$ for Xe_{2171} at $\tau = 25\,\mathrm{fs}$), increases with increasing the cluster size and manifests a marked increase with increasing the pulse length [279]. The EII yield and the EII level enhancement markedly decrease with increasing the laser intensity. The EII involves reactive dynamics of nanoplasma electrons driven by the laser field, and will be further considered in Sect. 6.6.3.

Elemental Xe_n clusters provide benchmark systems for the theoretical and experimental studies of electron and nuclear dynamics. A Xe_{2171} cluster coupled to Gaussian laser pulses ($\tau = 25\,\mathrm{fs}$) of intensities $I_m = 10^{15}\,\mathrm{Wcm}^{-1}$ (Fig. 6.54) and $I_m = 10^{18}\,\mathrm{Wcm}^{-2}$ (Fig. 6.55) reveals the following dynamic processes:

A. Electron dynamics involving sequential–parallel multielectron inner ionization (represented by the color coding of atom charges in Figs. 6.54 and 6.55), nanoplasma formation (represented by the electron cloud and by the positive ions in Figs. 6.54 and 6.55), and outer ionization (which corresponds to complete depletion of the nanoplasma for $I_m = 10^{18}\,\mathrm{Wcm}^{-2}$, Fig. 6.55).

B. Nuclear dynamics of CE, which is spatially nonuniform and relatively slow ($\sim 120\,\mathrm{fs}$) for $I_m = 10^{15}\,\mathrm{Wcm}^{-2}$ (where complete outer ionization does not prevail).

The extreme ionization level of Xe_n clusters results in the production of $(\mathrm{Xe}^{q+})_n$ multicharged ions (characterized by an average charge q_{av} on each ion). The cluster size and laser intensity dependence of q_{av} produced from

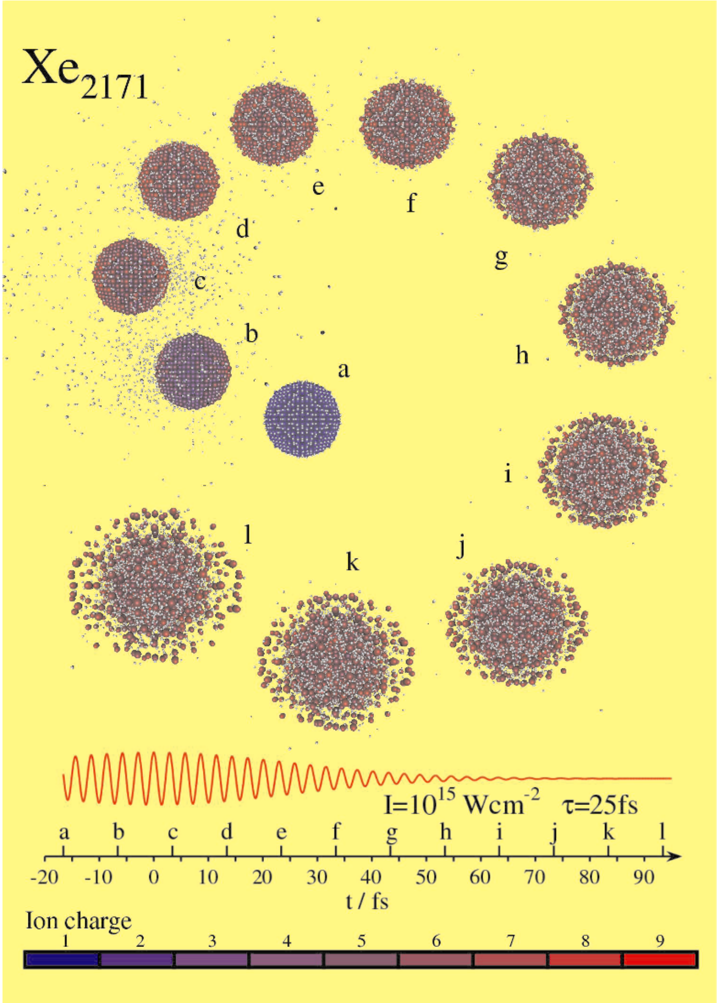

Fig. 6.54. Snapshots of the time-resolved inner ionization, nanoplasma charge distribution, outer ionization and structures of Xe_{2171} clusters induced by Gaussian laser pulses with a peak intensity of $\mathrm{I}_M = 10^{15}\,\mathrm{Wcm}^{-2}$ and a pulse width of $\tau = 25\,\mathrm{fs}$. The lower part of the panel portrays the electric field of the laser and the time axis $t - t_s$ (where t_s is the onset time for the laser field [85]). The snapshot instants are marked a–l on the time axes. The Xe ions are color coded according to their charge: blue corresponds to the initial charge +1 and red to the maximum charge +9, which can be obtained at this intensity (and τ). A map of the color coding of the ionic charges is given in the panel at the bottom of the figure. The electrons are represented by light gray spheres.

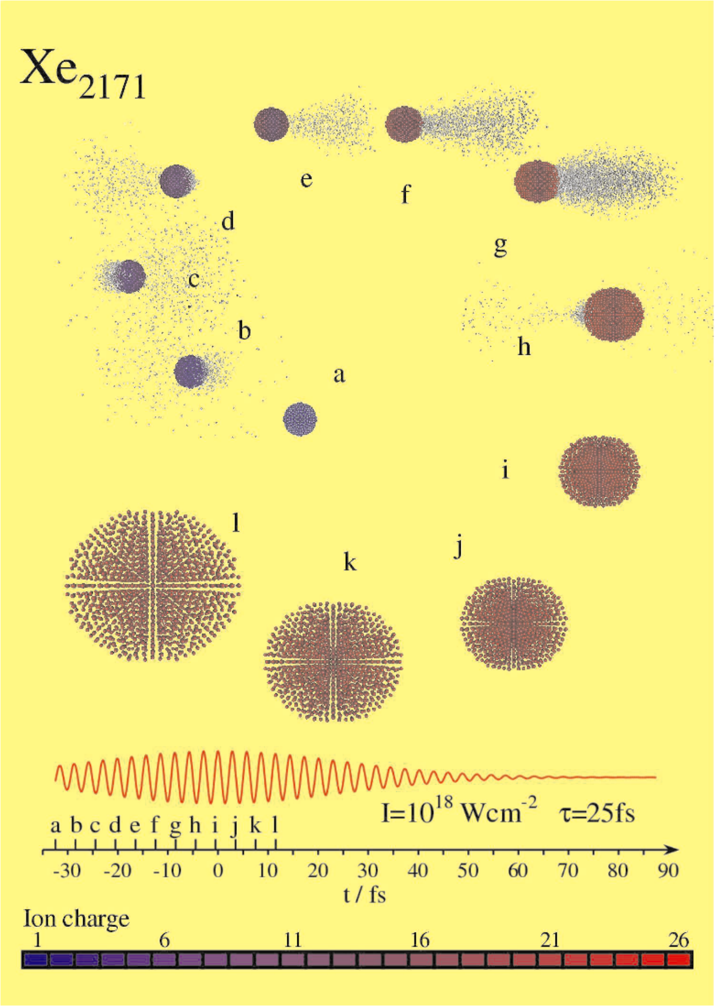

Fig. 6.55. Snapshots of the time-resolved inner ionization, nanoplasma charge distribution, outer ionization and structures induced by a Gaussian laser pulse with a peak intensity of $I_m = 10^{18}\,\mathrm{Wcm}^{-2}$ and a pulse width of $\tau = 25\,\mathrm{fs}$. Presentation and notation as in Fig. 6.54, with the color coding of the Xe ions from blue for the initial charge +1 to deep red for the maximal charge +26.

$n = 55$–2171 clusters (Fig. 6.56) exhibits the formation of highly charged ($q_{av} = 6$–36) clusters. For any cluster size, q_{av} increases with increasing I_m, essentially manifesting the contribution of the laser field to the BSI. The cluster size dependence at fixed I_m exhibits an intensity specific behavior. The highest intensity domains, $q_{av} = 26$ at $I_m = 10^{19}\,\mathrm{Wcm}^{-2}$ (corresponding to ionization of the $4s^2 4p^6 4d^{10} 5s^2 5p^6$ shells) and $q_{av} = 36$ at $I_m = 10^{20}\,\mathrm{Wcm}^{-2}$ (corresponding to the ionization of the $3d^{10} 4s^2 4p^6 4d^{10} 5s^2 5p^6$ shells), are independent of the cluster size at fixed I_m. For $I_m = 10^{18}\,\mathrm{Wcm}^{-2}$, q_{av} increases with increasing R_0, achieving the value of $q_{av} = 24$ at $n = 2171$, which presumably manifests ignition effects. For $I_m = 10^{17}\,\mathrm{Wcm}^{-2}$, q_{av} first increases (in the range $n = 55$–459), and subsequently decreases (in the range $n = 459$–2171) with increasing R_0 (and n), apparently manifesting the interplay between ignition effects (lower n) and screening effects (higher n). In the lowest intensity range of $I_m = 10^{15}\,\mathrm{Wcm}^{-2}$ $q_{av} = 5.8$–6.8, while at $I_m = 10^{16}\,\mathrm{Wcm}^{-2}$ $q_{av} = 8$, with q_{av} being nearly cluster size independent. In the intensity range of $I_m = 10^{18}$–$10^{20}\,\mathrm{Wcm}^{-2}$, q_{av} converges for clusters to the single atom–value with decreasing R_0, indicating that ignition effects are minor for moderately small $n = 55$ clusters in this highest I_m range. At $I_m = 10^{16}$–$10^{17}\,\mathrm{Wcm}^{-2}$, the values of q_{av} for Xe_{55} are somewhat larger (by 0.5–1.0 electrons per atom) than the single-atom values. A dramatic enhancement of q_{av} for Xe_{55} at $I_m = 10^{15}\,\mathrm{Wcm}^{-2}$ is exhibited, where q_{av} increases by a numerical factor of 2 relative to the single–atom value.

The inner ionization level $n_{ii}^L = q_{av}$ (per constituent with the indexsubject L representing an asymptotic long-time value) is $n_{ii}^L = n_{BSI}^L + n_{imp}^L$ being given by the sum of the BSI contribution n_{BSI}^L and the EII contribution n_{imp}^L. From the simulation data for n_{ii}^L, n_{BSI}^L and n_{imp}^L (Fig. 6.57), complete information emerges concerning the interplay between the contributions of BSI, and ignition and screening, together with the contribution of EII to inner ionization, which reveals the following features: (1) Ignition effects on n_{BSI}^L for very small Xe_n clusters ($n = 2$–13) are manifested at the lowest intensity of $I_m = 10^{15}\,\mathrm{Wcm}^{-2}$ (Fig. 6.57a), where the inner field is comparable to the laser field. This ignition effect for $n = 2$–13 is not operative at $I_m \geq 10^{16}\,\mathrm{Wcm}^{-2}$ (Figs. 6.57b–d), where the laser field overwhelms the inner field. (2) Ignition effects for large clusters ($n > 55$), manifested by the increase of q_{av} with increasing n, are exhibited in the higher intensity domain $I_m = 10^{17}$–$10^{18}\,\mathrm{Wcm}^{-2}$ (Figs. 6.57c and 6.57d). (3) Screening effects, manifested by the decrease of n_{BSI}^L with increasing n, are exhibited at $I_m = 10^{15}$–$10^{16}\,\mathrm{Wcm}^{-2}$ for $n \geq 13$ (Figs. 6.57a and 6.57b) and for $n = 459$–2171 at $I_m = 10^{17}\,\mathrm{Wcm}^{-2}$ (Fig. 6.57c). At $I_m = 10^{18}\,\mathrm{Wcm}^{-2}$ (Fig. 6.57d) screening effects are not operative. (4) The EII contribution of n_{imp}^L to $n_{ii}^L = q_{av}$ at fixed I_m increases with increasing n for large clusters in the intensity range $I_m = 10^{15}$–$10^{18}\,\mathrm{Wcm}^{-2}$ (Figs. 6.57a–d). This significant issue will be further discussed in Sect. 6.6.3. (5) The maximal ionic charge q_{max} (Figs. 6.57a–d) exceeds the average charge, i.e., $q_{max} > n_{ii}^L = q_{av}$. For $I_m = 10^{15}\,\mathrm{Wcm}^{-2}$, a flattening at $q_{max} = 8$ is ex-

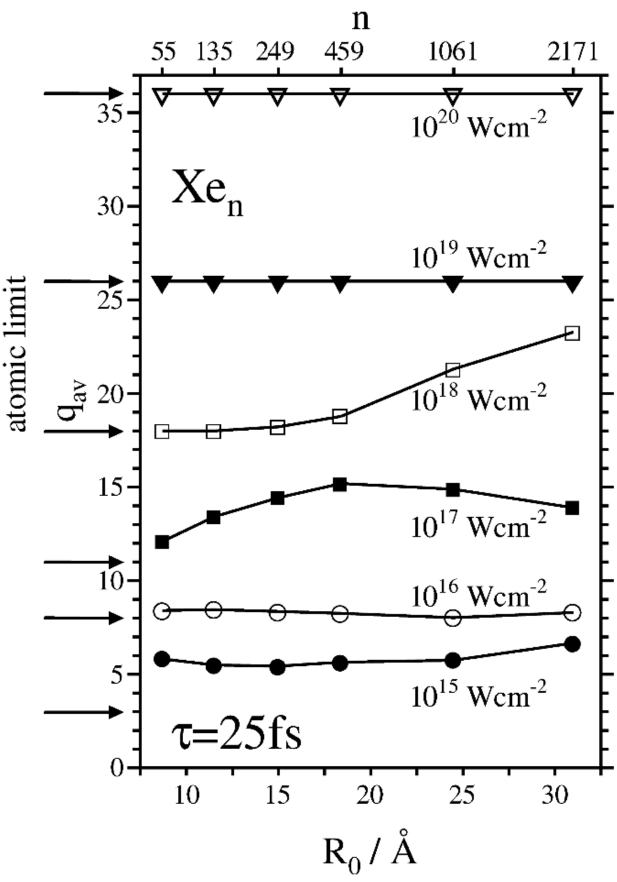

Fig. 6.56. Cluster size and laser intensity dependence of inner ionization levels (expressed by the average final charge $q_{av} = n_{ii}^{L}$ of the $(\mathrm{Xe}^{q+})_n$ ions) of Xe$_n$ clusters ($n = 55$–2171) over the intensity range $I_m = 10^{15}$–$10^{20}\,\mathrm{Wcm}^{-2}$ (marked on the curves) with a laser pulse width of $\tau = 25\,\mathrm{fs}$. The horizontal arrows (marked atomic limit) represents the single atom ionization level calculated by the BSI model [228].

hibited over a broad size domain, followed by EII at $n = 2171$ (Fig. 6.57a), while for $I_m = 10^{17}\,\mathrm{Wcm}^{-2}$ a flattening at $q_{max} = 18$ is observed (Fig. 6.57c). (6) 'Magic numbers' in cluster multielectron ionization are observed in the cluster size domain where laser induced BSI dominates over ignition, screening and EII. The 'magic numbers' are $q_{av} = 8$ at $I_m = 10^{16}\,\mathrm{Wcm}^{-2}$ for $n = 2$–55 (Fig. 6.57b) corresponding to the ionization of the $5\mathrm{s}^2 5\mathrm{p}^6$ shells, $q_{av} = 18$ at $I_m = 10^{18}\,\mathrm{Wcm}^{-2}$ for $n = 2$–135 (Fig. 6.57d) corresponding to the ionization of the $4\mathrm{d}^{10} 5\mathrm{s}^2 5\mathrm{p}^6$ shells, $q_{av} = 26$ at $I_m = 10^{19}\,\mathrm{Wcm}^{-2}$ for $n = 55$–2171 (Fig. 6.56) corresponding to the ionization of the $4\mathrm{s}^2 4\mathrm{p}^6 4\mathrm{d}^{10} 5\mathrm{s}^2 5\mathrm{p}^6$ shells, and

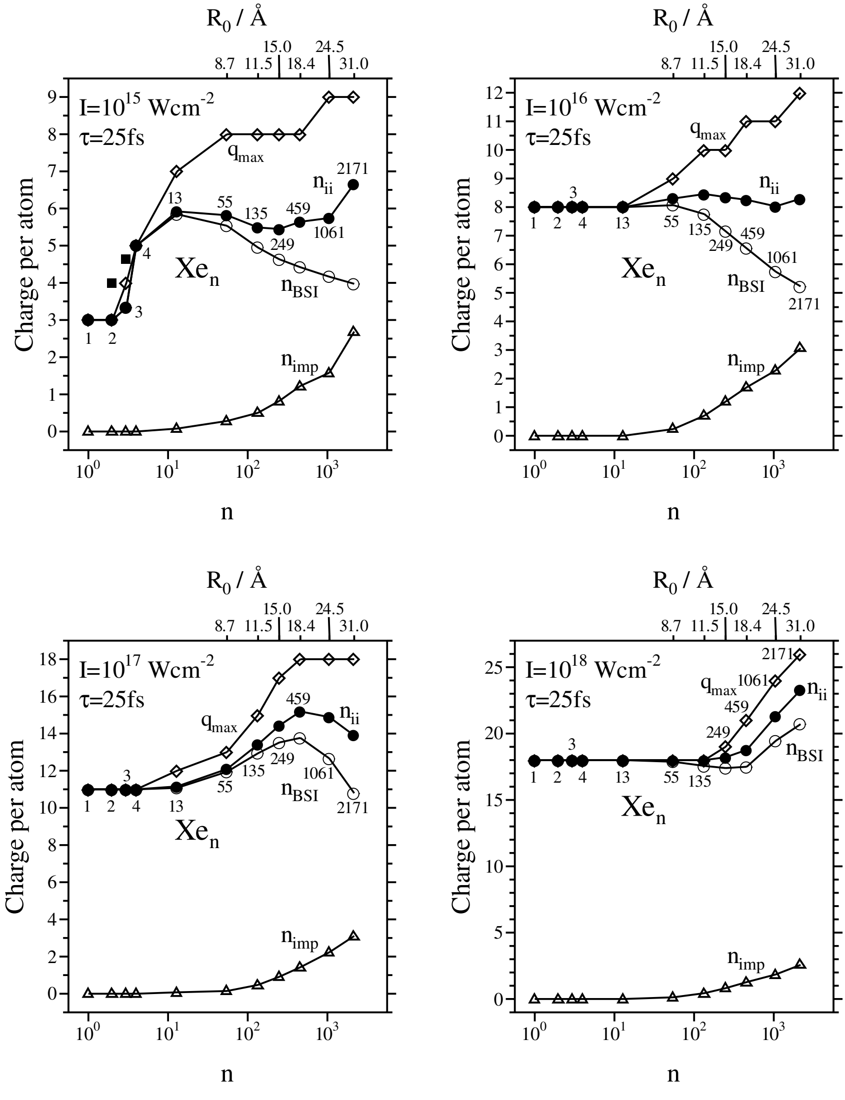

Fig. 6.57. The cluster size dependence of the long-time BSI level n^L_{BSI} (O), the EII level n^L_{imp} (Δ), and the total inner ionization level n^L_{ii} (● and ■) for the maximal ionic charge $q_{\max}$ (◇) from Xe$_n$ (n = 2–2171) clusters. (a) $I_m = 10^{15}\,\mathrm{Wcm}^{-2}$ (τ = 25 fs). The $n^L_{BSI} = n^L_{ii}$ data for small (n = 2 and 3) clusters at a fixed nuclear configuration are dependent on the direction of the laser field, with (■) for the laser field being parallel to the molecular axis and (●) for the laser field being perpendicular to the molecular axis. (b) $I_m = 10^{16}\,\mathrm{Wcm}^{-2}$ (τ = 25 fs). (c) $I_m = 10^{17}\,\mathrm{Wcm}^{-2}$ (τ = 25 fs). (d) $I_m = 10^{18}\,\mathrm{Wcm}^{-2}$ (τ = 25 fs).

$q_{av} = 36$ at $I_m = 10^{20}\,\mathrm{Wcm}^{-2}$ for $n = 55$–2171 (Fig. 6.56) corresponding to the ionization of the $3\mathrm{d}^{10}4\mathrm{s}^2 4\mathrm{p}^6 4\mathrm{d}^{10} 5\mathrm{s}^2 5\mathrm{p}^6$ shells.

The cluster size, laser intensity, and laser pulse shape dependence of inner ionization levels of Xe_n clusters are induced by a complex superposition of laser-induced BSI, inner field ignition effects and nanoplasma screening effects, as well as by the contribution of EII. The inner field ignition and screening effects, in conjunction with EII, constitute collective effects, which preclude the description of cluster inner ionization in terms of an additive contribution of the constituents. The laser intensity dependent ionization levels of Xe_n clusters, with the dramatic enhancement of q_{av} and q_{max} with increasing I_m, originate from the laser field contribution to the BSI. This enhancement is characteristic for partial multielectron inner ionization of heavy atoms, with no production of nuclei in the currently available laser intensity domain ($I_m \leq 10^{21}\,\mathrm{Wcm}^{-2}$). On the other hand, for $(\mathrm{H}_2)_n$ and $(\mathrm{D}_2)_n$ clusters, complete ionization can be achieved at $I_m \simeq 2 \times 10^{14}\,\mathrm{Wcm}^{-2}$ [221, 243], which is below the lowest limits of the intensity range used herein. For first-row molecular heteroclusters consisting of light atoms, e.g., $(\mathrm{CA}_4)_n$, $(\mathrm{A}_2\mathrm{O})_n$ (A = H, D), complete multielectron ionization, with the production of H^+, D^+, C^{6+} and O^{8+} nuclei, can be realized in the currently available laser intensity domain.

Table 6.1. Multielectron ionization of Xe_n clusters

EXPERIMENT						THEORY				
	n (R_0)	I_m Wcm^{-2}	τ fs	q_{av}	$q_{\max}$	n (R_0)	I_m Wcm^{-2}	τ fs	q_{av}	$q_{\max}$
(a) [280]	2×10^6 (270 Å)	5×10^{17}			25	2171 (31 Å)	10^{18}	25	23	25
(b) [281]	5×10^4 (79 Å)	2×10^{17}	20	12	18	2171 (31 Å)	10^{17}	25	14	18
(c) [267]	10^5–10^6 (100 Å–210 Å)	10^{18}			26–30	2171 (31 Å)	10^{18}	25	23	26
(d) [222]	1.2×10^4 (49 Å)	10^{15}	100		11	2171 (31 Å)	10^{15}	100		10

In Table 6.1 the ionization levels are compared for the largest Xe_n ($n = 2171$) cluster sizes calculated by us with the available experimental results [222, 267, 280, 281]. The experimental values of q_{av} and q_{max} at $I_m = 2 \times 10^{17}\,\mathrm{Wcm}^{-2}$ [data set (b)] [281] and at $I_m = 10^{15}\,\mathrm{Wcm}^{-2}$ [data set (d)] [222] are in good agreement with experiment. For the experimental results of $I_m = 5 \times 10^{17}\,\mathrm{Wcm}^{-2}$ [data set (a)] [280] and $I_m = 10^{18}\,\mathrm{Wcm}^{-2}$ [data set (c)] [267], the experimental cluster radius $R_0 = r_0 n^{1/3}$ ($r_0 = 2.16\,\text{Å}$ being the constituent radius) is considerably larger than the corresponding

R_0 values used for the simulations. However, the relevant cluster size domain at this high intensity of $I_m = 10^{18}\,\mathrm{Wcm}^{-2}$ is determined by the border radius [245, 246, 279] $R_0^{(I)}$ for the complete sweeping of the nanoplasma from the cluster and for cluster vertical ionization, which prevails for $R_0 \leq R_0^{(I)}$ (see Sect. 6.6.4). For $R_0 > R_0^{(I)}$ the inner ionization levels are weakly cluster size dependent. For Xe_n, in the intensity range of $I_m = 10^{18}\,\mathrm{Wcm}^{-2}$, $R_0^{(I)} = 35 \pm 5\,\text{Å}$ [279]. Thus the experimental data (a) and (c) correspond to $R_0 \gg R_0^{(I)}$, while the simulation data correspond to $R_0 \leq R_0^{(I)}$, allowing for an approximate comparison between theory and experiment. The computational results reported in this section account for the gross features of the cluster ionization levels.

6.6.3 The nanoplasma

The nanoplasma is formed from the unbound electrons, which are confined to the cluster and to its vicinity, and from the ion cluster. The life story of the nanoplasma is portrayed in Figs. 6.54 and 6.55 for Xe_{2171} clusters and in Fig. 6.58 for $(\mathrm{D}_2)_{2171}$ and $(\mathrm{HT})_{2171}$ clusters. These snapshots portray the formation of the nanoplasma, its response to the laser field, followed by its complete depletion at $I_m = 10^{18}\,\mathrm{Wcm}^{-2}$ (Figs. 6.55 and 6.58) or its partial depletion at $I_m = 10^{15}\,\mathrm{Wcm}^{-2}$ (Fig. 6.54). The time-dependent nanoplasma population is characterized by the number $n_p(t)$ of nanoplasma electrons (per atomic constituent), which is given by $n_p(t) = n_{ii}(t) - n_{oi}(t)$. The number $n_{ii}(t)$ ($n_{oi}(t)$) of depleted electrons (per constituent) for inner (outer) ionization exhibits a gradual increase and long-time saturation [244, 279]. At long times, after the termination of the laser pulse, the nanoplasma population is finite at lower intensities of $I_m = 10^{15}$–$10^{16}\,\mathrm{Wcm}^{-2}$, exhibiting only partial depletion (Fig. 6.59), with the long-time population n_p^L manifesting a marked increase with increasing the pulse length. The cluster size and laser parameters in Fig. 6.59 provide the conditions for effective reactive dynamics of the nanoplasma [244, 279].

The electron dynamics of the nanoplasma (Figs. 6.54, 6.55 and 6.58–6.60) reveals the following features:

1. Composition of the nanoplasma. It consists of the electron cloud and of the positive Xe^{q+} ions produced by inner ionization. The nanoplasma responds to the laser field, which strips electrons from the cluster by outer ionization. Accordingly, the nanoplasma is positively charged.
2. Formation time. The time scales for the near completion of inner ionization decrease with increasing I_m, assuming the approximate values of $t - t_s \sim 35\,\mathrm{fs}$ at $I_m = 10^{15}\,\mathrm{Wcm}^{-2}$, down to $t - t_s \sim 15\,\mathrm{fs}$ for $I_m = 10^{19}\,\mathrm{Wcm}^{-2}$ for Xe_{2171}.
3. Electron energies. The electron cloud is characterized by high (average) energies $\mathcal{E}$. For Xe_{2171} we found $\mathcal{E} = 53\,\mathrm{eV}$, $150\,\mathrm{eV}$, $930\,\mathrm{eV}$, $72\,\mathrm{keV}$ and $100\,\mathrm{keV}$ at $I_m = 10^{15}$, 10^{16}, 10^{17}, 10^{18}, and $10^{19}\,\mathrm{Wcm}^{-2}$, respectively. The

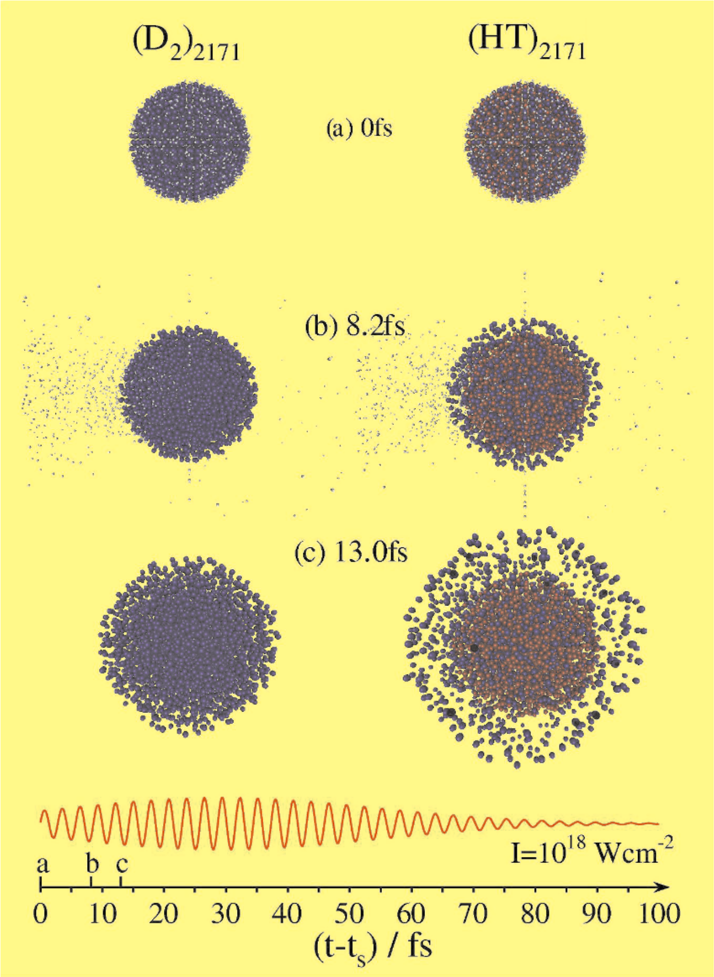

Fig. 6.58. Snapshots of the time-resolved structures of $(D_2)_{2171}$ and $(HT)_{2171}$ clusters in a Gaussian laser field ($I_m = 10^{18}\,\mathrm{Wcm}^{-2}$ at $\tau = 25\,\mathrm{fs}$ marked on the images), at three different times $t - t_s$. The lowest part of the panel portrays the time axis and the electric field of the laser. The instants of the snapshots are marked on the time axis by a, b and c. H atoms are represented in blue, T atoms in red, and electrons in light gray. (a) The initial nanoplasma at $t - t_s = 0$. (b) At $t - t_s = 8.2\,\mathrm{fs}$, the beginning of spatial expansion of the clusters is manifested. In case of the $(HT)_n$ cluster, a shell of H^+ ions is displayed. At this time, a large number of electrons is stripped by outer ionization, which occurs repeatedly when the electric field of the laser is close to a maximum. (c) At $t - t_s = 13.2\,\mathrm{fs}$, the spatial expansion and shell formation of the HT cluster is pronounced. Also, all nanoplasma electrons have been removed at this time.

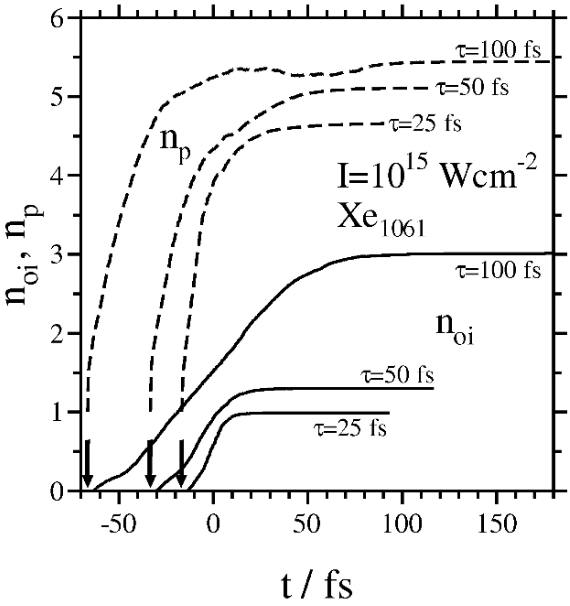

Fig. 6.59. The time dependence of the nanoplasma population $n_p(t) = n_{ii}(t) - n_o(t)$ (dashed lines) and the outer ionization levels n_{oi} (solid lines) for Xe_n clusters ($n = 1061$) at $I_m = 10^{15}\,\mathrm{Wcm}^{-2}$. The laser pulse lengths are $\tau = 25\,\mathrm{fs}$, $50\,\mathrm{fs}$, and $100\,\mathrm{fs}$, as marked on the curves. The vertical arrows represent the times for the onset of the pulse ($t = t_s$).

electron energies increase by 4 orders of magnitude with increasing I_m in this intensity domain.

4. Spatial inhomogeneity and angular anisotropy of the nanoplasma. For $I_m = 10^{15}\,\mathrm{Wcm}^{-2}$ the electron cloud is nearly spatially isotropic, with the majority of the electrons being located within the cluster. For higher intensities of $I_m = 10^{18}\,\mathrm{Wcm}^{-2}$ and $I_m = 10^{19}\,\mathrm{Wcm}^{-2}$, the electron angular distribution is spatially anisotropic, assuming a “sausage type” shape along the laser electric field direction.
5. Attosecond response of the nanoplasma. At intensities of $I_m = 10^{18}$–$10^{19}\,\mathrm{Wcm}^{-2}$ the “sausage type” shape of the electron cloud oscillates along the electric field direction on the time scale ν^{-1} of the laser period, manifesting ultrafast electron dynamics.
6. The outer ionization of the nanoplasma can be either partial (at intensities of 10^{15}–$10^{16}\,\mathrm{Wcm}^{-2}$) or complete (at highest intensities of 10^{18}–$10^{20}\,\mathrm{Wcm}^{-2}$).
7. Persistent and transient nanoplasmas. At intensities of $I_m = 10^{15}$–$10^{16}\,\mathrm{Wcm}^{-2}$, where outer ionization is partial, a persistent nanoplasma on the time scale of $t - t_s > 100\,\mathrm{fs}$ exists, while for higher intensities of

$I_m = 10^{18}$–$10^{19}\,\mathrm{Wcm}^{-2}$, a transient nanoplasma is formed, being completely depleted on the time scale of $t - t_s \simeq 15$–25 fs. The persistent nanoplasma exists over the cluster size domain and intensity range for which $R_0 > R_0^{(I)}$, while the transient nanoplasma prevails for $R_0 < R_0^{(I)}$.

8. The 'metallic' nanoplasma. The average time-dependent electron density in the nanoplasma is

$$\rho_e(t) = n\,n_p(t)/(4\pi/3)R(t)^3 \tag{6.51}$$

where $R(t)$ is the cluster radius, with $R(0) = R_0$ at the onset of the pulse and $R(t) > R_0$ at longer times, due to CE. For the entire I_m range $\rho_e(t)$ first increases with increasing t, reaching a maximum of $\rho_e^{MAX} = 0.08$–$0.09\,\text{Å}^{-3}$ (Fig. 6.60). The weak dependence of ρ_e^{MAX} on I_m (Fig. 6.60) can be traced to the weak intensity dependence of the maximal value of $n_p(t)$, both for the persistent and for the transient nanoplasma. At $I_m = 10^{18}\,\mathrm{Wcm}^{-2}$ $\rho_e(t)$ vanishes for $t \geq 0$, as appropriate for a transient nanoplasma. For the lowest intensity of $I_m = 10^{15}\,\mathrm{Wcm}^{-2}$, $\rho_e(t)$ decreases gradually with increasing t on the time scale of 10–90 fs, due to Coulomb explosion, retaining a long-time ($t_L = 90\,\mathrm{fs}$) electron density of $\rho_e^L = 0.02\,\text{Å}^{-3}$ for Xe_{2171}. The nanoplasma electron densities at the maximum, i.e., $\rho_e^{MAX} = 8 \times 10^{22}$–$9 \times 10^{22}\,\mathrm{cm}^{-3}$ for the entire I_m domain, and the long–time electron density of $\rho_e^L = 2 \times 10^{22}\,\mathrm{cm}^{-3}$ at $I_m = 10^{15}\,\mathrm{Wcm}^{-2}$, are comparable to electron densities in metals.

   It is instructive to establish contact between the microscopic nanoplasma model used herein and a macroscopic 'plasma model' for the nanoplasma response and outer ionization, considering the enhancement of light absorption by resonance effects. The frequency of the linear oscillations for a thermally equilibrated and uniform nanoplasma is [203, 290]

$$\omega_p = (4\pi e^2 \rho_e/3m_e)^{1/2} \tag{6.52}$$

   The maximal (nearly intensity independent) electron density in the nanoplasma is $\rho_e^{MAX} = 0.08$–$0.09\,\text{Å}^{-3}$ (at $I_m = 10^{15}$–$10^{19}\,\mathrm{Wcm}^{-2}$, $\tau = 25\,\mathrm{fs}$, Fig. 6.60). The nanoplasma energy is $\hbar\omega_p = 6.1$–$6.4\,\mathrm{eV}$. This value of $\hbar\omega_p$ is considerably larger than the photon energy of 1.44 eV. The simulation results for the persistent nanoplasma at $I_m = 10^{15}$–$10^{16}\,\mathrm{Wcm}^{-2}$ over the time scale of 100 fs (Fig. 6.59) do not reveal any steep temporal decrease of $n_p(t)$ or an increase of the electron energy, which could be interpreted as resonance generation of nanoplasma oscillations, precluding the possibility of such excitations. The role of the macroscopic 'plasma model' [212, 233] is not borne out by the simulations.

9. Attosecond oscillations of the nanoplasma population. In the intensity range $I_m = 10^{17}$–$10^{18}\,\mathrm{Wcm}^{-2}$ $\rho_e(t)$ exhibits an oscillatory time dependence during the temporal rise of the inner/outer ionization levels (Fig. 6.60). The period of these temporal oscillations is close to the laser period ν^{-1}, manifesting the attosecond response and driving of outer ionization by the ultraintense laser field.

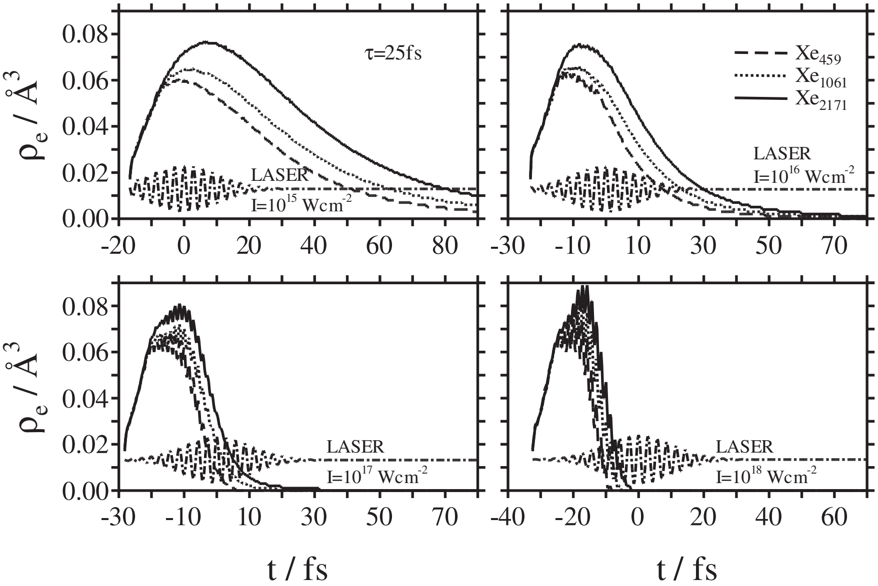

Fig. 6.60. The time dependent electron density in the nanoplasma $\rho_e^{(t)} = n_p^{(t)}/(4\pi/3)R^3$ in Xe_n clusters ($n = 459$, 1061 and 2171, as marked on the curves). R is the cluster radius obtained from molecular dynamics simulations of CE. Data are presented for $I_m = 10^{15}$, 10^{16}, 10^{17}, and $10^{18}\,\mathrm{Wcm}^{-2}$, as marked on the panels. The Gaussian laser fields ($- \cdot - \cdot -$), expressed in arbitrary units for $t \geq t_s$, are presented on the panels.

The reactive dynamics of the nanoplasma is manifested by EII, which is important for clusters of heavy multielectron atoms or molecules, e.g., Xe_n, where the corresponding cross sections are large [278,279,284–288]. The cluster size dependence of n_{imp}^L (at fixed I_m) reveals an increase with increasing n, with the largest EII yields being exhibited at $I_m = 10^{15}$–$10^{16}\,\mathrm{Wcm}^{-2}$, where the persistent nanoplasma prevails (Fig. 6.61). Significantly, in the persistent nanoplasma domain (at $I_m = 10^{15}$ –$10^{16}\,\mathrm{Wcm}^{-2}$), the EII yields and the total ionization levels manifest a marked increase with increasing the laser pulse width. As is evident from the data for Xe_{2171} at $I_m = 10^{15}\,\mathrm{Wcm}^{-2}$ and $\tau =$ 10–100 fs (Fig. 6.62), the BSI yield exhibits a weak pulse length dependence, while the EII yield increases from $n_{imp}^L = 1.7$ at $\tau = 10$ fs to $n_{imp}^L = 5.2$ at $\tau = 100$ fs. This results in a marked increase in n_{ii}^L, with the EII becoming the dominant ionization mechanism at $\tau = 100$ fs (Fig. 6.62). Another interesting effect pertains to 'laser free' EII by the persistent nanoplasma (with a modest yield of 10%), which was documented. On the other hand, at higher intensities ($I_m > 10^{17}\,\mathrm{Wcm}^{-2}$), where the nanoplasma is transient and the cross sections

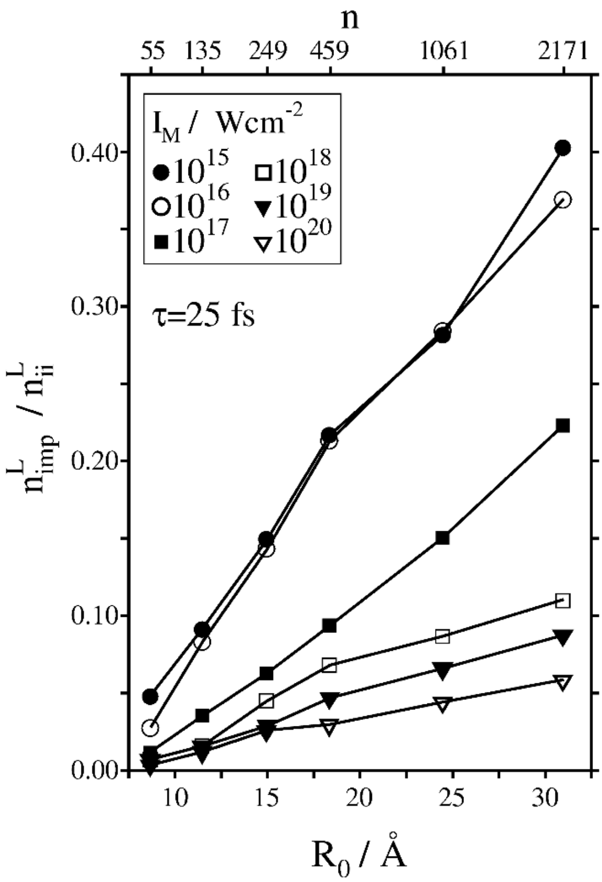

Fig. 6.61. The cluster size dependence of the relative EII yield n^L_{imp}/n^L_{ii} for Xe$_n$ ($n = 55$–2171) clusters in the intensity range $I_m = 10^{15}$–10^{20} Wcm^{-2} ($\tau = 25$ fs).

for EII are reduced (due to the increase in the electron energy), EII competes with BSI, but does not lead to a net effect on the inner ionization levels.

6.6.4 Outer ionization

Cluster outer ionization manifests the nanoplasma response to the laser field, due to barrier suppression of the entire cluster [243] and due to quasiresonance effects [214, 239, 248]. The outer ionization removes all, or part, of the nanoplasma electrons by the laser field. In the simulations outer ionization is described in terms of a cluster barrier suppression ionization (CBSI) model, which involves the balancing between the cluster exterior Coulomb potential and the laser field potential at the cluster boundary. The long time outer

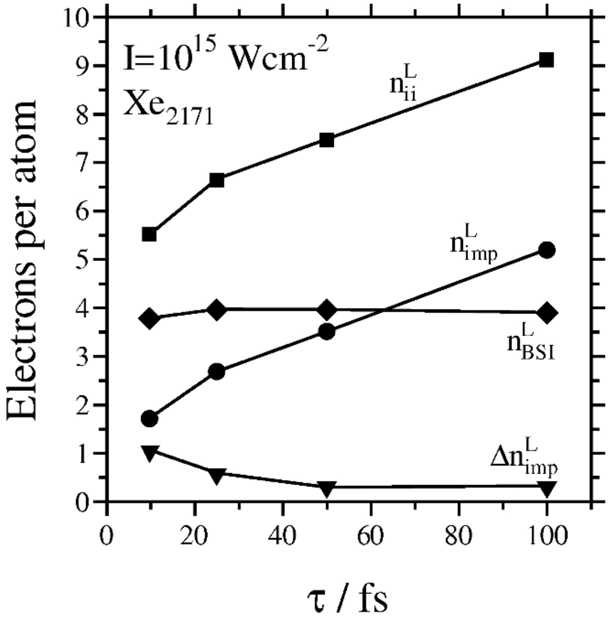

Fig. 6.62. The laser pulse length dependence of the long-time ionization levels of Xe_{2171} coupled to a laser field at $I_m = 10^{15}\,\mathrm{Wcm}^{-2}$ ($\tau = 10\,\mathrm{fs}$–$100\,\mathrm{fs}$). Ionization levels are presented for BSI (n^L_{BSI}, ◆), for EII (n^L_{imp}, ●), for inner ionization (n^L_{ii}, ■), and for "laser free" EII (Δn_{imp}, ▼) in the time domain after the termination of the laser pulse. The marked increase of the inner ionization yield with increasing τ marks control by laser pulse shaping.

ionization level was expressed in the form [279]

$$n^L_{oi} = F_m \gamma \xi^2 / \left(\frac{4\pi\sqrt{2}}{3} \right) \overline{B} \rho_{mol} R_0 \tag{6.53}$$

where F_m is the laser electric field for peak intensity I_m, $\rho_{mol} = 3n/4\pi R_0^3$ is the initial atomic / molecular constituent density expressed in terms of the initial cluster radius, $\xi = R(t)/R_0$ is the cluster expansion parameter due to CE and $\gamma \simeq 4$ is a numerical correction factor. This result is applicable for the intensity range and cluster size domain where a persistent nanoplasma prevails, i.e., $n^L_p = n^L_{ii} - n^L_{oi} > 0$ (or $n^L_{ii} > n^L_{oi}$). The use of (6.53) gives [279]

$$n^L_{oi} = A\sqrt{I_m}/R_0 \tag{6.54}$$

where

$$A = 2.745 \times 10^{-7} \gamma \xi^2 / \left(\frac{4\pi\sqrt{2}}{3} \right) \overline{B} \rho_{mol} \tag{6.55}$$

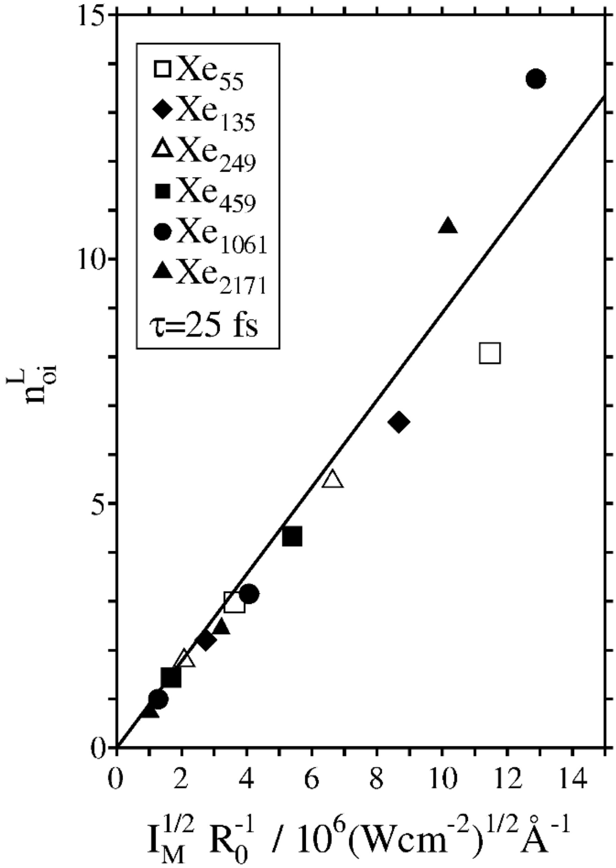

Fig. 6.63. A test of the electrostatic model for outer ionization, which predicts a linear dependence of n_{oi}^L vs $\sqrt{I_m}/R_0$ over broad cluster size ranges and laser intensities at constant τ, when the persistent nanoplasma prevails in Xe$_n$ clusters. $\tau = 25\,\mathrm{fs}$, $n = 55$–2171 at $I_m = 10^{15}$–$10^{16}\,\mathrm{Wcm^{-2}}$ and $n = 1061$, 2171 at $I_m = 10^{17}\,\mathrm{Wcm^{-2}}$.

In (6.54) and (6.55) I_m is presented in Wcm^{-2}, R_0 in Å, ρ_A in Å^{-3} and $\overline{B} = 14.4\,\mathrm{eV}$. The most striking prediction of the CBSI model, which is confirmed by the simulation data, is the linear dependence of n_{oi}^L on $\sqrt{I_m}/R_0^{(I)}$ over a broad laser intensity and cluster size range (at fixed τ), where the persistent nanoplasma exists. A typical example is portrayed in Fig. 6.63 for $\tau = 25\,\mathrm{fs}$ with $n = 55$–2171, and $I_m = 10^{15}$–$10^{17}\,\mathrm{Wcm^{-2}}$. From the dependence of the compound parameter $\gamma^{1/2}\xi$ on τ it was inferred that the outer ionization level for Xe$_n$ clusters is [279]

$$n_{oi}^L = 1.06 \times 10^{-7} \tau^{0.64} \sqrt{I_m}/R_0 \qquad (6.56)$$

where R_0 is given in Å, I_m in Wcm^{-2} and τ in fs. An identical function of the form $n_{oi}^L \propto \tau^{0.62}\sqrt{I_m}/R_0$ was obtained for outer ionization of $(\mathrm{D}_2)_n$ clusters pointing toward the generality of the electrostatic CBSI model. It is also gratifying that the relation between the electron outer ionization levels and the expansion parameter, $\xi = R(t)/R_0$, provides information on nuclear CE dynamics.

Complete outer ionization of a cluster can be specified by the cluster border radius $R_0^{(I)}$ at the intensity I_m, and prevails for $R_0 < R_0^{(I)}$, where cluster vertical ionization (CVI) is attained. The border radius for molecular clusters can be obtained from three independent sources.

1. The electrostatic model. Using (6.53) it was inferred that the maximal cluster radius $R_0^{(I)}$ for the attainment of the conditions $n_p^L = 0$ and $n_{oi}^L = n_{ii}^L = q_{av}$ is given by [279]
$$R_0^{(I)} = |F_m|\,\gamma\xi^2/\left(\frac{4\pi\sqrt{2}}{3}\right)\overline{B}\,\rho_{mol}\,q_{av} \tag{6.57}$$
Using (6.55) one gets
$$R_0^{(I)} = \frac{A\sqrt{I_m}}{q_{av}}\ . \tag{6.58}$$
2. Electron dynamics. $R_0^{(I)}$ can be inferred for the cluster size that exhibits complete (taken as 95%) outer ionization at the peak of the laser pulse, as obtained from molecular dynamics simulations [245, 246, 279].
3. The border radius $R_0^{(I)}$ is central in the characterization of the nuclear dynamics and energetics of CE. In the cluster size domain and in the laser intensity range where $R_0 \leq R_0^{(I)}$, the CVI is applicable, with the energetics (e.g., the average ion energy E_{av}) of CE being characterized by the cluster size scaling equation $E_{av} \propto q_{av}^2 R_0^2$, being explicitly independent of I_m and of other laser parameters. $R_0^{(I)}$ can be estimated from the deviation of the energetics of CE from the scaling equation [245, 246, 279].

The border radii $R_0^{(I)}$ for electron and nuclear dynamics in Xe_n, $(\mathrm{CD}_4)_n$ and $(\mathrm{D}_2)_n$ molecular clusters (Table 6.2) exhibit good agreement (within $\sim 20\%$) between the electrostatic model and the simulations of electron dynamics. From this agreement it can be inferred, on the basis of (6.54), (6.57) and (6.58), that for electron and nuclear explosion dynamics in molecular clusters [279]
$$R_0^{(I)} \propto \frac{\sqrt{I_m}\xi^2}{q_{mol}\,\rho_{mol}} \tag{6.59}$$
where q_{mol} is the average charge per molecule (or atomic constituent) and ρ_{mol} is the initial molecular density. The dependence $R_0^{(I)} \propto \sqrt{I_m}/q_{av}$ implies that the border radii for $(\mathrm{D}_2)_n$ clusters are considerably larger than for $(\mathrm{CD}_4)_n$ and Xe_n clusters at the same intensity. For $(\mathrm{D}_2)_n$ clusters, over the entire

Table 6.2. Border radii $R_0^{(I)}$(Å) for electron dynamics and nuclear CE dynamics of multicharged molecular clusters.

	Xe_n [279]				$(\mathrm{CD}_4)_n$ [246]			$(\mathrm{D}_2)_n$ [245]			
I_M / Wcm^{-2}	q_{av}	$R_0^{(I)}$ / Å			q_{av}	$R_0^{(I)}$ / Å		q_{av}	$R_0^{(I)}$ / Å		
$\tau = 25\mathrm{fs}$		(1)	(2)	(3)		(1)	(2)		(1)	(2)	(3)
10^{15}	6	5.6						1	6.5	5.8	< 8
10^{16}	8	11.0	8.0		8	10.0	10.1	1	20.4	20.4	≈ 25
10^{17}	15	18.5	15.2	17.3	8	31.4	31.4	1	64.5	76.5	
10^{18}	23	38.0	32.4		8	99.5		1	204		
10^{19}	26	107			10	251		1	640		
10^{20}	36	244						1			

(1) Electrostatic model.
(2) Simulations of electron dynamics.
(3) Simulations of CE nuclear dynamics.

intensity range, and for $(\mathrm{CD}_4)_n$ clusters at $I_m = 10^{15}$–$10^{18}\,\mathrm{Wcm}^{-2}$, q_{mol} is constant (but distinct) for each cluster resulting in a $R_0^{(I)} \propto \sqrt{I_m}$ intensity dependence. For Xe_n the increase of $R_0^{(I)}$ with increasing $\sqrt{I_m}$ is sublinear, reflecting on the increase of $q_{mol} = q_{av}$ with increasing I_m. The scarce data for CE nuclear dynamics are in good agreement with the results for electron dynamics as well. The border radius $R_0^{(I)}$ builds a bridge between electron (outer ionization) dynamics and nuclear (CE) dynamics, which will now be considered.

6.6.5 Uniformity, energetics, kinematics, and dynamics of Coulomb explosion

Cluster electron dynamics triggers nuclear dynamics, with the outer ionization being accompanied and followed by CE [241, 242, 245, 246, 254, 271]. The multicharged (totally or partially ionized) metastable clusters undergo CE whose notable applications pertain to ion imaging [291], accelerator technology [292] of high-energy (keV–MeV) ions or nuclei, and extreme ultraviolet lithography [293].

The traditional view of CE under CVI conditions involves uniform ion expansion. This prevails for homonuclear clusters with an initially uniform, constant charge and spherically symmetric ion distributions, which retain the succession of the ion distances from the cluster center throughout the expansion [245, 246]. Time-dependent structures of the $(\mathrm{D}_2)_{2171}$ cluster at $I_m = 10^{18}\,\mathrm{Wcm}^{-2}$ (Fig. 6.58) manifest uniform CE, which corresponds to complete stripping of all the electrons from $(\mathrm{D}_2)_{2171}$. The CE exhibits a unimodal spatial expansion of the D^+ ions, as evident from the time-resolved

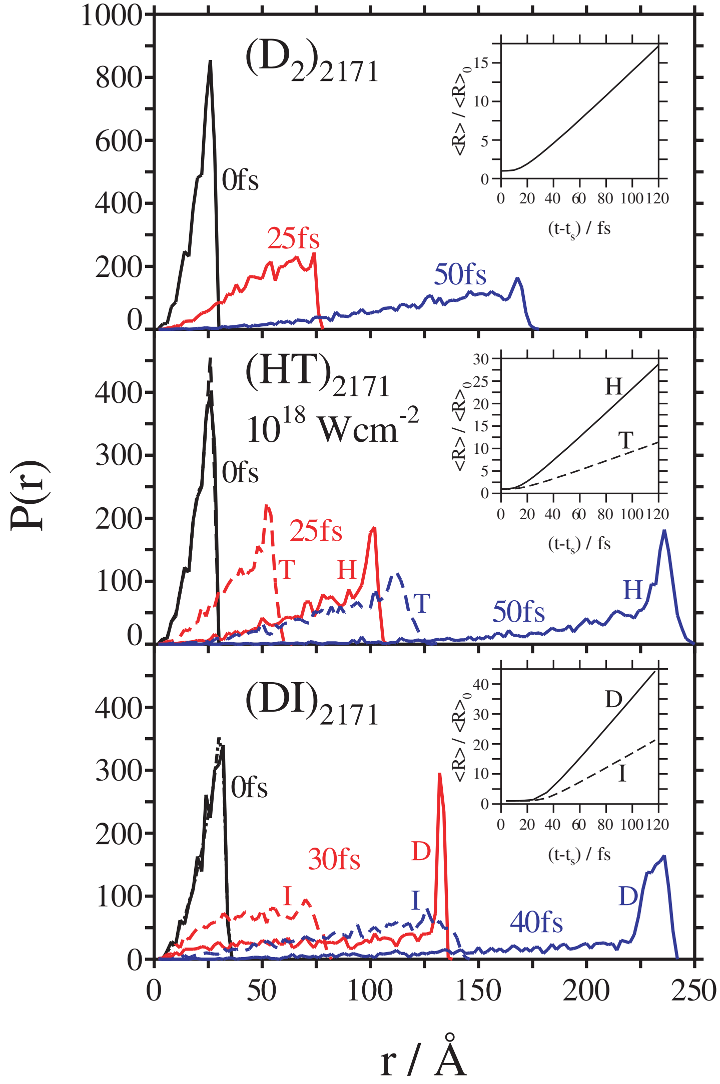

Fig. 6.64. The radial distribution functions $P(r)$ for the $(\mathrm{D}_2)_{2171}$, $(\mathrm{HT})_{2171}$ and $(\mathrm{DI})_{2171}$ clusters in a Gaussian laser field ($I_m = 10^{18}\,\mathrm{Wcm}^{-2}$ and $\tau = 25\,\mathrm{fs}$) at various times $t - t_s$. t_s is the starting time of the simulation with respect to the maximum of the Gaussian laser field envelope located at $t = 0$. For the heteronuclear $(\mathrm{HT})_{2171}$ and $(\mathrm{DI})_{2171}$ clusters, $P(r)$ is drawn separately for each ion (in blue and red,as marked on the panels), exhibiting shell formations of the non overlapping distributions of different isotope/element ions at times $t - t_s > 0$. These shells expand with different velocities. The insets portray the time-dependent increase of the first moments $\langle R\rangle$ of $P(r)$ relative to the first moment $\langle R\rangle_0$ at $t - t_s = 0$. Data are presented for different ions, as marked on the insets.

structures (Fig. 6.58) and from the single, broad time-dependent spatial distributions $P(r)$ at each t (Fig. 6.64). Even for the CE of ions from highly multicharged elemental clusters, e.g., $(\mathrm{Xe}^{+q})_n$ (Figs. 6.54 and 6.55), the explosion is nonuniform. At lower intensities of $I_m = 10^{15}\,\mathrm{Wcm}^{-2}$ outer ionization is incomplete, and the screening of CE by the persistent nanoplasma in the center of the cluster results in nonuniformity in the exterior explosion (Fig. 6.54). At $I_m = 10^{18}\,\mathrm{Wcm}^{-2}$, where outer ionization is complete, a spatial anisotropy in the angular distribution of the Xe^{q+} ($q = 22$–26) ions is exhibited (Fig. 6.55), with a velocity increase along the polarization axes of the laser field.

The dynamics of uniform CE (inset to $(\mathrm{D}_2)_{2171}$ in Fig. 6.64) will be characterized by the time dependence of $\langle R\rangle/\langle R\rangle_0$, where $\langle R\rangle$ is the first moment of the spatial distribution of the A^{q_A+} light ions at time t, while $\langle R\rangle_0$ is the initial value of $\langle R\rangle$. The CE dynamics is described by the near-linear time dependence [245, 246, 294]

$$\frac{\langle R\rangle}{\langle R\rangle_0} = a\,(t - t_{onset}) \tag{6.60}$$

at $t > t_{onset}$ (inset for $(\mathrm{D}_2)_{2171}$ in Fig. 6.64). The onset time t_{onset} in the linear dependence of $\langle R\rangle$ vs t (e.g., $t_{onset} = 10\,\mathrm{fs}$ for $(\mathrm{D}_2)_{2171}$) is due to the switching-off of acceleration effects in CE. From the electrostatic model of uniform CE under CVI conditions [245, 246, 294] $(a/\mathrm{fs})^{-1} = 1.074(\rho_{mol}\,q_A/m_A)^{1/2}$ where q_A is the ion charge, $q_{mol} = kq_A$, and m_A is ion mass. For the uniform CE of $(\mathrm{D}_2)_n$ clusters, the results of the electrostatic model (6.60), are in good agreement with the fit of the simulation data by (6.59).

Nonuniform CE under CVI conditions occurs in $\mathrm{A}_k^{q_A+}\mathrm{B}_l^{q_B+}$ light-heavy heteroclusters, which consist of k light A^{q_A+} ions of mass m_A and charge q_A, and l heavy B^{q_B+} ions of mass m_B and charge q_B (with $m_A < m_B$). The CE dynamics is governed by the kinematic parameter $\eta_{AB} = q_A m_B/q_B m_A$ [241, 242, 245, 246]. The nonuniform CE of $(\mathrm{H}^+\mathrm{T}^+)_{2171}$ heteroclusters (Fig. 6.58), for which $\eta_{HT} = 3$, manifests kinematic run-over effects of the H^+ ions relative to the T^+ ion. These kinematic effects are characterized by a spatial segregation of the exterior distribution of H^+ ions relative to an interior distribution of the T^+ ions (Fig. 6.58). The distinct spatial distributions of the H^+ and T^+ ions overlap at short times and separate at longer times (Fig. 6.64). The case of CE of extremely charged light-heavy $(\mathrm{A}_k^{q_A+}\mathrm{B}_l^{q_B+})_n$ heteroclusters (ECLHH) (corresponding to $m_A \ll m_B$ and $kq_A \ll lq_B$) exhibits the formation of exterior spherical nanoshells of the light ions, which manifest the attainment of transient self-organization driven by repulsive Coulomb interactions [250]. The time-dependent structures (Fig. 6.65) of CE of $(\mathrm{DI})_{2171}$ clusters at $I_m = 10^{18}\,\mathrm{Wcm}^{-2}$ correspond to $\eta_{DI} = 2.5$ and $q_I = 21$–23, with $q_D = 1 \ll q_I$, where q_I increases with increasing n due to ignition effects induced by the inner field, as is the case for extreme multielectron ionization. The fs CE dynamics reveals an extreme case of spatial segregation between the light D^+ ions and the heavy I^{q_I+} ions, with the formation of a transient halo of the expanding light D^+ ions, which surrounds the inner subcluster of

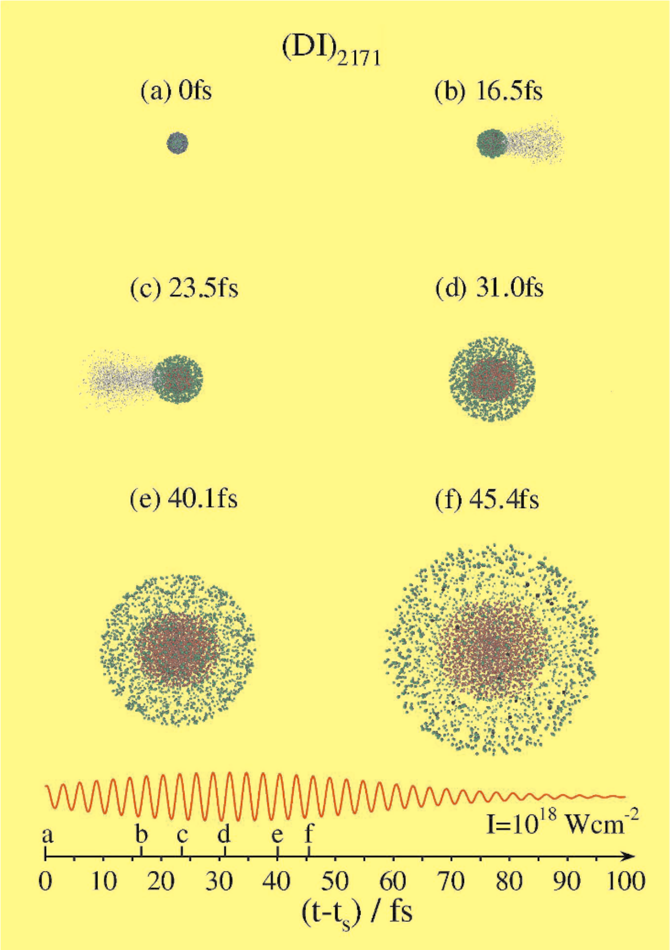

Fig. 6.65. Snapshots of the time-resolved structures in the Coulomb explosion of the $(DI)_{2171}$ cluster induced by a Gaussian laser pulse ($I_m = 10^{18}$ Wcm^{-2}, $\tau = 25$ fs). The lowest part of the panel portrays the time axis $t - t_s$ and the electric field of the laser. The instants of the snapshots are marked by a–f on the time axis. The deuterons are represented by green and the electrons by light gray spheres. The iodine atoms are color coded according to their charge; blue corresponds to the initial charge +1, deep red to the maximum charge +25, which can be obtained at this laser intensity. (a) The initial nanoplasma at $t - t_s = 0$, with the cluster radius $R_0 = 34.8$ Å. (b) At $t - t_s = 16.9$ fs the onset of the deuteron shell expansion becomes apparent. The radius of the deuteron shell, defined by the outermost D atoms, is 39.1 Å. The average charge per iodine atom is 16.0. (c) At 21.5 fs the average charge per iodine atom reaches 24.3 and the radius of the deuteron shell is 51 Å. (d) At 26.4 fs the outer ionization is complete. The radius of the deuteron shell grows to 76 Å and the expansion of the iodine shell sets in. At even longer times, (e) 31.8 fs and (f) 37.2 fs, the deuteron shell radius is 111 Å and 126 Å, respectively.

Table 6.3. Energetics and dynamics of Coulomb explosion of deuterium containing homo-nuclear $(D_2)_n$ clusters and heteronuclear $(A_k^{q_A+}B_l^{q_B+})_n$ or $(A_k^{q_A+}B_l^{q_B+}C_p^{q_C+})_n$ clusters at $I_m = 10^{18}\,\mathrm{Wcm}^{-2}$. Simulation data (marked SIM) are compared with the results of the electrostatic model (marked EML).

Cluster	ρ_{mol} (Å^{-3}) [a]	q_{mol} or q_B [c]	Z (eV) [d]		κ [d]		a (fs^{-1})	
			SIM [e]	EML [f]	SIM [e]	EML [f]	SIM [g]	EML [f]
$(D_2)_n$	0.025	2	12.5	13.6	0.61	0.60	0.16	0.17
$(CD_4)_n$	0.016	8	42.5	46.7	0.70	0.60		0.27
$(DI)_n$	0.013	22	115	165	0.80	0.83	0.50	0.45
$(CD_3I)_n$	0.010	26	130	181	0.80	0.83		

[a] Initial molecular density of molecular ions in the cluster.
[b] The cluster initial radius is related to n by $R_0 = (3n/4\pi\rho_{mol})^{1/3}$.
[c] Ion charge $q_{mol} = kq_A + lq_B + pq_C$ for cases (A) and (B), and $q_{mol} = lq_B + pq_C$ for ECLHH, where $q_I = 22$ is an average charge in the size domain $n = 1061$–2171 and $q_C = 4$ for $(CD_3I)_{2171}$.
[d] $E_M(n) = Zn^{2/3}$ and $\kappa = E_M(n)/E_{av}(n)$, with Z and κ being independent of n.
[e] Fig. 6.66.
[f] See text. For the ECLHHs we neglect a weak cluster size dependence of Z, due to the dependence of q_I on n, which arises from ignition and screening effects on inner ionization (6.57,6.62).
[g] From the time dependence of the first moment of the distribution of the light ions, $\langle R\rangle = \langle R\rangle_0 = a(t - t_{onset})$.

the I^{q_I+} ions (Fig. 6.64). The dynamics of nonuniform CE is given by (6.59) and (6.60) with $q_{mol} = kq_A + lq_B$, while for ECLHH $q_{mol} = lq_B$. Note that a is independent of the cluster size at fixed I_m. As evident from Table 6.3, the results of the electrostatic model, (6.60), account well for the simulation data (insets to Fig. 6.64). i.e., $a = 0.16\,\mathrm{fs}^{-1}$ ($0.17\,\mathrm{fs}^{-1}$) for H^+ ions from $(HT)_{2171}$, and $a = 0.56\,\mathrm{fs}^{-1}$ ($0.45\,\mathrm{fs}^{-1}$) for D^+ ions from $(DI)_{2171}$ at $I_m = 10^{18}\,\mathrm{Wcm}^{-2}$. The agreement between theory and simulation provides benchmark reference data for CE in the CVI domain. The maximization of the energies of the light ions in the CE of ECLHHs requires the applicability of the CVI ($I_m \gtrsim 10^{17}$–$10^{18}\,\mathrm{Wcm}^{-2}$), and the use of the highest attainable laser intensities for the maximization of the heavy atom charge q_B for effective energetic driving.

The maximum energy E_M and the average energy E_{av} of the light ions in the uniform CE of homonuclear clusters and in the nonuniform CE of heteronuclear clusters can be obtained from electrostatic models, which in the CVI limit result in the general expressions for the cluster size dependence [241, 242, 294]

$$E_M(n) = XR_0^2 \tag{6.61}$$

where $R_0 = (3n/4\pi\rho_{mol})^{1/3}$ is the initial cluster radius, whereupon [241, 242, 250, 251, 294]

$$E_M(n) = Zn^{2/3} \tag{6.62}$$

The ratio between E_M and E_{av} is [241, 242, 250, 251, 294]

$$E_{av}(n) = \kappa E_M(n) \tag{6.63}$$

The parameters X, Z and κ assume the following forms:

(A) For homonuclear $(A_2)_n$ clusters, $X = (4\pi/3)\overline{B}\rho_{mol}q_A q_{A_2}$ with $\overline{B} = 14.40\,\text{eVÅ}$, while $Z = (4\pi/3)^{1/3}\overline{B}q_{A_2}\rho_{mol}^{1/3}$ and $\kappa = 3/5$.

(B) For $(\mathrm{A}_k^{q_A+}\mathrm{B}_l^{q_B+})_n$ heteronuclear clusters with $m_A < m_B$ and $\eta_{AB} = 1$, $X = (4\pi/3)\overline{B}\rho_{mol}q_A q_{mol}$ where $q_{mol} = kq_A + lq_B$, $Z = (4\pi/3)^{1/3}$ $\overline{B}q_A q_{mol}\rho_{mol}^{1/3}$, and $\kappa = 3/5$.

(C) For nonuniform CE of an ECLHH $(\mathrm{A}_k^{q_A+}\mathrm{B}_l^{q_B+}\mathrm{C}_p^{q_C+})_n$ with $m_A < m_C \ll m_B$, $kq_A \ll lq_B$ and $q_{mol} \simeq lq_B + pq_C$, $X = 2\pi\overline{B}\rho_{mol}q_{mol}q_A$, $Z = (9\pi/2)^{1/3}\overline{B}q_A q_{mol}\rho_{mol}^{1/3}$ and $\kappa = 4/5$.

The simulation results for cluster CE at $I_m = 10^{18}\,\mathrm{Wcm}^{-2}$ for $(D_2)_n$ (case (A)), for $(CD_4)_n$ (case (B) with $q_C = 4$) and for $(DI)_n$ and $(CD_3I)_n$ (case (C)

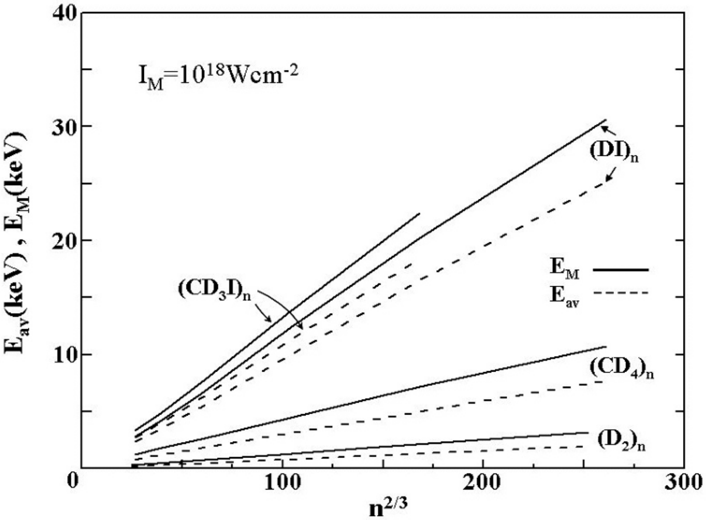

Fig. 6.66. The cluster size dependence of the maximal energies E_M (solid lines) and average energies E_{av} (dashed lines) of D^+ ions in the uniform CE of $(D_2)_n$ clusters and in the nonuniform CE of $(CD_4)_n$, $(DI)_n$ and $(CD_3I)_n$ clusters at $I_m = 10^{18}\,\mathrm{Wcm}^{-2}$ and $\tau = 25\,\mathrm{fs}$. The simulation data manifest the (divergent) power law E_M, $E_{av} \propto n^{2/3}$. Slight deviations from this scaling dependence for small $(DI)_n$ and $(CD_3I)_n$ ECLHHs originate from ignition and screening effects for inner ionization. The inset shows the dependence of E_M and I_m for clusters marked on the curves.

with $q_I = 21$–23), obey the size dependence E_M, $E_{av} \propto n^{2/3}$ (Fig. 6.66). The agreement between the Z parameters obtained from the simulations and the predictions of the electrostatic model (Table 6.3) is better than 30%, while the κ parameters are accounted for within 10% by the electrostatic model. The marked increase of E_M and E_{av} of D^+ in the series $(D_2)_n \ll (CD_4)_n \ll (DI)_n \ll (CD_3I)_n$ (at fixed n) exhibited in Fig. 6.66 manifests energy driving (i.e., energy boosting) by the multicharged heavy ions, which is determined by the ionic charge q_{mol} (e.g., at $I_m = 10^{18}\,\mathrm{Wcm}^{-2}$, $q_{mol} = 8$ for $(CD_4)_{2171}$, while $q_{mol} = 22$ for $(DI)_{2171}$ and $q_{mol} = 26$ for $(CD_3I)_{2171}$). Of considerable interest are the energy distributions of the high-energy D^+ ions and how they are affected by kinematic effects [241, 242, 245, 246, 250, 251]. All the kinetic energy distributions $P(E)$ of the product D^+ ions (Fig. 6.67) from CE of $(D_2)_n$ and from several heteroclusters, exhibit a maximal cut-off energy E_M analyzed below. For $(D_2)_n$ and $(CD_4)_n$ clusters the onset of $P(E)$ occurs at $E = 0$, while for the $(DI)_n$ and $(CD_3I)_n$ ECLHHs a narrow distribution of $P(E)$ is exhibited with a relative energy spread $\varDelta E/E_{av} \simeq 0.2$. The EML for uniform CE results in $P(E) = (3/2E_M)(E/E_M)^{1/2}$ $(E \le E_M)$, in agreement with the simulated energy distribution for CE of $(D_2)_n$ (inset for $(D_2)_{16786}$ to Fig. 6.67). For $(CD_4)_n$ clusters a marked deviation of $P(E)$ from the $E^{1/2}$ relation is exhibited with about 75% of the D^+ ions lying in a narrow energy interval $\varDelta E/E_{av} \simeq 0.4$, below E_M, manifesting kinematic run-over effects (inset for $(CD_4)_{4213}$ to Fig. 6.57). The EML for CE of the extremely charged light–heavy heteroclusters for a frozen subcluster of the I^{q_I+} ions predicts a low-energy onset of the energy distribution at $E_{min} = (4\pi/3)^{1/3}\overline{B}q_A q_B \rho_{mol} n^{2/3}$ with $P(E) = (3/E_{min})[3 - (2E/E_{min})]^{1/2}$ for $E_{min} \le E \le 3E_{min}/2$, where $E_M = 3E_{min}/2$ and $E_{av} = 6E_{min}/5$. The narrow distribution of $P(E)$ for CE of $(DI)_{2171}$ and of $(CD_3I)_{2171}$ (Fig. 6.67) is in accord with these predictions. This CE of $(DI)_n$ and $(CD_3)_n$ light–heavy heteroclusters constitutes an extreme manifestation of kinematic run-over effects, resulting in a narrow, high-energy distribution of the light ions.

6.6.6 Nuclear fusion driven by cluster Coulomb explosion

Eighty years of search for table-top nuclear fusion driven by bulk or surface chemical reactions, which involved the production of deuterons by catalytic processes [295] or by electrochemical methods [296], reflect on a multitude of experimental and conceptual failures [297]. This is not surprising, as the typical deuteron kinetic energies of 10 keV–100 keV are required for dd nuclear fusion, i.e., $D^+ + D^+ \rightarrow {}^3He + n + 3.3\,\mathrm{MeV}$ and $T^+ + H^+ + 4.0\,\mathrm{MeV}$. This characterizes the lower limit of the D^+ energy domain for the accomplishment of nuclear fusion, which cannot be attained in ordinary chemical reactions in macroscopic bulk or surface systems. CE of multicharged clusters produces high-energy (1 keV–1 MeV) ions in the energy domain of nuclear physics. Nuclear fusion can be driven by energetic deuterons produced by CE of multicharged deuterium containing homonuclear $(D_2)_n$ clus-

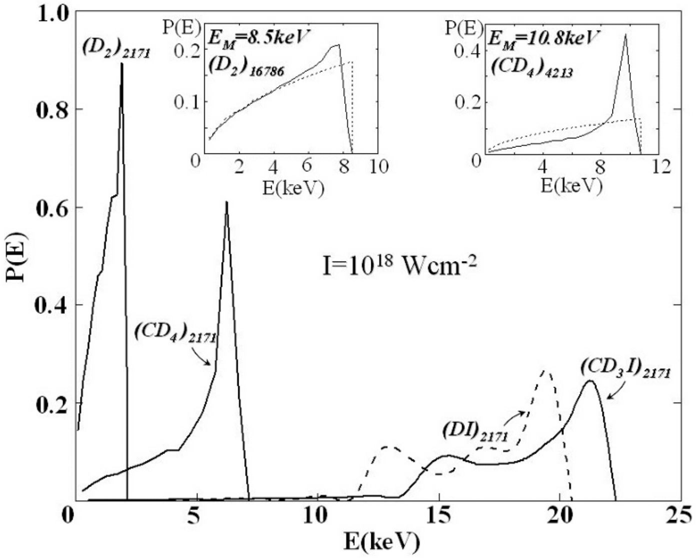

Fig. 6.67. The kinetic energy distributions of D^+ ions from several clusters (marked on the curves) at $I_m = 10^{18}$ Wcm^{-2} and $\tau = 25$ fs. The two insets show the simulated data (solid curves) and the results of the ELM (dashed curves) for CE of $(D_2)_{16786}$ and $(CD_4)_{4213}$.

ters [221,241,254,255,257] and heteronuclear (e.g., $(D_2O)_n$, [224,230,233,241] $(CD_4)_n$ [213, 226, 242, 259], $(DI)_n$) [250, 251]) clusters. CE in an assembly of deuterium containing homonuclear or heteronuclear clusters produces a plasma filament within the laser focal region, which constitutes a source of high-energy deuterons for nuclear fusion. Compelling experimental [254, 255] and theoretical [211, 245] evidence was advanced for nuclear fusion driven by CE (NFDCE) in an assembly of $(D_2)_n$ clusters. It was proposed and demonstrated [211, 241, 242, 246, 250, 251, 294] a marked enhancement of yields for NFDCE of deuterium containing heteroclusters due to energetic driving and kinematic effects.

While the quest for table-top nuclear fusion was realized for cluster CE, as well as for neutron production driven by a macroscopic piezoelectric crystal in a deuterium gas [298], these constitute low-yield processes. The neutron yield, Y, experimentally observed by Ditmire et al. [254, 255] for NFDCE of $(D_2)_n$ clusters ($n = 10^3$–2×10^4), is $Y \simeq 10^3$–10^4 per laser pulse (at $I_m = 10^{17}$ Wcm^{-2}). We demonstrated a seven orders of magnitude enhancement of Y in the NFDCE of ECLHHs, e.g., $(DI)_n$ and $(CD_3I)_n$ as compared to Y from $(D_2)_n$ clusters of the same size [294].

CE of multicharged deuterium containing heteroclusters and, in particular, of ECLHHs, manifests a marked increase of the average and maximal ener-

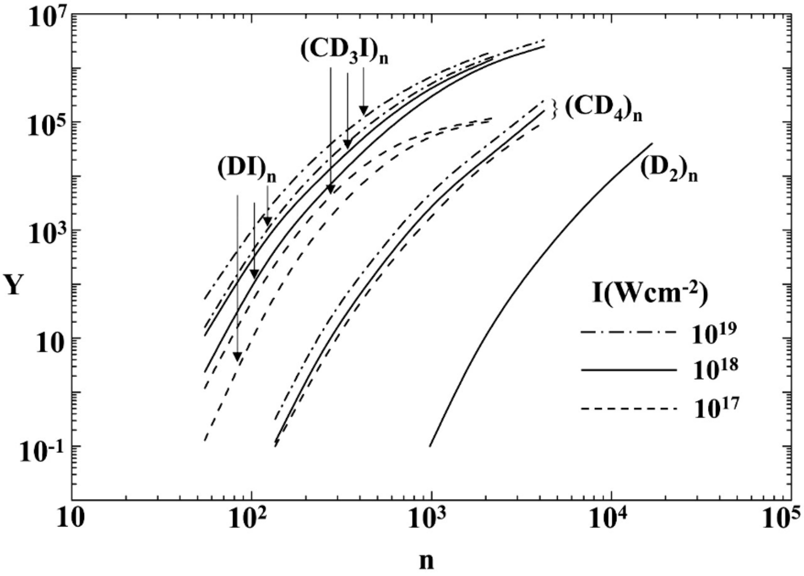

Fig. 6.68. Neutron yields per laser pulse (see text) for NFDCE of $(D_2)_n$, $(CD_4)_n$, $(DI)_n$ and $(CD_3I)_n$ clusters in the intensity range 10^{17}–10^{19} Wcm^{-2}.

gies of the D^+ ions. This is due to energetic driving effects by multicharged heavy ions and to the narrowing of the energy redistribution at high energies (just below E_M) due to kinematic run-over effects, (6.61). These energetic and kinematic driving effects will result in a marked enhancement of the neutron yields Y from NFDCE of these heteroclusters, in comparison to NFDCE of $(D_2)_n$ clusters of the same size. The fusion yield per laser pulse in a plasma filament (produced by a laser of intensity $I_m = 10^{16}$–10^{18} Wcm^{-2}) is given by $Y = (1/2)\rho_d^2 V_f(\overline{\ell}/\overline{v})\langle\sigma v\rangle$ where ρ_d is the deuteron density within the (cylindrical) reaction volume V_f, v is the relative velocity of the colliding nuclei, $\overline{v}$ is their average velocity, σ the fusion cross section, $\overline{\ell}$ is the deuterons mean free path, while $\langle\ \rangle$ denotes an average over the energy distribution. Using the conditions of the Lawrence-Livermore experiment, $\rho_d = 2 \times 10^{19}\,\mathrm{cm}^{-3}$ and $V_f = 6 \times 10^{-5}\,\mathrm{cm}^3$, while $\overline{\ell} = 0.016\,\mathrm{cm}$. The neutron yields Y (per laser pulse) calculated under the conditions of the Lawrence-Livermore experiment [254] for $I_m > 10^{17}$ Wcm^{-2} are higher by 2–3 orders of magnitude for CE of $(CD_4)_n$ clusters than for $(D_2)_n$ clusters of the same size (Fig. 6.68). The theoretical predictions [211, 241, 242, 246, 250, 251, 294] were experimentally confirmed in Sacley [259], the Lawrence-Livermore laboratory [256], and in the Max Born Institute [224]. Moving to NFDCE of extremely charged light-heavy heterocluster, e.g., $(D^+I^{25+})_n$ and $(CH_3I)_n$ (Fig. 6.68), Y can be enhanced by another 2–3 orders of magnitude over $(CD_4)_n$ clusters of the same size. For $(DI)_n$ and $(CD_3I)_n$ extremely charged light–heavy heteroclusters in the size domain $n = 1000$–2000 at $I_m = 10^{18}$–$10^{19}\,\mathrm{Wcm^{-2}}$, a dramatic increase of the neutron yields in the NFDCE of ECLHHs manifests energetic driving and kinematic effects. The realization of dd "hot–cold" nuclear fusion driven by CE made an 80 years old quest [297] for table–top nuclear fusion come true. An interesting application of NFDCE (with neutron yields of up to $\sim 10^9$ per laser pulse, see Fig. 6.68) pertains to the production of 100 ps–1 ns neutron pulses, which will be of interest for the exploration of time–resolved structures. Another "spin off" of nuclear reactions in cluster beams driven by ultraintense lasers pertains to nuclear astrophysics.

6.6.7 Table-top nucleosynthesis

Cluster dynamics transcends molecular dynamics toward nuclear reactions in ultraintense laser fields (Sect. 6.6.6). On the basis of theoretical and computational studies Last and Jortner proposed and demonstrated [299] that CE of molecular clusters will drive astrophysical nucleosynthesis [299,300] of protons with heavier nuclei

$$^{12}\mathrm{C}^{6+} + \mathrm{H}^+ \rightarrow {}^{13}\mathrm{N}^{7+} + \gamma \; ; \quad {}^{12}\mathrm{C}(\mathrm{p},\gamma)^{13}\mathrm{N} \tag{6.64}$$

$$^{14}\mathrm{N}^{7+} + \mathrm{H}^+ \rightarrow {}^{15}\mathrm{O}^{8+} + \gamma \; ; \quad {}^{14}\mathrm{N}(\mathrm{p},\gamma)^{15}\mathrm{N} \tag{6.65}$$

$$^{16}\mathrm{O}^{8+} + \mathrm{H}^+ \rightarrow {}^{17}\mathrm{F}^{9+} + \gamma \; ; \quad {}^{16}\mathrm{O}(\mathrm{p},\gamma)^{17}\mathrm{N} \tag{6.66}$$

These reactions are part of the CNO cycle that constitutes the energy source of hot stars, which results in the fusion of four protons into $^4\mathrm{He}^{2+}$, with $^{12}\mathrm{C}^{6+}$ serving as a regenerable catalyst in this set of reactions [300,301]. For the realization of the astrophysical nucleosynthesis reactions (6.64), (6.65) and (6.66), the reagent nuclei will be produced by CE of the completely ionized $(\mathrm{CH_4})_n$, $(\mathrm{H_2O})_n$ and $(\mathrm{NH_3})_n$ molecular clusters in ultraintense laser fields. The realization of nucleosynthesis of protons with $^{12}\mathrm{C}^{6+}$, $^{14}\mathrm{N}^{7+}$, and $^{16}\mathrm{O}^{8+}$ nuclei in exploding cluster beams requires the fulfillment of the following conditions:

1. Cluster sizes. One has to utilize the largest cluster size at the given (very high) laser intensity that allows for the formation of bare nuclei and for the attainment of the highest energies of the nuclei. This requires extreme inner ionization, together with complete cluster outer ionization. Complete outer ionization involves CVI for subsequent–parallel CE, being achieved for the cluster border radius (section 6.6.6), i.e., $R_0 \simeq R_0^{(I)}$. On the basis of the electrostatic CBSI model, $R_0^{(I)}$ (at $I_m = 10^{20}\,\mathrm{Wcm^{-2}}$) assumes the values:

   $$R_0^{(I)} = 750\,\text{Å}\ (n^{(I)} = 2.7 \times 10^7)\ \text{for}\ (\mathrm{CH_4})_{n^{(I)}}\ ,$$
   $$R_0^{(I)} = 500\,\text{Å}\ (n^{(I)} = 1.3 \times 10^7)\ \text{for}\ (\mathrm{NH_3})_{n^{(I)}}\ \text{and,}$$
   $$R_0^{(I)} = 360\,\text{Å}\ (n^{(I)} = 6.3 \times 10^6)\ \text{for}\ (\mathrm{H_2O})_{n^{(I)}}\ .$$

   Such large cluster (droplet) sizes are amenable for experimental preparation [224].

2. Complete inner ionization. The BSI and the ADK models (Sects. 6.6.1 and 6.6.2) were utilized for the estimates of the laser intensity thresholds required for the C, N and O single atoms, which are accomplished at $I_m \geq 4 \times 10^{19}\,\mathrm{Wcm}^{-2}$. The laser threshold intensity for the complete ionization of the corresponding molecular clusters is lower than that of a single atom, due to ignition effects (see Sect. 6.6.2). For the very large clusters of radius $R_0^{(I)}$, the intensity threshold values are $I_m = 10^{18}\,\mathrm{Wcm}^{-2}$ for $(\mathrm{NH}_3)_{n^{(I)}}$ and $I_m = 3 \times 10^{18}\,\mathrm{Wcm}^{-2}$ for $(\mathrm{H}_2\mathrm{O})_{n^{(I)}}$. The $(\mathrm{CH}_4)_n$ cluster requires a more detailed treatment of the optimal largest cluster size, in view of the resonance structure [300] in the energy-dependent cross sections for reaction (6.64).
3. Highest possible energies of the nuclei. The scaling law $E_M \propto R_0^2$ (Sect. 6.6.5) for the energetics of cluster CE under CVI conditions requires the use of the largest cluster size in the $R_0 \leq R_0^{(I)}$ domain. The energetics of the bare nuclei from exploding clusters of size $R_0^{(I)}$ at $I_m = 10^{20}\,\mathrm{Wcm}^{-2}$ are $E_M \simeq 3\,\mathrm{MeV}$ for protons and $E_M \simeq 30\,\mathrm{MeV}$ for the C^{6+}, N^{7+} and O^{8+} heavy nuclei. These energies are high enough to drive nucleosynthesis. The optimal conditions for the attainment of table-top nucleosynthesis reactions (6.64)–(6.66) driven by CE of molecular clusters, involve laser intensities of $I_m = 10^{19}$–$10^{20}\,\mathrm{Wcm}^{-2}$ and cluster sizes of $\mathrm{R}_0 = R^{(I)} = 400$–$800$Å in this intensity range. The high-energy Coulomb exploding nuclei produce a macroscopic plasma filament [254]. The nucleosynthesis reactions take place both inside the plasma filament (IF) where high-energy nuclei collide [245,246,254,255,294] and outside the plasma filament (OF), where the energetic nuclei produced inside the plasma filament collide with the nuclei of clusters in the cluster beam outside the filament [224] (Fig. 6.69). In the intensity range $I_m = 10^{16}$–$10^{18}\,\mathrm{Wcm}^{-2}$, where the volume of the plasma filament is large, i.e., $\simeq 10^{-3}$–10^{-4} cm^3, the IF mechanism dominates [254]. On the other hand, in the highest intensity range $I_m = 10^{19}$–$10^{20}\,\mathrm{Wcm}^{-2}$, which is of interest to us, the small values of $V_f \simeq 10^{-9}$–$10^{-7}\,\mathrm{cm}^3$, and the low values of the path of the energetic nuclei inside the plasma filaments, result in a dominating OF mechanism. The cluster size dependence of the nucleosynthesis yields (per laser pulse) were calculated using the experimental cross sections [301] and the theory of CE energetics under CVI conditions (Sect. 6.6.4). Figure 6.69 portrays the dependence of the nucleosynthesis yields vs the number n_A of atoms in the cluster. For $^{14}\mathrm{N}(\mathrm{p},\gamma)^{15}\mathrm{O}$ and $^{16}\mathrm{O}(\mathrm{p},\gamma)^{17}\mathrm{F}$ reactions (6.65) and (6.66), where no resonances are exhibited in the cross sections, a smooth dependent Y increases smoothly with increasing n_A, while for the $^{18}\mathrm{C}(\mathrm{p},\gamma)^{13}\mathrm{N}$ reaction (6.64) Y shows two peaks due to the resonance structure of the cross sections. At $I_m = 10^{20}\,\mathrm{Wcm}^{-2}$ ($\tau = 25\,\mathrm{fs}$), the maximal values of $Y = 50$–100 for γ production (per laser pulse) are predicted. Table-top astrophysical nucleosynthesis reactions are amenable to experimental observation.

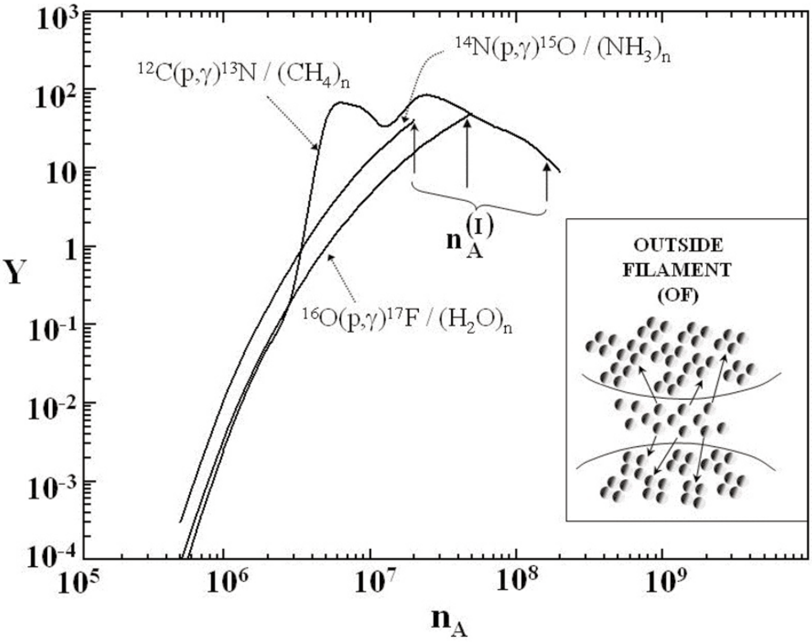

Fig. 6.69. Cluster size dependence of γ-ray yields (per laser pulse) for the nucleosynthesis reactions $^{12}C(p,\gamma)^{13}N$, $^{14}N(p,\gamma)^{15}O$, and $^{16}O(p,\gamma)^{17}F$, with the H^+, C^{6+}, N^{7+} and O^{8+} nuclei being produced by SE of $(CH_4)_n$, $(NH_3)_n$ and $(H_2O)_n$ clusters. The Y values are presented vs n_A, the total number of atoms in the cluster. The values of $n_A^{(I)}$, corresponding to the border radius $R_0^{(I)}$ for this intensity, are marked by vertical arrows. The dominating reaction mode involves the outside filament (OF) nucleosynthesis mechanism (schematically portrayed in the inset at the RHS of the figure).

6.6.8 Control in ultraintense laser fields

The control of reaction products in ultraintense laser fields ($I_m \geq 10^{15}\,\mathrm{Wcm}^{-2}$) is technically and conceptually different from the exploration of control in ordinary fields. At low laser intensities ($I_m \leq 10^{12}\,\mathrm{Wcm}^{-2}$), where perturbative treatment of radiative interactions is applicable, remarkable progress was made by pursuing control via pump-dump, phase control and optimal laser pulse shaping mechanisms. Control by laser pulse shaping is applicable up to $I_m = 10^{14}\,\mathrm{Wcm}^{-2}$. In this context, Vrakking et al. [222, 223] advanced and explored optimal control of the ionization level of Xe_n clusters by shaping the laser pulse train at $I_m = 10^{14}\,\mathrm{Wcm}^{-2}$, below the lowest limits of the ultraintense intensity domain. In ultraintense laser fields, where nonperturbative effects are fundamental, new mechanisms of control based on novel ionization mechanisms, electron dynamics and high–energy CE nuclear dynamics will be of considerable interest. In the new field of control by ultraintense lasers ($I_m \geq 10^{15}\,\mathrm{Wcm^{-2}}$), the concept of pump-dump low–field control seems to be inapplicable and optimal laser pulse shaping via learning algorithms is fraught with considerable technical difficulties. Ultraintense field control can be achieved by changing the laser parameters, i.e., intensity, pulse length, shape and phase. In what follows we shall discuss two scenarios for control of cluster extreme ionization and nucleosynthesis driven by CE in ultraintense laser fields:

1. Control of extreme multielectron ionization of clusters [279]. From the analysis of the complex cluster size and laser parameter dependence of the ionization level of Xe_n clusters (Sect. 6.6.2) we can infer that EII reactive dynamics opens avenues for the control of the ionization products (Sect. 6.6.3). The dependence of the long-time inner ionization yield on the pulse length, with $q_{av}(= n_{ii}^L)$ for Xe_{2171} at $I_m = 10^{15}\,\mathrm{Wcm^{-2}}$ (Fig. 6.62), constitutes control of extreme ionization in ultraintense laser fields. Of course, the ionization levels can markedly increase by raising the laser intensity, but this constitutes a trivial mode of control. More significant control involves product changes with changing the laser parameters (e.g., the pulse length). The variation of the laser pulse length leads to a marked change in the ionization products at a fixed laser intensity. This control mechanism for Xe_n clusters is induced by EII and is expected to be effective in the intensity range and cluster size domain where EII by the persistent nanoplasma does prevail. This will be realized in the intensity range $I_m = 10^{15}$–$10^{16}\,\mathrm{Wcm^{-2}}$ for the large cluster size domain of Xe_n ($n = 459$–2171) presented in Sects. 6.6.2 and 6.6.3. The results presented in this section established an ultraintense laser pulse length control mechanism driven by EII in the persistent nanoplasma within clusters of heavy atoms. It will be instructive to provide a further analysis of single pulse and multiple pulse nanoplasma electron dynamics and ionization levels in Xe_n clusters, by assessing the contribution of EII to optimal control in ultraintense laser fields.
2. Branching ratios in nucleosynthesis. CE of extremely ionized molecular heteroclusters containing carbon, deuterium and hydrogen, will result in branching between the $^{12}\mathrm{C(p,}\gamma)^{13}\mathrm{N}$ nucleosynthesis and the $^{2}\mathrm{D(d,n)}^{3}\mathrm{He}$ dd fusion. To be more explicit, consider the CE of a completely ionized $(\mathrm{CH_3D})_n$ cluster
$$(\mathrm{CH_3D})_n \rightarrow \mathrm{C}^{6+} + \mathrm{D}^{+} + 3\mathrm{H}^{+} \tag{6.67}$$
Two parallel nuclear reactions are expected to occur inside and/or outside the nanoplasma filament
$$^{12}\mathrm{C}^{6+} + {}^{1}\mathrm{H}^{+} \rightarrow {}^{13}\mathrm{N}^{7+} + \gamma\ ; \quad {}^{12}\mathrm{C(p,}\gamma)^{13}\mathrm{N} \tag{6.68}$$
$$^{2}\mathrm{D}^{+} + {}^{2}\mathrm{D}^{+} \rightarrow {}^{3}\mathrm{He}^{2+} + \mathrm{n}\ ; \quad {}^{2}\mathrm{D(d,n)}^{3}\mathrm{He} \tag{6.69}$$
Control of the branching ratio between reactions (6.68) and (6.69) (interrogated by monitoring the ratio of the numbers of (γ rays)/(neutrons))

can be induced by changing the cluster size and the laser parameters. Lowering the laser intensity in the threshold region for complete C atom ionization can reduce the contribution of the ^{12}C(p,γ)^{13}N reaction, while changing the pulse shape may modify the energetics of CE. Perspectives will also be explored for laser control by a further increase in the energies of the H^+, D^+ and C^{6+} nuclei by CE of the light–heavy $(CDH_2I)_n$ heteroclusters, where the highly charged I^{25+} ion (at $I_m = 10^{19}\,\mathrm{Wcm}^{-2}$) or I^{35+} ion (at $I_m = 10^{20}\,\mathrm{Wcm}^{-2}$) will act as an energetic booster for those nuclei participating in the parallel ^{12}C(p,γ)^{13}N and ^{2}D(d,n)^{3}He nuclear reactions.

We addressed some new research directions in the realm of laser–cluster interaction in ultraintense laser fields ($I_m \geq 10^{15}\,\mathrm{Wcm}^{-2}$). In this new physical/chemical world, all the conventional 'rules of the game' regarding laser energy acquisition, storage and disposal in large finite systems have to be modified, differing quantitatively from the situation in ordinary, 'weak' laser fields. Two major novel research directions pertaining to control in ultraintense laser fields are emerging. First, a conceptual basis is being developed for control of exotic products (e.g., extreme ionization levels) in ultraintense laser fields. Second, cluster dynamics transcends molecular dynamics in large finite systems toward nuclear reactions (e.g., dd fusion and nucleosynthesis) driven by extreme cluster multielectron ionization in ultraintense laser fields, with the formation of unique clusters that consist of bare nuclei undergoing high-energy CE.

References

1. A. L'Huillier, P. Balcou, Phys. Rev. Lett. **70**, 774 (1993)
2. P. Agostini, F. Fabre, G. Mainfray, G. Petite, N.K. Rahman, Phys. Rev. Lett. **42**, 1127 (1979)
3. A. Zavriyev, P.H. Bucksbaum, J. Squier, F. Saline, Phys. Rev. Lett. **70**, 1077 (1993)
4. C. Kosmidis, P. Tzallas, K.W.D. Ledingham, T. McCanny, R.P. Singhal, P.F. Taday, A.J. Langley, J. Phys. Chem. A **103**, 6950 (1999)
5. M.J. DeWitt, R.J. Levis, J. Chem. Phys. **102**, 8670 (1995)
6. M.J. DeWitt, D.W. Peters, R.J. Levis, Chem. Phys. **218**, 211 (1997)
7. R.J. Levis, M.J. DeWitt, J. Phys. Chem. A **103**, 6493 (1999)
8. D.M. Villeneuve, S.A. Aseyev, P. Dietrich, M. Spanner, M.Y. Ivanov, P.B. Corkum, Phys. Rev. Lett. **85**, 542 (2000)
9. J. Purnell, E.M. Snyder, S. Wei, A.W. Castleman, Chem. Phys. Lett. **229**, 333 (1994)
10. M. Schmidt, D. Normand, C. Cornaggia, Phys. Rev. A **50**, 5037 (1994)
11. T. Ditmire, J. Zweiback, V.P. Yanovsky, T.E. Cowan, G. Hays, K.B. Wharton, Nature **398**, 489 (1999)
12. M.P. Kalachnikov, P.V. Nickles, H. Schönnagel, W. Sandner, Nucl. Instrum. Meth. A **472**, 254 (2001)

13. S. Larochelle, A. Talebpour, S.L. Chin, J. Phys. B **31**, 1201 (1998)
14. V. Schyja, T. Lang, H. Helm, Phys. Rev. A **57**, 3692 (1998)
15. A. Saenz, P. Lambropoulos, J. Phys. B **32**, 5629 (1999)
16. M.G. Baik, M. Pont, R. Shakeshaft, Phys. Rev. A **54**, 1570 (1996)
17. A. Apalategui, A. Saenz, P. Lambropoulos, J. Phys. B **33**, 2791 (2000)
18. A. Palacios, S. Barmaki, H. Bachau, F. Martin, Phys. Rev. A **71**, 063405 (2005)
19. A. Apalategui, A. Saenz, J. Phys. B **35**, 1909 (2002)
20. P.B. Corkum, Phys. Rev. Lett. **71**, 1994 (1993)
21. K.J. Schafer, B. Yang, L.F. Dimauro, K.C. Kulander, Phys. Rev. Lett. **70**, 1599 (1993)
22. L.V. Keldysh, Sov. Phys. JETP **20**, 1307 (1965)
23. M.J. DeWitt, R.J. Levis, J. Chem. Phys. **110**, 11368 (1999)
24. M. Lezius, V. Blanchet, D.M. Rayner, D.M. Villeneuve, A. Stolow, M.Y. Ivanov, Phys. Rev. Lett. **86**, 51 (2001)
25. M. Lezius, V. Blanchet, M.Y. Ivanov, A. Stolow, J. Chem. Phys. **117**, 1575 (2002)
26. I.V. Hertel, T. Laarmann, C.P. Schulz, in *Advances in atomic, molecular, and optical Physics, Vol. 50*, ed. by B. Bederson, H. Walter (Elsevier Academic Press, San Diego, 2005), pp. 219–286
27. M. Smits, C.A. de Lange, A. Stolow, D.M. Rayner, Phys. Rev. Lett. **93**, 203402 (2004)
28. J.R. Hiskes, Phys. Rev. **122**, 1207 (1961)
29. A.C. Riviere, D.R. Sweetman, Phys. Rev. Lett. **5**, 560 (1960)
30. T. Seideman, M.Y. Ivanov, P.B. Corkum, Phys. Rev. Lett. **75**, 2819 (1995)
31. T. Zuo, A.D. Bandrauk, Phys. Rev. A **52**, R2511 (1995)
32. Z. Mulyukov, M. Pont, R. Shakeshaft, Phys. Rev. A **54**, 4299 (1996)
33. M. Plummer, J.F. McCann, J. Phys. B **29**, 4625 (1996)
34. T.T. Nguyen-Dang, C. Lefebvre, H. Abou-Rachid, O. Atabek, Phys. Rev. A **71**, 023403 (2005)
35. A.S. Alnaser, M. Zamkov, X.M. Tong, C.M. Maharjan, P. Ranitovic, C.L. Cocke, I.V. Litvinyuk, Phys. Rev. A **72**, 041402(R) (2005)
36. T. Ergler, A. Rudenko, B. Feuerstein, K. Zrost, C.D. Schröter, R. Moshammer, J. Ullrich, Phys. Rev. Lett. **95**, 093001 (2005)
37. H.T. Yu, T. Zuo, A.D. Bandrauk, Phys. Rev. A **54**, 3290 (1996)
38. A. Saenz, Phys. Rev. A **61**, 051402(R) (2000)
39. A. Saenz, Phys. Rev. A **66**, 063407 (2002)
40. A. Saenz, Phys. Rev. A **66**, 063408 (2002)
41. K. Harumiya, I. Kawata, H. Kono, Y. Fujimura, J. Chem. Phys. **113**, 8953 (2000)
42. A. Saenz, J. Phys. B **35**, 4829 (2002)
43. G.R. Hanson, J. Chem. Phys. **62**, 1161 (1975)
44. A. Saenz, J. Phys. B **33**, 4365 (2000)
45. M.V. Ammosov, N.B. Delone, V.P. Krainov, Sov. Phys. JETP **64**, 1191 (1986)
46. A. Saenz, J. Phys. B **33**, 3519 (2000)
47. M. Awasthi, A. Saenz, J. Phys. B **39**, S389 (2006)
48. A. Scrinzi, M. Geissler, T. Brabec, Phys. Rev. Lett. **83**, 706 (1999)
49. M. Awasthi, Y.V. Vanne, A. Saenz, J. Phys. B **38**, 3973 (2005)
50. X. Urbain, B. Fabre, E.M. Staicu-Casagrande, N. de Ruette, V.M. Andrianarijaona, J. Jureta, J.H. Posthumus, A. Saenz, E. Baldit, C. Cornaggia, Phys. Rev. Lett. **92**, 163004 (2004)

51. E. Goll, G. Wunner, A. Saenz, Phys. Rev. Lett. **97**, 103003 (2006)
52. T. Ergler, B. Feuerstein, A. Rudenko, K. Zrost, C.D. Schröter, R. Moshammer, J. Ullrich, Phys. Rev. Lett. **97**, 103004 (2006)
53. A. Palacios, H. Bachau, F. Martin, Phys. Rev. Lett. **96**, 143001 (2006)
54. C. Cornaggia, J. Lavancier, D. Normand, J. Morellec, P. Agostini, J.P. Chambaret, A. Antonetti, Phys. Rev. A **44**, 4499 (1991)
55. M.J. DeWitt, R.J. Levis, Phys. Rev. Lett. **81**, 5101 (1998)
56. A.N. Markevitch, N.P. Moore, R.J. Levis, Chem. Phys. **267**, 131 (2001)
57. A.D. Bandrauk, J. Ruel, Phys. Rev. A **59**, 2153 (1999)
58. A.D. Bandrauk, S. Chelkowski, Chem. Phys. Lett. **336**, 518 (2001)
59. A.D. Bandrauk, S. Chelkowski, Phys. Rev. Lett. **84**, 3562 (2000)
60. A.M. Perelomov, V.S. Popov, M.V. Terent'ev, Sov. Phys. JETP **23**, 924 (1966)
61. M.J. DeWitt, R.J. Levis, J. Chem. Phys. **108**, 7045 (1998)
62. M.J. DeWitt, B.S. Prall, R.J. Levis, J. Chem. Phys. **113**, 1553 (2000)
63. N.P. Moore, R.J. Levis, J. Chem. Phys. **112**, 1316 (2000)
64. L. Pan, L. Armstrong, J.H. Eberly, J. Opt. Soc. Am. B **3**, 1319 (1986)
65. P.H. Bucksbaum, R.R. Freeman, M. Bashkansky, T.J. McIlrath, J. Opt. Soc. Am. B **4**, 760 (1987)
66. R.R. Freeman, P.H. Bucksbaum, J. Phys. B **24**, 325 (1991)
67. N.P. Moore, A.N. Markevitch, R.J. Levis, J. Phys. Chem. A **106**, 1107 (2002)
68. T.D.G. Walsh, F.A. Ilkov, J.E. Decker, S.L. Chin, J. Phys. B **27**, 3767 (1994)
69. A. Talebpour, S. Larochelle, S.L. Chin, J. Phys. B **31**, 2769 (1998)
70. J. Muth-Bohm, A. Becker, S.L. Chin, F.H.M. Faisal, Chem. Phys. Lett. **337**, 313 (2001)
71. S. Mukamel, S. Tretiak, T. Wagersreiter, V. Chernyak, Science **277**, 781 (1997)
72. S. Tretiak, V. Chernyak, S. Mukamel, Phys. Rev. Lett. **77**, 4656 (1996)
73. S. Tretiak, V. Chernyak, S. Mukamel, Chem. Phys. Lett. **259**, 55 (1996)
74. H.T. Yu, T. Zuo, A.D. Bandrauk, J. Phys. B **31**, 1533 (1998)
75. H.T. Yu, A.D. Bandrauk, Phys. Rev. A **56**, 685 (1997)
76. S. Chelkowski, A. Conjusteau, T. Zuo, A.D. Bandrauk, Phys. Rev. A **54**, 3235 (1996)
77. E.M. Snyder, S.A. Buzza, A.W. Castleman, Phys. Rev. Lett. **77**, 3347 (1996)
78. K.W.D. Ledingham, R.P. Singhal, Int. J. Mass Spectrom. Ion Process. **163**, 149 (1997)
79. T. Baumert, G. Gerber, Phys. Scr. **T72**, 53 (1997)
80. A.N. Markevitch, S.M. Smith, D.A. Romanov, H.B. Schlegel, M.Y. Ivanov, R.J. Levis, Phys. Rev. A **68**, 011402 (2003)
81. A.N. Markevitch, D.A. Romanov, S.M. Smith, H.B. Schlegel, M.Y. Ivanov, R.J. Levis, Phys. Rev. A **69**, 013401 (2004)
82. S.M. Smith, A.N. Markevitch, D.A. Romanov, X.S. Li, R.J. Levis, H.B. Schlegel, J. Phys. Chem. A **108**, 11063 (2004)
83. A.N. Markevitch, D.A. Romanov, S.M. Smith, R.J. Levis, Phys. Rev. Lett. **92**, 063001 (2004)
84. A.N. Markevitch, D.A. Romanov, S.M. Smith, R.J. Levis, Phys. Rev. Lett. **96**, 163002 (2006)
85. R.J. Levis, G.M. Menkir, H. Rabitz, Science **292**, 709 (2001)
86. A. Assion, T. Baumert, M. Bergt, T. Brixner, B. Kiefer, V. Seyfried, M. Strehle, G. Gerber, Science **282**, 919 (1998)

87. N.P. Moore, G.M. Menkir, A.N. Markevitch, P. Graham, R.J. Levis, in *Laser control and manipulation of molecules*, *ACS symposium series*, vol. 821, ed. by A.D. Bandrauk, Y. Fujimura, R.J. Gordon (Amer. Chem. Soc., Washington, 2002), pp. 207–220
88. D.J. Tannor, S.A. Rice, Adv. Chem. Phys. **70**, 441 (1988)
89. P. Brumer, M. Shapiro, Laser Part. Beams **16**, 599 (1998)
90. W.S. Warren, H. Rabitz, M. Dahleh, Science **259**, 1581 (1993)
91. M. Shapiro, P. Brumer, in *Advances in atomic, molecular, and optical Physics*, vol. 42 (Academic Press, San Diego, 2000), pp. 287–345
92. H. Rabitz, R. de Vivie-Riedle, M. Motzkus, K. Kompa, Science **288**, 824 (2000)
93. A.M. Weiner, Opt. Quantum Electron. **32**, 473 (2000)
94. J.X. Tull, M.A. Dugan, W.S. Warren, in *Advances in magnetic and optical resonance*, vol. 20 (Academic Press, New York, 1997), p. 1
95. R.S. Judson, H. Rabitz, Phys. Rev. Lett. **68**, 1500 (1992)
96. J. Berkowitz, G.B. Ellison, D. Gutman, J. Phys. Chem. **98**, 2744 (1994)
97. S. Vajda, A. Bartelt, E.C. Kaposta, T. Leisner, C. Lupulescu, S. Minemoto, P. Rosendo-Francisco, L. Wöste, Chem. Phys. **267**, 231 (2001)
98. C. Daniel, J. Full, L. Gonzalez, C. Kaposta, M. Krenz, C. Lupulescu, J. Manz, S. Minemoto, M. Oppel, P. Rosendo-Francisco, S. Vajda, L. Wöste, Chem. Phys. **267**, 247 (2001)
99. T. Hornung, R. Meier, M. Motzkus, Chem. Phys. Lett. **326**, 445 (2000)
100. B.J. Pearson, J.L. White, T.C. Weinacht, P.H. Bucksbaum, Phys. Rev. A **63**, 063412 (2001)
101. H. Rabitz, W.S. Zhu, Acc. Chem. Res. **33**, 572 (2000)
102. W.S. Zhu, H. Rabitz, J. Chem. Phys. **111**, 472 (1999)
103. Z.M. Lu, H. Rabitz, Phys. Rev. A **52**, 1961 (1995)
104. H. Rabitz, S. Shi, in *Advances in molecular vibrations and collision dynamics*, vol. 1A, ed. by J. Bowman (JAI Press, Greenwich, 1991), pp. 187–214
105. H.W. Kroto, J.R. Heath, S.C. O'Brien, R.F. Curl, R.E. Smalley, Nature **318**, 162 (1985)
106. M.S. Dresselhaus, G. Dresselhaus, P.C. Eklund, *Science of fullerenes and carbon nanotubes* (Academic Press, San Diego, 1996)
107. W. Krätschmer, L.D. Lamb, K. Fostiropoulos, D.R. Huffman, Nature **347**, 354 (1990)
108. E. Kolodney, A. Budrevich, B. Tsipinyuk, Phys. Rev. Lett. **74**, 510 (1995)
109. I.V. Hertel, H. Steger, J. De Vries, B. Weisser, C. Menzel, B. Kamke, W. Kamke, Phys. Rev. Lett. **68**, 784 (1992)
110. R.K. Yoo, B. Ruscic, J. Berkowitz, J. Chem. Phys. **96**, 911 (1992)
111. A. Reinköster, S. Korica, G. Prümper, J. Viefhaus, K. Godehusen, O. Schwarzkopf, M. Mast, U. Becker, J. Phys. B **37**, 2135 (2004)
112. S.C. O'Brien, J.R. Heath, R.F. Curl, R.E. Smalley, J. Chem. Phys. **88**, 220 (1988)
113. V. Foltin, M. Foltin, S. Matt, P. Scheier, K. Becker, H. Deutsch, T.D. Märk, Chem. Phys. Lett. **289**, 181 (1998)
114. M. Takayama, Int. J. Mass Spectrom. Ion Process. **121**, R19 (1992)
115. B. Walch, C.L. Cocke, R. Völpel, E. Salzborn, Phys. Rev. Lett. **72**, 1439 (1994)
116. S. Martin, J. Bernard, L. Chen, A. Denis, J. Desesquelles, Eur. Phys. J. D **4**, 1 (1998)
117. T. Schlathölter, O. Hadjar, J. Manske, R. Hoekstra, R. Morgenstern, Int. J. Mass Spectrom. **192**, 245 (1999)

118. A. Reinköster, B. Siegmann, U. Werner, H.O. Lutz, Radiat. Phys. Chem. **68**, 263 (2003)
119. J. Jensen, H. Zettergren, H.T. Schmidt, H. Cederquist, S. Tomita, S.B. Nielsen, J. Rangama, P. Hvelplund, B. Manil, B.A. Huber, Phys. Rev. A **69**, 053203 (2004)
120. H. Brauning, A. Diehl, R. Trassl, A. Theiss, E. Salzborn, A.A. Narits, L.P. Presnyakov, Fullerenes Nanotubes and Carbon Nanostructures **12**, 477 (2004)
121. E.E.B. Campbell, V. Schyja, R. Ehlich, I.V. Hertel, Phys. Rev. Lett. **70**, 263 (1993)
122. R. Vandenbosch, B.P. Henry, C. Cooper, M.L. Gardel, J.F. Liang, D.I. Will, Phys. Rev. Lett. **81**, 1821 (1998)
123. B. Farizon, M. Farizon, M.J. Gaillard, R. Genre, S. Louc, J. Martin, J.P. Buchet, M. Carré, G. Senn, P. Scheier, T.D. Märk, Int. J. Mass Spectrom. Ion Process. **164**, 225 (1997)
124. H.G. Busmann, T. Lill, B. Reif, I.V. Hertel, H.G. Maguire, J. Chem. Phys. **98**, 7574 (1993)
125. C. Yeretzian, K. Hansen, R.D. Beck, R.L. Whetten, J. Chem. Phys. **98**, 7480 (1993)
126. A. Bekkerman, A. Kaplan, E. Gordon, B. Tsipinyuk, E. Kolodney, J. Chem. Phys. **120**, 11026 (2004)
127. E.E.B. Campbell, K. Hansen, K. Hoffmann, G. Korn, M. Tchaplyguine, M. Wittmann, I.V. Hertel, Phys. Rev. Lett. **84**, 2128 (2000)
128. E.E.B. Campbell, G. Ulmer, I.V. Hertel, Phys. Rev. Lett. **67**, 1986 (1991)
129. K. Hansen, K. Hoffmann, E.E.B. Campbell, J. Chem. Phys. **119**, 2513 (2003)
130. F. Rohmund, M. Héden, A.V. Bulgakov, E.E.B. Campbell, J. Chem. Phys. **115**, 3068 (2001)
131. E.E.B. Campbell, R.D. Levine, Annu. Rev. Phys. Chem. **51**, 65 (2000)
132. E.E.B. Campbell, K. Hoffmann, H. Rottke, I.V. Hertel, J. Chem. Phys. **114**, 1716 (2001)
133. D. Bauer, F. Ceccherini, A. Macchi, F. Cornolti, Phys. Rev. A **64**, 063203 (2001)
134. B. Torralva, T.A. Niehaus, M. Elstner, S. Suhai, T. Frauenheim, R.E. Allen, Phys. Rev. B **64**, 153105 (2001)
135. G.P. Zhang, X. Sun, T.F. George, Phys. Rev. B **68**, 165410 (2003)
136. M. Kitzler, J. Zanghellini, C. Jungreuthmayer, M. Smits, A. Scrinzi, T. Brabec, Phys. Rev. A **70**, 041401 (2004)
137. T. Brabec, M. Côté, P. Boulanger, L. Ramunno, Phys. Rev. Lett. **95**, 073001 (2005)
138. M. Boyle, K. Hoffmann, C.P. Schulz, I.V. Hertel, R.D. Levine, E.E.B. Campbell, Phys. Rev. Lett. **87**, 273401 (2001)
139. M. Boyle, M. Heden, C.P. Schulz, E.E.B. Campbell, I.V. Hertel, Phys. Rev. A **70**, 051201 (2004)
140. M. Boyle, T. Laarmann, K. Hoffmann, M. Heden, E.E.B. Campbell, C.P. Schulz, I.V. Hertel, Eur. Phys. J. D **36**, 339 (2005)
141. M. Boyle, T. Laarmann, I. Shchatsinin, C.P. Schulz, I.V. Hertel, J. Chem. Phys. **122**, 181103 (2005)
142. T. Kunert, R. Schmidt, Phys. Rev. Lett. **86**, 5258 (2001)
143. F. Alvarado, R. Hoekstra, R. Morgenstern, T. Schlathölter, J. Phys. B **38**, L55 (2005)

144. M.J. Puska, R.M. Nieminen, Phys. Rev. A **47**, 1181 (1993)
145. R.R. Freeman, P.H. Bucksbaum, H. Milchberg, S. Darack, D. Schumacher, M.E. Geusic, Phys. Rev. Lett. **59**, 1092 (1987)
146. H. Kono, Y. Sato, Y. Fujimura, I. Kawata, Laser Physics **13**, 883 (2003)
147. H. Kono, Y. Sato, N. Tanaka, T. Kato, K. Nakai, S. Koseki, Y. Fujimura, Chem. Phys. **304**, 203 (2004)
148. C.P. Schick, P.M. Weber, J. Phys. Chem. A **105**, 3725 (2001)
149. N. Kuthirummal, P.M. Weber, Chem. Phys. Lett. **378**, 647 (2003)
150. K. Gluch, S. Matt-Leubner, O. Echt, B. Concina, P. Scheier, T.D. Mark, J. Chem. Phys. **121**, 2137 (2004)
151. S.A. Trushin, W. Fuß, W.E. Schmid, J. Phys. B **37**, 3987 (2004)
152. M. Murakami, R. Mizoguchi, Y. Shimada, T. Yatsuhashi, N. Nakashima, Chem. Phys. Lett. **403**, 238 (2005)
153. I. Shchatsinin, T. Laarmann, G. Stibenz, G. Steinmeyer, A. Stalmashonak, N. Zhavoronkov, C.P. Schulz, I.V. Hertel, J. Chem. Phys. **125**, 194320 (2006)
154. V.R. Bhardwaj, P.B. Corkum, D.M. Rayner, Phys. Rev. Lett. **93**, 043001 (2004)
155. A. Rentenier, A. Bordenave-Montesquieu, P. Moretto-Capelle, D. Bordenave-Montesquieu, J. Phys. B **37**, 2429 (2004)
156. K.R. Lykke, P. Wurz, J. Phys. Chem. **96**, 3191 (1992)
157. K.R. Lykke, Phys. Rev. A **52**, 1354 (1995)
158. M.E. Geusic, M.F. Jarrold, T.J. McIllrath, R.R. Freeman, W.L. Brown, J. Chem. Phys. **86**, 3862 (1987)
159. P.P. Radi, T.L. Bunn, P.R. Kemper, M.E. Molchan, M.T. Bowers, J. Chem. Phys. **88**, 2809 (1988)
160. H. Hohmann, R. Ehlich, S. Furrer, O. Kittelmann, J. Ringling, E.E.B. Campbell, Z. Phys. D **33**, 143 (1995)
161. G.P. Zhang, T.F. George, Phys. Rev. Lett. **93**, 147401 (2004)
162. T. Laarmann, I. Shchatsinin, A. Stalmashonak, M. Boyle, N. Zhavoronkov, J. Handt, R. Schmidt, C.P. Schulz, I.V. Hertel, Phys. Rev. Lett. (submitted)
163. G.N. Lewis, J. Am. Chem. Soc. **38**, 762 (1916)
164. T. Brabec, F. Krausz, Rev. Mod. Phys. **72**, 545 (2000)
165. P.M. Paul, E.S. Toma, P. Breger, G. Mullot, F. Auge, P. Balcou, H.G. Muller, P. Agostini, Science **292**, 1689 (2001)
166. C. Edmiston, K. Ruedenberg, Rev. Mod. Phys. **35**, 457 (1963)
167. W. Kohn, L.J. Sham, Phys. Rev. **140**, A1133 (1965)
168. C. Fiolhais, F. Nogueira, M.A.L. Marques (eds.), *A primer in Density Functional Theory*, *Lecture notes in Physics*, vol. 620 (Springer, Berlin, 2003)
169. R.M. Dreizler, E.K.U. Gross, *Density Functional Theory* (Springer, Berlin, 1990)
170. R.G. Parr, W. Yang, *Density Functional Theory of atoms and molecules* (Oxford University Press, New York, 1989)
171. P. Hohenberg, W. Kohn, Phys. Rev. B **136**, B864 (1964)
172. R.F.W. Bader, S. Johnson, T.H. Tang, P.L.A. Popelier, J. Phys. Chem. **100**, 15398 (1996)
173. A.D. Becke, K.E. Edgecombe, J. Chem. Phys. **92**, 5397 (1990)
174. T. Burnus, M.A.L. Marques, E.K.U. Gross, Phys. Rev. A **71**, 010501 (2005)
175. Y. Tal, R.F.W. Bader, Int. J. Quantum Chem. **12**, 153 (1978)
176. J.F. Dobson, J. Chem. Phys. **98**, 8870 (1993)

177. P.O. Löwdin, Phys. Rev. **97**, 1474 (1955)
178. R. McWeeny, Rev. Mod. Phys. **32**, 335 (1960)
179. A.D. Becke, Int. J. Quantum Chem. **23**, 1915 (1983)
180. T. Burnus, Time-dependent electron localization function. Diploma thesis, Freie Universität Berlin (2004)
181. E. Runge, E.K.U. Gross, Phys. Rev. Lett. **52**, 997 (1984)
182. M.A.L. Marques, C. Ullrich, F. Nogueira, A. Rubio, K. Burke, E.K.U. Gross, *Time-dependent Density Functional Theory*, *Lecture notes in Physics*, vol. 706 (Springer, Berlin, 2006)
183. M.A.L. Marques, E.K.U. Gross, Annu. Rev. Phys. Chem. **55**, 427 (2004)
184. R. van Leeuwen, Int. J. Mod. Phys. B **15**, 1969 (2001)
185. E. Gross, J. Dobson, M. Petersilka, in *Topics in current Chemistry*, vol. 181, ed. by R.F. Nalewajski (Springer, Berlin, 1996), pp. 81–172
186. E.K.U. Gross, W. Kohn, Adv. Quantum Chem. **21**, 255 (1990)
187. A. Savin, R. Nesper, S. Wengert, T.F. Fässler, Angew. Chem. Int. Ed. Engl. **36**, 1809 (1997)
188. M. Kohout, A. Savin, J. Comp. Chem. **18**, 1431 (1997)
189. J.B. Krieger, Y. Li, G.J. Iafrate, Phys. Rev. A **46**, 5453 (1992)
190. A. Castro, H. Appel, M. Oliveira, C.A. Rozzi, X. Andrade, F. Lorenzen, M.A.L. Marques, E.K.U. Gross, A. Rubio, phys. stat. sol. (b) **243**, 2465 (2006)
191. M.A.L. Marques, A. Castro, G.F. Bertsch, A. Rubio, Comput. Phys. Commun. **151**, 60 (2003)
192. B. Silvi, A. Savin, Nature **371**, 683 (1994)
193. D.B. Chesnut, J. Phys. Chem. A **104**, 11644 (2000)
194. M. Erdmann, E.K.U. Gross, V. Engel, J. Chem. Phys. **121**, 9666 (2004)
195. S. Shin, H. Metiu, J. Chem. Phys. **102**, 9285 (1995)
196. S. Shin, H. Metiu, J. Phys. Chem. **100**, 7867 (1996)
197. M. Erdmann, P. Marquetand, V. Engel, J. Chem. Phys. **119**, 672 (2003)
198. M. Erdmann, V. Engel, J. Chem. Phys. **120**, 158 (2004)
199. M. Erdmann, S. Baumann, S. Gräfe, V. Engel, Eur. Phys. J. D **30**, 327 (2004)
200. T. Kato, Commun. Pure Appl. Math. **10**, 151 (1957)
201. G.A. Mourou, C.P.J. Barty, M.D. Perry, Phys. Today **51**, 22 (1998)
202. G.A. Mourou, T. Tajima, S.V. Bulanov. Rev. Mod. Phys. **78**, 309 (2006)
203. T. Ditmire, T. Donnelly, A.M. Rubenchik, R.W. Falcone, M.D. Perry, Phys. Rev. A **53**, 3379 (1996)
204. T. Ditmire, J.W.G. Tisch, E. Springate, M.B. Mason, N. Hay, R.A. Smith, J. Marangos, M.H.R. Hutchinson, Nature **386**, 54 (1997)
205. T. Ditmire, Phys. Rev. A **57**, R4094 (1998)
206. K. Ishikawa, T. Blenski, Phys. Rev. A **62**, 063204 (2000)
207. J.S. Liu, R.X. Li, P.P. Zhu, Z.Z. Xu, J.R. Liu, Phys. Rev. A **64**, 033426 (2001)
208. P.B. Parks, T.E. Cowan, R.B. Stephens, E.M. Campbell, Phys. Rev. A **63**, 063203 (2001)
209. V.P. Krainov, A.S. Roshchupkin, J. Phys. B **34**, L297 (2001)
210. C. Rose-Petruck, K.J. Schafer, K.R. Wilson, C.P.J. Barty, Phys. Rev. A **55**, 1182 (1997)
211. I. Last, J. Jortner, Phys. Rev. A **64**, 063201 (2001)
212. V.P. Krainov, M.B. Smirnov, Phys. Rep.-Rev. Sec. Phys. Lett. **370**, 237 (2002)
213. D.A. Card, E.S. Wisniewski, D.E. Folmer, A.W. Castleman Jr., J. Chem. Phys. **116**, 3554 (2002)

214. U. Saalmann, J.M. Rost, Phys. Rev. Lett. **89**, 143401 (2002)
215. D. Bauer, A. Macchi, Phys. Rev. A **68**, 033201 (2003)
216. J. Schulz, H. Wabnitz, T. Laarman, P. Gürtler, W. Laasch, A. Swiderski, T. Möller, A.R.B. de Castro, Nucl. Instrum. Meth. A **507**, 572 (2003)
217. C. Siedschlag, J.M. Rost, Phys. Rev. A **67**, 013404 (2003)
218. C. Siedschlag, J.M. Rost, Phys. Rev. Lett. **93**, 043402 (2004)
219. C. Siedschlag, J.M. Rost, Phys. Rev. A **71**, 031401 (2005)
220. T. Laarmann, A.R.B. de Castro, P. Gürtler, W. Laasch, J. Schulz, H. Wabnitz, T. Möller, Phys. Rev. Lett. **92**, 143401 (2004)
221. K.W. Madison, P.K. Patel, D. Price, A. Edens, M. Allen, T.E. Cowan, J. Zweiback, T. Ditmire, Phys. Plasmas **11**, 270 (2004)
222. S. Zamith, T. Martchenko, Y. Ni, S.A. Aseyev, H.G. Muller, M.J.J. Vrakking, Phys. Rev. A **70**, 011201(R) (2004)
223. T. Martchenko, C. Siedschlag, S. Zamith, H.G. Muller, M.J.J. Vrakking, Phys. Rev. A **72**, 053202 (2005)
224. S. Ter-Avetisyan, M. Schnürer, D. Hilscher, U. Jahnke, S. Busch, P.V. Nickles, W. Sandner, Phys. Plasmas **12**, 012702 (2005)
225. D.M. Niu, H.Y. Li, F. Liang, L.H. Wen, X.L. Luo, B. Wang, H.B. Qu, J. Chem. Phys. **122**, 151103 (2005)
226. M. Hohenberger, D.R. Symes, K.W. Madison, A. Sumeruk, G. Dyer, A. Edens, W. Grigsby, G. Hays, M. Teichmann, T. Ditmire, Phys. Rev. Lett. **95**, 195003 (2005)
227. S. Ter-Avetisyan, M. Schnürer, P.V. Nickles, M. Kalashnikov, E. Risse, T. Sokollik, W. Sandner, A. Andreev, V. Tikhonchuk, Phys. Rev. Lett. **96**, 145006 (2006)
228. I. Last, J. Jortner, Phys. Rev. A **73**, 013202 (2006)
229. C. Siedschlag, J.M. Rost, Phys. Rev. Lett. **89**, 173401 (2002)
230. V. Kumarappan, M. Krishnamurthy, D. Mathur, Phys. Rev. A **67**, 063207 (2003)
231. E. Springate, S.A. Aseyev, S. Zamith, M.J.J. Vrakking, Phys. Rev. A **68**, 053201 (2003)
232. M. Rusek, A. Orlowski, Phys. Rev. A **71**, 043202 (2005)
233. G.M. Petrov, J. Davis, Phys. Plasmas **13**, 033106 (2006)
234. M. Krishnamurthy, D. Mathur, V. Kumarappan, Phys. Rev. A **69**, 033202 (2004)
235. J.S. Liu, C. Wang, B.C. Liu, B. Shuai, W.T. Wang, Y. Cai, H.Y. Li, G.Q. Ni, R.X. Li, Z.Z. Xu, Phys. Rev. A **73**, 033201 (2006)
236. M. Hirokane, S. Shimizu, M. Hashida, S. Okada, S. Okihara, F. Sato, T. Iida, S. Sakabe, Phys. Rev. A **69**, 063201 (2004)
237. S. Sakabe, S. Shimizu, M. Hashida, F. Sato, T. Tsuyukushi, K. Nishihara, S. Okihara, T. Kagawa, Y. Izawa, K. Imasaki, T. Iida, Phys. Rev. A **69**, 023203 (2004)
238. I. Last, J. Jortner, Phys. Rev. A **62**, 013201 (2000)
239. I. Last, J. Jortner, Phys. Rev. A **60**, 2215 (1999)
240. I. Last, J. Jortner, Z. Phys. Chemie-Int. J. Res. Phys. Chem. Chem. Phys. **217**, 975 (2003)
241. I. Last, J. Jortner, Phys. Rev. Lett. **87**, 033401 (2001)
242. I. Last, J. Jortner, J. Phys. Chem. A **106**, 10877 (2002)
243. I. Last, J. Jortner, J. Chem. Phys. **120**, 1336 (2004)

244. I. Last, J. Jortner, J. Chem. Phys. **120**, 1348 (2004)
245. I. Last, J. Jortner, J. Chem. Phys. **121**, 3030 (2004)
246. I. Last, J. Jortner, J. Chem. Phys. **121**, 8329 (2004)
247. I. Last, Y. Levy, J. Jortner, Proc. Natl. Acad. Sci. USA **99**, 9107 (2002)
248. I. Last, Y. Levy, J. Jortner, J. Chem. Phys. **123**, 154301 (2005)
249. Y. Levy, I. Last, J. Jortner, Mol. Phys. **104**, 1227 (2006)
250. I. Last, J. Jortner, Proc. Natl. Acad. Sci. USA **102**, 1291 (2005)
251. I. Last, J. Jortner, Phys. Rev. A **71**, 063204 (2005)
252. J. Jortner, Proc. R. Soc. London, Ser. A **356**, 477 (1998)
253. F. Krausz, Optics and Photonic News **13**, 62 (2002)
254. J. Zweiback, T.E. Cowan, R.A. Smith, J.H. Hartley, R. Howell, C.A. Steinke, G. Hays, K.B. Wharton, J.K. Crane, T. Ditmire, Phys. Rev. Lett. **85**, 3640 (2000)
255. J. Zweiback, T.E. Cowan, J.H. Hartley, R. Howell, K.B. Wharton, J.K. Crane, V.P. Yanovsky, G. Hays, R.A. Smith, T. Ditmire, Phys. Plasmas **9**, 3108 (2002)
256. K.W. Madison, P.K. Patel, M. Allen, D. Price, R. Fitzpatrick, T. Ditmire, Phys. Rev. A **70**, 053201 (2004)
257. M. Isla, J.A. Alonso, Phys. Rev. A **72**, 023201 (2005)
258. T.E. Dermota, D.P. Hydutsky, N.J. Bianco, A.W. Castleman, J. Chem. Phys. **123**, 214308 (2005)
259. G. Grillon, P. Balcou, J.P. Chambaret, D. Hulin, J. Martino, S. Moustaizis, L. Notebaert, M. Pittman, T. Pussieux, A. Rousse, J.P. Rousseau, S. Sebban, O. Sublemontier, M. Schmidt, Phys. Rev. Lett. **89**, 065005 (2002)
260. J.W.G. Tisch, N. Hay, E. Springate, E.T. Gumbrell, M.H.R. Hutchinson, J.P. Marangos, Phys. Rev. A **60**, 3076 (1999)
261. M. Eloy, R. Azambuja, J.T. Mendonca, R. Bingham, Phys. Plasmas **8**, 1084 (2001)
262. E.S. Toma, H.G. Muller, Phys. Rev. A **66**, 013204 (2002)
263. Q. Zhong, A.W. Castleman, Chem. Rev. **100**, 4039 (2000)
264. V. Mijoule, L.J. Lewis, M. Meunier, Phys. Rev. A **73**, 033203 (2006)
265. C. Jungreuthmayer, M. Geissler, J. Zanghellini, T. Brabec, Phys. Rev. Lett. **92**, 133401 (2004)
266. S. Ter-Avetisyan, M. Schnürer, H. Stiel, U. Vogt, W. Radloff, W. Karpov, W. Sandner, P.V. Nickles, Phys. Rev. E **6403**, 036404 (2001)
267. P.V. Nickles, S. Ter-Avetsyan, H. Stiehl, W. Wandner, M. Schnürer, in *Superstrong fields in plasmas*, *AIP conference proceedings*, vol. 611, ed. by M. Lontano, G. Mourou, O. Svelto, T. Tajima (Am. Inst. Phys., 2002), p. 288
268. A. Youssef, R. Kodama, M. Tampo, Phys. Plasmas **13**, 030701 (2006)
269. R.A. Snavely, M.H. Key, S.P. Hatchett, T.E. Cowan, M. Roth, T.W. Phillips, M.A. Stoyer, E.A. Henry, T.C. Sangster, M.S. Singh, S.C. Wilks, A. MacKinnon, A. Offenberger, D.M. Pennington, K. Yasuike, A.B. Langdon, B.F. Lasinski, J. Johnson, M.D. Perry, E.M. Campbell, Phys. Rev. Lett. **85**, 2945 (2000)
270. U. Andiel, K. Eidmann, K. Witte, I. Uschmann, E. Förster, Appl. Phys. Lett. **80**, 198 (2002)
271. S. Augst, D. Strickland, D.D. Meyerhofer, S.L. Chin, J.H. Eberly, Phys. Rev. Lett. **63**, 2212 (1989)
272. G. Gibson, T.S. Luk, C.K. Rhodes, Phys. Rev. A **41**, 5049 (1990)
273. M. Dammasch, M. Dörr, U. Eichmann, E. Lenz, W. Sandner, Phys. Rev. A **64**, 061402 (2001)

274. A.H. Zewail, *Femtochemistry: Ultrafast dynamics of the chemical bond* (World Scientific, Singapore, 1994)
275. J. Manz, L. Wöste (eds.), *Femtosecond Chemistry* (VCH, Weinheim, 1995)
276. M. Chergui (ed.), *Femtochemistry: Ultrafast chemical and physical processes in molecular systems* (World Scientific, Singapore, 1996)
277. V. Sundström (ed.), *Femtochemistry and Femtobiology: Ultrafast reaction dynamics at atomic-scale resolution.* Nobel Symposium 101 (Imperial College Press, London, 1997)
278. A. Heidenreich, I. Last, J. Jortner, Eur. Phys. J. D **35**, 567 (2005)
279. A. Heidenreich, I. Last, J. Jortner, (to be published)
280. M. Lezius, S. Dobosz, D. Normand, M. Schmidt, Phys. Rev. Lett. **80**, 261 (1998)
281. Y. Fukuda, K. Yamakawa, Y. Akahane, M. Aoyama, N. Inoue, H. Ueda, Y. Kishimoto, Phys. Rev. A **67**, 061201(R) (2003)
282. R. Santra, C.H. Greene, Phys. Rev. Lett. **91**, 233401 (2003)
283. F. Megi, M. Belkacem, M.A. Bouchene, E. Suraud, G. Zwicknagel, J. Phys. B **36**, 273 (2003)
284. C. Achenbach, A. Müller, E. Salzborn, R. Becker, J. Phys. B **17**, 1405 (1984)
285. D.C. Griffin, C. Bottcher, M.S. Pindzola, S.M. Younger, D.C. Gregory, D.H. Crandall, Phys. Rev. A **29**, 1729 (1984)
286. D.C. Gregory, D.H. Crandall, Phys. Rev. A **27**, 2338 (1983)
287. M.E. Bannister, D.W. Mueller, L.J. Wang, M.S. Pindzola, D.C. Griffin, D.C. Gregory, Phys. Rev. A **38**, 38 (1988)
288. G. Hofmann, J. Neumann, U. Pracht, K. Tinschert, M. Stenke, R. Völpel, A. Müller, E. Salzborn, in *The physics of highly charged ions*, *AIP conference proceedings*, vol. 274, ed. by M. Stockli, P. Richard (AIP Press, New York, 1993), p. 485
289. W. Lotz, Z. Phys. **216**, 241 (1968)
290. K.J. Mendham, N. Hay, M.B. Mason, J.W.G. Tisch, J.P. Marangos, Phys. Rev. A **64**, 055201 (2001)
291. S. Chelkowski, P.B. Corkum, A.D. Bandrauk, Phys. Rev. Lett. **82**, 3416 (1999)
292. J.M. de Conto, J. Phys. IV **9**, 115 (1999)
293. D. Atwood, *Soft X-rays and extreme ultraviolet radiation: Principles and applications* (Cambridge University Press, Cambridge, 1999)
294. A. Heidenreich, I. Last, J. Jortner, Proc. Natl. Acad. Sci. USA **103**, 10589 (2006)
295. F. Paneth, Nature **119**, 706 (1927)
296. J.R. Huizenga, *Cold fusion: The scientific fiasco of the century* (Oxford University Press, Oxford, 1992)
297. J. Jortner, I. Last, ChemPhysChem **3**, 845 (2002)
298. B. Naranjo, J.K. Gimzewski, S. Putterman, Nature **434**, 1115 (2005)
299. I. Last, J. Jortner, Phys. Rev. Lett. (in press)
300. D.A. Ostlie, B.W. Carroll, *An introduction to modern stellar Astrophysics* (Addision-Wesley Publ. Comp. Inc., New York, 1996)
301. E.G. Adelberger, S.M. Austin, J.N. Bahcall, A.B. Balantekin, G. Bogaert, L.S. Brown, L. Buchmann, F.E. Cecil, A.E. Champagne, L. de Braeckeleer, C.A. Duba, S.R. Elliott, S.J. Freedman, M. Gai, G. Goldring, C.R. Gould, A. Gruzinov, W.C. Haxton, K.M. Heeger, E. Henley, C.W. Johnson, M. Kamionkowski, R.W. Kavanagh, S.E. Koonin, K. Kubodera, K. Langanke, T. Motobayashi,

V. Pandharipande, P. Parker, R.G.H. Robertson, C. Rolfs, R.F. Sawyer, N. Shaviv, T.D. Shoppa, K.A. Snover, E. Swanson, R.E. Tribble, S. Turck-Chieze, J.F. Wilkerson, Rev. Mod. Phys. **70**, 1265 (1998)